UiO : Department of Mathematics
University of Oslo

Simulating Cerebrospinal Fluid Flow and Spinal Cord Movement Associated with Syringomyelia

Fluid Structure Interaction in Idealized Geometries

Vegard Vinje

Master's Thesis, Spring 2016

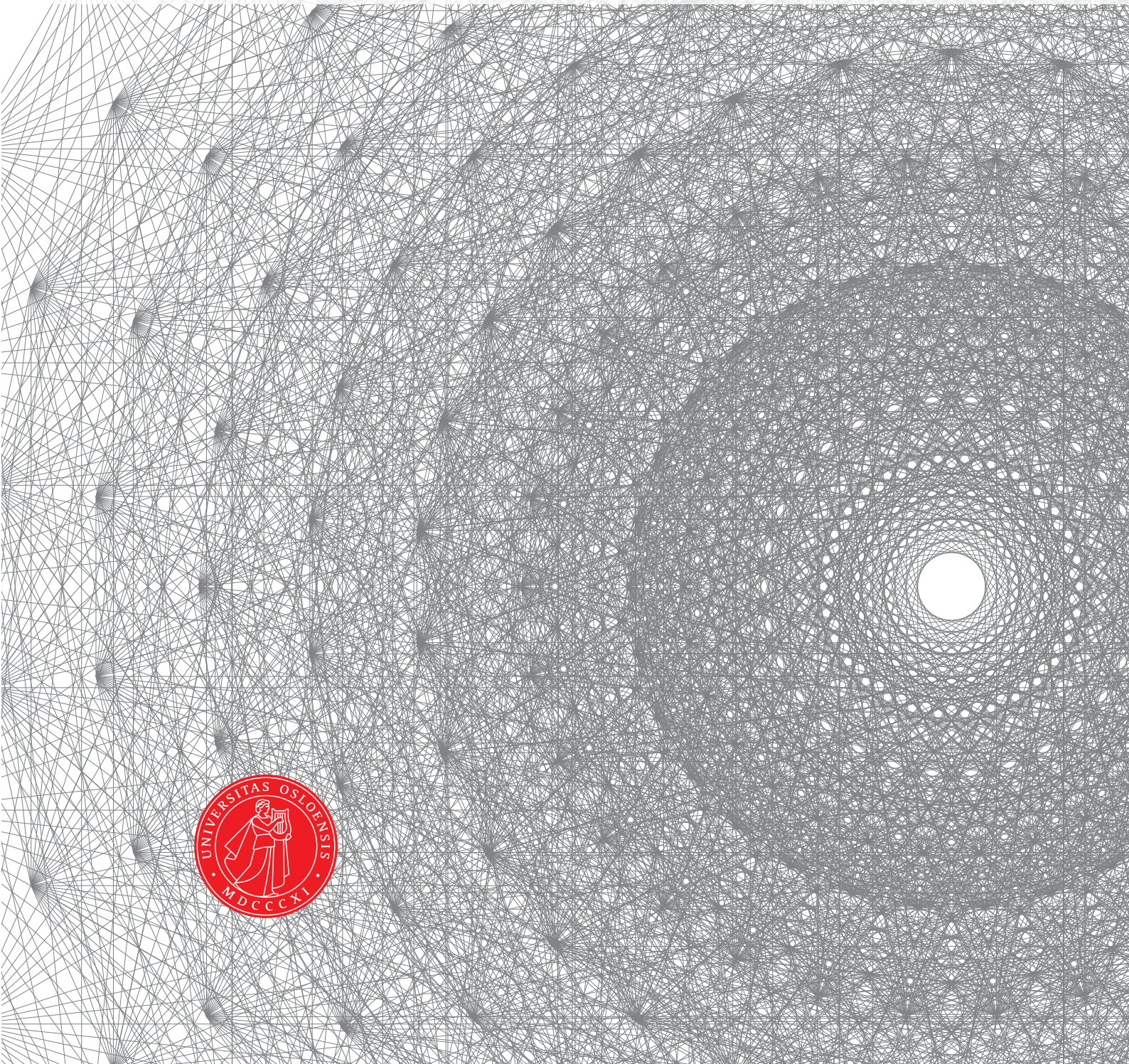

Cover design by Martin Helsø

The front page depicts a section of the root system of the exceptional Lie group E_8, projected into the plane. Lie groups were invented by the Norwegian mathematician Sophus Lie (1842–1899) to express symmetries in differential equations and today they play a central role in various parts of mathematics.

Acknowledgements

First of all, I want to thank my supervisors Kent-André Mardal, Marie Rognes and Victor Haughton. Kent, I appreciate our discussions about medical and numerical issues, in which I have learned a lot! Also, thank you for your guidance throughout the work of this thesis. Marie, thank you for taking time to discuss mathematical formulations of the medical problem, as well as encouraging me for further research of biomedical problems. Vic, you have given me more medical insight in relation to numerical modeling, and your interest for the underlying concepts within your expertise contributes by building bridges between the two fields of study.

I would also like to thank Eleonora Piersanti, Carlo Cisale and my father for constructive feedback on my thesis. Finally, I would like to thank all the great people contributing to the dynamic environments at Simula and at the Department of Mathematics at the University of Oslo. You have made most of the work writing this thesis enjoyable.

Part of this work was performed on the Abel Cluster, owned by the University of Oslo and the Norwegian metacenter for High Performance Computing (NOTUR), and operated by the Department for Research Computing at USIT, the University of Oslo IT-department.

http://www.hpc.uio.no/

This research is supported by the Research Council of Norway via NOTUR allocation NN9279K.

List of abbreviations

Medical

CSF ..... Cerebrospinal Fluid

SAS ..... Subarachnoid Space

CNS ..... Central Nervous System

MRI ..... Magnetic Resonance Imaging

PC-MRI ..... Phase Contrast Magnetic Resonance Imaging

MWA ..... Mean Wave Amplitude

ICP ..... Intracranial Pressure

LP ..... Lumbar Pressure

Mathematical/Numerical

CFD ..... Computational Fluid Dynamics

FSI ..... Fluid Structure Interaction

ALE ..... Arbitrary Lagrangian-Eulerian

BJS ..... Beavers-Joseph-Saffmann

CG ..... Continuous Galerkin

UFL ..... Unified Form Language

BB ..... Babuska-Brezzi

CSM ..... Computational Structural Mechanics

Contents

Chapter 1

Introduction

The Cerebrospinal Fluid (CSF) surrounds the brain and acts as a protection to the brain inside the skull. As a result of the cardiac cycle, the CSF will flow up and down the subarachnoid space (SAS) surrounding the spinal cord. The Chiari malformation is a downwards displacement of a part of the brain known as the cerebellar tonsils that partially block CSF flow entering and leaving the SAS. This malformation is associated with syringomyelia, which is the presence of a fluid filled cavity within the spinal cord tissue known as a syrinx. Treatment may include decompression surgery to remove parts of the bones of the skull to relieve pressure. Studies (e.g. Paul et al. (1983) [1], Lorenzo et al. (1995) [2], Guo et al. (2007)[3]) have shown that in many cases the syrinx gradually vanishes after surgery. The underlying mechanisms behind neither the formation nor the vanishing of the syrinx are yet fully understood.

In vivo measurements by Quigley et al. (2004) [4] and Haughton et al. (2003) [5] have shown that abnormal CSF flow is associated with the Chiari malformation. Many researchers have thus suggested computational fluid dynamics (CFD) as a tool to give useful insight, as experiments are very difficult and expensive. Idealized models have predicted abnormal CSF flow due to tonsillar herniation (Linge et al. (2011) [6]) as well as normalization of flow patterns by modeling cases of post-operative decompression surgery (Linge et al. (2014) [7]). CFD-studies in patient-specific models (Rutkowska et al (2012) [8], Clarke et al. (2013) [9]) have given further evidence that abnormal anatomy of the SAS contributes to abnormal pressure and flow patters. Cheng et al. (2014) [10] investigated effects of fluid structure interaction (FSI) on CSF pressure and velocities and concluded that cord motion was negligible.
On the other hand, *in vitro* FSI models by Martin and Loth (2009) [11] and Martin et al. (2010) [12] have suggested that the presence and location of a syrinx have a critical impact on the pressure environment in the SAS. Bertram et al. [13, 14, 15] have, in a series of *in silico* studies using FSI, investigated pressure waves traveling along the cord during a cough. Initially, it was believed that the so called "slosh" mechanism may not generate sufficient force to lengthen a syrinx. However, Bertram (2010) [16] has later discussed possible limitations of these studies and have suggested that the slosh effect could be of importance.

Kylstad (2014) [17] simulated the viscoelastic response of the spinal cord from applied pressure and compared displacement patterns between elastic and poroelastic models. Displacement patterns were shown to be similar but differ in magnitude depending on the material parameter setting. In the most extreme cases, displacement magnitudes were approximately 15 times larger for viscoelasticity, and a lag of 10 ms was observed compared to elastic models. These are both effects that can be triggered by altering parameters for the elastic spinal cord model. Støverud et al. (2015) [18] used poroelastic models to describe the spinal cord using in vivo pressure measurements as boundary conditions. To the authors knowledge poroelastic flow in the spinal cord has not yet been coupled to fluid flow in the SAS to investigate syringomyelia.

Therefore, the goal of this study is to model CSF flow around the cord and inside the syrinx by coupling computational models of viscous fluid flow in the SAS with elastic and, for the first time, poroelastic models for the spinal cord. In particular, changes in pressure and velocity distributions in the SAS as well as cord displacements due to the presence of a syrinx will be investigated. The governing equations are the Navier-Stokes equations in the SAS coupled to linear elasticity or Biot's (poroelastic) theory in cord tissue. The models will be implemented with the finite element method using FEniCS [19], a software package for automated scientific computing with main focus on partial differential equations. A mixed function space consisting of P2-P1-P1 (quadratic – linear – linear) elements are used in the elastic models and P2-P1-P2 elements are used in poroelastic models to represent velocities, pressure and displacements, respectively. Numerical solutions for the fluid domain are validated against exact solutions as well as benchmark simulations by Hron and Turek (2006) [20]. The same benchmark configuration is used to validate the elastic part as well as fluid-structure interaction simulations. Regarding model equations, extension to poroelasticity is not complicated, but a similar rigorous validation were not possible in this case due to the complexity of the problem as well as lack of comparative results.

Raw data from pressure measurements by Per Kristian Eide (Oslo University Hospital - Rikshospitalet) have also been taken into account and might add new insights in understanding flow patterns in the SAS or syrinx.

1.1 Outline

The field of biomechanics requires multidisciplinary knowledge within medicine, mathematics, mechanics and numerical modeling. The authors main field of study as well as the main focus in this thesis lie in the last three.
In chapter 2, necessary background information to understand the physical problem from the physiological point of view is presented.

The mathematical description of the physical problem based on laws of classical mechanics is given in chapter 3. The ALE-formulation, a necessary abstraction from the physical problem is also presented in this chapter.

Chapter 4 gives an introduction to the FEniCS software including a few examples validating the CFD-solver used in the thesis. Error estimates are also considered in this chapter.

In chapter 5, the implementation of a FSI model is described and validated by comparing results to a benchmark problem.

Implementation of the poroelastic model is given in chapter 6, and has been devoted a chapter itself due to differences in notation.

Chapter 7 gives a justification of the material parameters used in simulations of the SAS–spinal cord–syrinx system

Chapter 8 gives a short discussion of previous literature followed by main results from simulations of the medical problem.

In chapter 9, discussion, limitations, summary and possible future work is given.

Python code used in this thesis can be found at:

https://github.com/vegarvi/CSF_code

Chapter 2

Medical Background

In this chapter, a short description of the problem setting from a medical point of view is given. If not specified, the information given below is based on the textbook Human Anatomy and Physiology", by Van Wynsberghe, Noback, and Carola [21]

2.1 Anatomy of the central nervous system

The human nervous system consists of peripheral nervous system, and the central nervous system (CNS). The former consists of spinal and cranial nerves and sensory receptor organs while the latter consists of two parts: the brain and the spinal cord. The CNS receives and processes information from all parts of the body. Consequently, studies on the CNS are crucial for our understanding of human anatomy.

2.2 The Spinal Cord

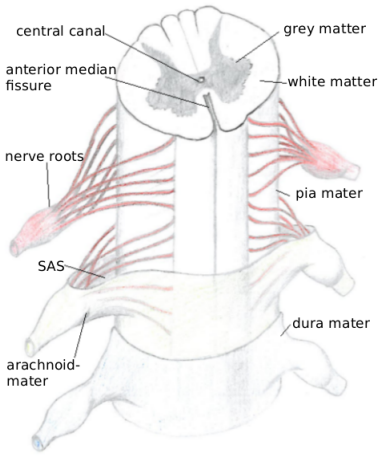

Figure 2.1: Schematic figure of the spinal cord. The pia mater surrounds the spinal cord, and between the pia mater and dura mater lies the subarachnoid space where CSF flows.

The spinal cord carries information between the body and the brain. It is divided into four or five regions from top to bottom: cervical (C), thoracic (T), lumbar (L) and sacral (S) in addition to the coccygeal part at the very bottom. The upper end of the spinal cord is continuous with the lowermost part of the brain, while the lower part tapers at the filum terminale, which attaches to the coccyx, known as the tailbone. Along the cord, there are 31 pairs of nerves exiting: 8 in the cervical region, 12 in the thoracic region, 5 in the lumbar region, 5 in the sacral region and one in the coccygeal region. The first four segments of the cord are usually referred as C1-C8, T1-T12, L1-L5, S1-S5. The tissue within the spinal cord consists of nervous tissue in form of white and grey matter which differs in both structure and function. In the center of the spinal cord, lies a tiny central spinal canal where CSF can flow. This channel closes off with age and should not be confused with the spinal canal which is sometimes used to denote the SAS. Surrounding the central canal lies the gray matter in an H-shape, similar to a butterfly. The rest consists of white matter, and the ratio between white and gray matter differs along the spinal cord.

There are three layers covering the brain and spinal cord known as meninges. The innermost layer surrounds the spinal cord and is known as the *pia mater*. The pia contains blood vessels that nourish the spinal cord. The middle layer, the *arachnoid* runs caudally extending almost all the way down the spinal cord. At the S2 vertebral level, the arachnoid joins the filum terminale. The outermost layer of the meninges protecting the spinal cord is known as the *dura mater* and is a though fibrous membrane.

2.3 The Chiari malformation

The Chiari malformation, also known as Arnold-Chiari Malformation, is a neurological condition where a displacement of a part of the brain, the cerebellum, or more presice the cerebellar tonsils, down through the foramen magnum occur. The condition is classified into four types, I-IV, where IV is the most severe. The main focus in this thesis is on type I. In a Chiari patient, the cerebellar tonsils obstructs the CSF flow (see figure 2.2) and even Chiari I patients have shown to have greater CSF velocities and a more complex flow pattern than healthy subjects [4]. These patients could also experience severe headaches, dizziness, tinnitus and muscle weakness. As the cerebellum is the part of the brain controlling balance, loss of coordination have also been reported.

2.3.1 Syringomyelia

In some cases, Chiari patients develop a fluid cavity, known as a syrinx within the spinal cord. Some of the symptoms are similar to the Chiari patients in general. These include muscle and back pain, weakness, numbness and inabilities to feel temperature changes. Many theories on the underlying mechanisms (pathogenesis) of syringomyelia have been proposed, though the details are not yet fully understood.

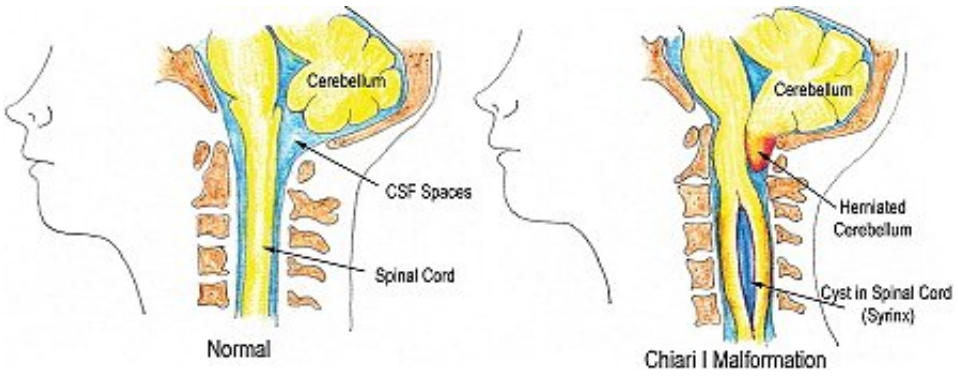

Figure 2.2: The Chiari malformation. Healthy subject to the left and a downward displacement into the CSF space known as the foramen magnum of the cerebellar tonsils on the right.

In patients diagnosed with Chiari I, about 2/3 develops syrinxes within the spinal cord tissue. It should be noted that not all Chiari patients have syringomyelia and in addition patients with syringomyeila does not necessary have the Chiari malformation.

Even though researchers do not seem to agree on the pathogenesis of syringomyelia, most seem to agree on the fact that altered CSF dynamics is associated with the formation of the syrinx. A few of these theories are given in the following section, literature review is given by Levine (2004) [22] or Elliott et al. (2013) [23]

2.3.2 Theories on the pathogenesis of syringomyelia

Williams (1980) [24] proposed that pressure waves traveling downwards in the SAS is transmitted to the cord and cause downwards acceleration of fluid inside the syrinx, possibly damaging spinal cord tissue. To explain upwards progression of syrinxes, Williams argued that coughing could play an important role. During a cough, the initial upwards motion is the sharpest and the upwards fluid rush is way more destructive than the downwards motion. Williams named his theory the slosh mechanism.

Greitz (2006) [25] proposed that obstruction in the SAS causes increased velocities and a pressure drop due to the Venturi effect. This causes the cord to expand radially leaving space for excess fluid within the cord. Radial expansion of the cord further increase velocities in narrowed regions of the SAS, causing an even greater Venturi effect.

Thompson et al. (2016) [26] have in a recent study suggested the anatomy of the cervical spinal canal plays a role in the formation of syrinxes. The study compared subjects with Chiari I with and without syringomyelia. The study showed that Chiari patients with syringomyelia had greater positive *C4-C7*-tapering (expanding caudally) of the cervical spinal canal, but no significant difference was found on *C1-C4*-tapering. Most notably, this shows that anatomy *below* the syrinx may also play an important role in the pathogenesis of syringomyelia.

Chapter 3

Mathematical background

The flow of CSF around the spinal cord requires equations for fluid flow to be coupled with equations for elasticity, or in the optimal case, poroelasticity. The underlying concepts of these kinds of problems were originally developed somewhat independently within petroleum engineering, geomechanics and hydrogeology. At first, the equations will be presented separately. Later in the chapter, coupling conditions will be discussed. Several quantities will be discussed, and as far as possible, we try to use a consistent notation for each quantity throughout the study.

This chapter aims to give a short description of the mathematical theory behind modeling CSF. The equations are first introduced by assuming a fixed set of coordinates. Later, the two fundamental descriptions of motion are discussed.

In providing the necessary mathematical background, it is convenient to give an overview of the notation used. If not specifically specified otherwise, we use:

$\mathbf{v}$ - Velocity of the material. In the fluid, $\mathbf{v}$ represents fluid velocity, while in the solid $\mathbf{v}$ denotes the velocity of the solid.

$\mathbf{U}$ - Total displacement of the solid. $\frac{\partial \mathbf{U}}{\partial t} = \mathbf{v}$ relates displacements and velocities in the solid whereas in the fluid, $\mathbf{U}$ represents the total mesh displacement.

p - Pressure in the fluid. In the case of elasticity, no pressure variable exist in the solid. In the case of poroelasticity, p represents the pore pressure inside the fluid/solid mixture.

$\mathbf{w}$ - Domain velocity (i.e, all material points within the domain moves with velocity $\mathbf{w}$). In the case of a pure elastic medium, the solid domain changes with the velocity of the solid, $\mathbf{v}$. Hence, in the solid we have $\mathbf{v} = \mathbf{w}$, which will not necessarily hold in the fluid.

Unit vectors in the Cartesian coordinate system are denoted $\mathbf{i} = (1, 0, 0), \mathbf{j} = (0, 1, 0)$ and $\mathbf{k} = (0, 0, 1)$. For summation convention, the common choice $\mathbf{i}_i, \mathbf{i}_j, \mathbf{i}_k$ are used respectively.

The index notation to denote components of vectors and tensors are used together with Einstein summation convention $\mathbf{v}_i\mathbf{i}_i = v_1\mathbf{i}_i + v_2\mathbf{i}_j + v_3\mathbf{i}_k$ for a vector $\mathbf{v} = (v_1, v_2, v_3)$ are used occasionally. A sum is taken over a repeated index.

It should be noted that the definition of ∇ differs in the literature. We define ∇ as a tensor, $\nabla = \mathbf{i}_i \frac{\partial}{\partial x_i}$, and thus $\nabla\mathbf{v} = \frac{\partial v_i}{\partial x_j}\mathbf{i}_j\mathbf{i}_i$

Subscripts f and s are used to denote fluid and solid quantities, respectively

3.1 Fluid flow

The most fundamental equations in fluid flow are the conservation laws. These equations are based on classical mechanics, and states conservation of mass, momentum and energy. In the literature, these are often referred to as balance equations.

3.1.1 The Divergence Theorem

The divergence theorem is result that relates the flow of a *vector field* through a closed surface to the divergence of the vector field inside the surface. The theorem is usually credited to Green or Gauss, but other mathematicians also contributed (see e.g. [27] for a brief history) . For a vector field $\mathbf{F}$ in a region V_0 bounded by a closed surface S_0, the divergence theorem states that

$$\int_{V_0} \nabla \cdot \mathbf{F} \mathrm{d}V = \int_{S_0} \mathbf{F} \cdot \mathbf{n} \mathrm{d}S, \tag{3.1}$$

where $\mathbf{n}$ is the outward unit normal on S_0. For a second rank *tensor* $\mathbf{T} = T_{ij}\mathbf{i}_i\mathbf{i}_j$ for $i, j = 1, 2, 3$, the divergence theorem becomes a vector equation, and will differ slightly with the tensor notation used in this thesis. We have

$$\nabla \cdot \mathbf{T} = \mathbf{i}_i \frac{\partial}{\partial x_i} \cdot T_{kj}\mathbf{i}_k\mathbf{i}_j = \frac{\partial T_{ij}}{\partial x_i}\mathbf{i}_j.$$

To ensure the divergence theorem to hold for each direction $\mathbf{i}_j$, the volume integral over this expression must equal the surface integral of

$$T_{ij}n_i\mathbf{i}_j = n_i\mathbf{i}_i \cdot T_{jk}\mathbf{i}_j\mathbf{i}_k = \mathbf{n} \cdot \mathbf{T}.$$

Therefore, the divergence theorem for a second-rank tensor becomes

$$\int_{V_0} \nabla \cdot \mathbf{T} \mathrm{d}V = \int_{S_0} \mathbf{n} \cdot \mathbf{T} \mathrm{d}S. \tag{3.2}$$

For a symmetric tensor, $\mathbf{n} \cdot \mathbf{T} = \mathbf{T} \cdot \mathbf{n}$ holds, hence equation is (3.1). On the other hand, when dealing with non-symmetric tensors the form (3.2) must be used.

3.1.2 Reynolds Transport Theorem

The famous engineer and scientist Osbourne Reynold stated the general conservation law the following way [28]:

Any change whatsoever in the quantity of any entity within a closed surface can only be effected in one or other of two distinct ways:

1. it may be effected by the production or destruction of the entity within the surface, or
2. by the passage of the entity across the surface.

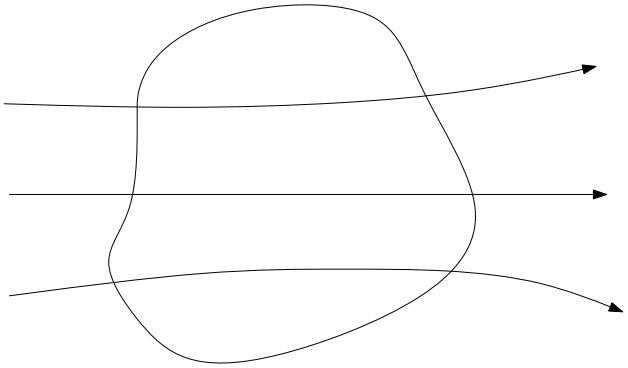

Figure 3.1: Fixed control volume with flow as indicated by streamlines

It should be noted that the transport theorem can be approached in two different ways. One for a fixed set of spatial coordinates, a fixed control volume, where fluid can enter and exit the boundaries of the defined body. The other approach has a control volume consisting of the same material particles at all times. Therefore the body has to follow the flow, and no fluid will cross the boundary. In this approach, one has to take into account the movement of the boundary of the body and the fact that the body can change it's volume. More on descriptions of motion is described in section 3.5

Now, consider a fixed control volume, V_0 and some fluid property $Q(\mathbf{x}, t)$. The rate of change of Q within the control volume can be written

$$\frac{\mathrm{d}}{\mathrm{d}t}\int_{V_0} Q(\mathbf{x}, t)\,\mathrm{d}V.$$

The net change of Q must be equal the rate of change in Q within the control volume plus the net rate of mass flow out of the volume. In other words:

$$\frac{\mathrm{d}}{\mathrm{d}t}\int_{V_0} Q(\mathbf{x}, t)\,\mathrm{d}V = \int_{V_0} \frac{\partial Q(\mathbf{x}, t)}{\partial t}\mathrm{d}V + \int_{S_0} Q(\mathbf{x}, t)\mathbf{v}\cdot\mathbf{n}\mathrm{d}S.$$

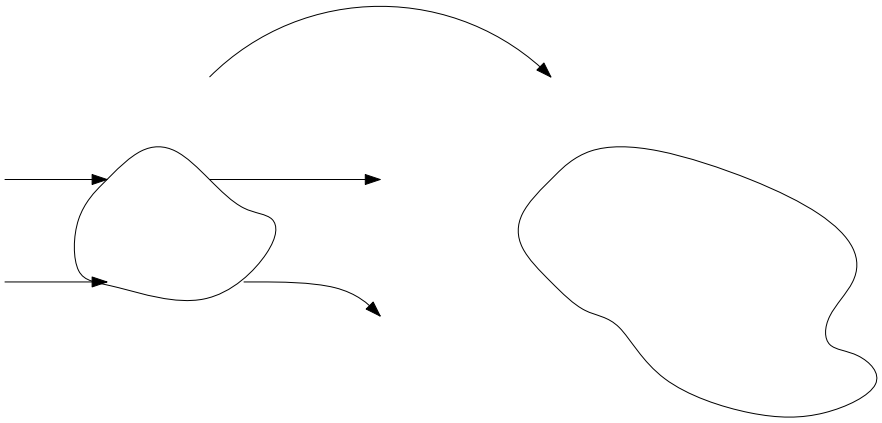

Figure 3.2: A moving control volume, consisting of the same fluid particles at time t (left) and time $t + \Delta t$ (right)

Here, $\mathbf{v}$ denotes fluid velocity, and $\mathbf{n}$ denotes the outward pointing unit-normal, i.e. $\mathbf{n}$ points *out* of the fluid. This equation is known as Reynold's transport theorem. The right hand side could be rewritten by using the divergence theorem on the last term.

$$\frac{\mathrm{d}}{\mathrm{d}t}\int_{V_0} Q(\mathbf{x},t)\,\mathrm{d}V = \int_{V_0}\big[\frac{\partial Q(\mathbf{x},t)}{\partial t} + \nabla\cdot(Q(\mathbf{x},t)\mathbf{v})\big]\mathrm{d}V. \tag{3.3}$$

3.1.3 Conservation of mass and momentum

Choose $Q(\mathbf{x},t) = \rho$, where ρ is fluid density. Conservation of mass means that

$$\frac{\mathrm{d}}{\mathrm{d}t}\int_{V_0} \rho\,\mathrm{d}V = 0,$$

which can be rewritten by using the transport theorem (3.3):

$$\int_{V_0}\big[\frac{\partial \rho}{\partial t} + \nabla\cdot(\rho\mathbf{v})\big]\mathrm{d}V = 0.$$

This should hold for any volume V_0, hence the integrand has to be zero. If there existed a point where the integrand were not zero, the control volume could be an arbitrary small enclosed sphere around this point, and the volume integral would not be zero. Therefore,

$$\frac{\partial \rho}{\partial t} + \nabla\cdot(\rho\mathbf{v}) = 0. \tag{3.4}$$

Equation (3.4) is known as the continuity equation and states conservation of mass.

To derive a similar property for momentum, Newton's second law of motion is used. The net change of momentum must be equal to the applied forces to the system. The forces can be divided into volume forces, acting on the entire control

volume, and forces acting only on the control surface. The forces acting on the surface can be written $\sigma_f \cdot \mathbf{n}$, where $\sigma_f = \sigma_f(\mathbf{v}, p)$ is the (symmetric) tensor denoting the total stress.

Thus, balance of momentum requires that

$$\frac{\mathrm{d}}{\mathrm{d}t}\int_{V_0} \rho\mathbf{v}(\mathbf{x},t)\mathrm{d}V = \int_{\partial V_0} \sigma_f \cdot \mathbf{n}\,\mathrm{d}S + \int_{V_0} \mathbf{F}_v \mathrm{d}V.$$

By using the transport theorem on the left hand side and the divergence theorem on the surface integral on the right hand side, we end up with

$$\int_{V_0} [\frac{\partial \rho\mathbf{v}}{\partial t} + \nabla\cdot(\rho\mathbf{v}\mathbf{v}) - \nabla\cdot\sigma_f - \mathbf{F}_v]\mathrm{d}V = 0.$$

With the same argument as before the integrand has to be zero, and with some rearrangement:

$$\frac{\partial \rho\mathbf{v}}{\partial t} + \nabla\cdot(\rho\mathbf{v}\mathbf{v}) = \nabla\cdot\sigma_f + \mathbf{F}_v. \tag{3.5}$$

The left hand side can be rewritten as

$$\rho\frac{\partial \mathbf{v}}{\partial t} + \mathbf{v}\frac{\partial \rho}{\partial t} + \mathbf{v}\mathbf{v}\cdot\nabla\rho + \rho\mathbf{v}\cdot\nabla\mathbf{v} + \mathbf{v}\rho\cdot\nabla\mathbf{v} = \rho\Big(\frac{\partial \mathbf{v}}{\partial t} + (\mathbf{v}\cdot\nabla)\mathbf{v}\Big) + \Big(\frac{\partial \rho}{\partial t} + \nabla\cdot(\mathbf{v}\rho)\Big),$$

where the last term is zero due to mass conservation. Equation (3.5) can then be written

$$\rho\Big(\frac{\partial \mathbf{v}}{\partial t} + (\mathbf{v}\cdot\nabla)\mathbf{v}\Big) = \nabla\cdot\sigma_f + \mathbf{F}_v. \tag{3.6}$$

The stress tensor, σ_f, depends on fluid properties and will be defined in the next subsection. Equation (3.6) is known as the momentum equation as it states conservation of momentum.

3.1.4 Incompressible Newtonian fluids

In this text we will only consider incompressible fluid flow for a Newtonian fluid. The information given below is based on explanations by White, [29, pp. 65-66] and Gjevik [30]

The assumption of a Newtonian fluid requires the viscous stresses to be linear functions of the components of the strain-rate tensor, denoted by ϵ. These assumptions were first made by Stokes in 1845. Stokes' assumptions have later proven to be quite accurate for all gases and most common fluids. Stokes' three postulates regarding the deformation laws are:

1. The fluid is continuous, and its stress tensor, $\sigma_{f_{ij}}$ is at most a linear function of the strain rates, ϵ_{ij}

2. The fluid is isotropic, i.e., its properties are independent of direction, and therefore the deformation law is independent of the coordinate axes in which it is expressed.

3. When the strain rates are zero, the deformation law must reduce to the hydrostatic pressure condition, $\sigma_{f_{ij}} = -p\delta_{ij}$, where δ_{ij} is the Kroenecker delta function.

From the first and third condition the following assumption can be made

$$\sigma_{f_{ij}} = -p\delta_{ij} + M_{ijkl}\epsilon_{kl} \tag{3.7}$$

As done by Gjevik, listing each component, it can be shown that symmetry of σ_f and ϵ also requires symmetry of M. This assumption reduces the number of coefficients in equation (3.7) from 36 to 21. If Stokes' second condition is also taken into account and the fluid properties are identical in each direction, the number of coefficients are further reduced to 2. These simplifications allow us to denote the stress tensor as

$$\sigma_{f_{ij}} = -p\delta_{ij} + 2\mu\epsilon_{ij} + \lambda\nabla\cdot\mathbf{v}\delta_{ij}, \tag{3.8}$$

where $\epsilon_{ij} = \frac{1}{2}(\frac{\partial v_i}{\partial x_j} + \frac{\partial v_j}{\partial x_i})$, p is the fluid pressure and μ and λ are known as Lame's constants. In the present study we only consider incompressible flow where ρ is constant. From the continuity equation (3.4), this implies $\nabla\cdot\mathbf{v} = 0$ and the last term in equation (3.8) vanishes. Furthermore,

$$\nabla\cdot 2\mu\epsilon = \mu\frac{\partial}{\partial x_j}(\frac{\partial v_j}{\partial x_i} + \frac{\partial v_i}{\partial x_j})\mathbf{i}_i = \mu(\frac{\partial}{\partial x_i}\frac{\partial v_j}{\partial x_j} + \frac{\partial v_i}{\partial x_j\partial x_j})\mathbf{i}_i = \mu\frac{\partial v_i}{\partial x_j\partial x_j}\mathbf{i}_i = \mu\nabla^2\mathbf{v}$$

Which simplifies the representation of $\nabla\cdot\sigma_f$ in (3.6) for an incompressible fluid

3.2 Navier-Stokes equations for incompressible flow

The system of equations (3.4),(3.6) are commonly referred to as the Navier-Stokes equations written in *divergence form*, where the Cauchy stress tensor, σ is explicitly included in the momentum equation and contributes to the momentum through its divergence. However, in the case of Newtonian incompressible fluids, the simplifications described in the previous section allows us to write the system of equations in *Laplace form*

$$\rho(\frac{\partial\mathbf{v}}{\partial t} + (\mathbf{v}\cdot\nabla)\mathbf{v}) = -\nabla p + \mu\nabla^2\mathbf{v} + \mathbf{F}_v$$

$$\nabla\cdot\mathbf{v} = 0.$$

The parameters ρ and μ describe fluid density and dynamic viscosity. Often, the momentum equation is written in terms of the kinematic viscosity $\nu = \frac{\mu}{\rho}$, by dividing the momentum equation with ρ.

It should be noted that the two formulations of the momentum equation are equivalent in their original form. In textbooks, see e.g. [29, 31, 32], the Laplace form is usually the form first presented as the Navier-Stokes equations probably because it is the simplest form explicitly including the two unknowns $\mathbf{v}$ and p.

Navier-Stokes equations are coupled and non-linear, and can generally not be solved analytically. However, numeruous analytical solutions have been carried out for different specific problems, and a good overview is given by White [29, pp. 97-164]. (Further references are also given in this textbook for the interested reader) These problems are often very simple and idealized. Hence, numerical solutions are a necessity to obtain useful solutions to real-life problems. Such methods will be discussed in chapters 4,5 and 6.

3.2.1 Boundary conditions

Before the equations can be solved, appropriate boundary conditions needs to be imposed on all boundaries of the domain. For a specific fluid occupying a domain, the treatment of boundary conditions is what distinguishes different flow patterns as the governing equations inside the domain stays exactly the same.
A fluid generally moves around between solid boundaries, $\partial\Omega_D$ and boundaries known as traction boundaries $\partial\Omega_N$.
On $\partial\Omega_D$ e.g. the interface between a fluid and a solid wall, the fluid velocity must equal the wall velocity in all directions, often known as the no-slip boundary condition. For instance at a rigid wall, the boundary condition will be $\mathbf{v} = 0$ on $\partial\Omega_D$, or in general

$$\mathbf{v} = \mathbf{v_0} \quad \text{on } \partial\Omega_D$$

On $\partial\Omega_N$ external forces on the system must be imposed. At surfaces where arbitrary forces $\mathbf{F}$ are acting, the fluid stress on the surface must equal these external forces. This can be written

$$\sigma \cdot \mathbf{n} = \mathbf{F} \quad \text{on } \partial\Omega_N$$

Where $\mathbf{n}$ is the outward normal unit vector.
This is also the case of a free surface, except the shear forces are negligible and that only external pressures are applied. This yields

$$\sigma \cdot \mathbf{n} = -p_0\mathbf{n} \quad \text{on } \partial\Omega_N$$

where p_0 is a known external pressure, for instance atmospheric pressure at the ocean surface.

A third option is the so called pseudo-traction boundary condition, where we set

$$\mu\frac{\partial \mathbf{v}}{\partial n} - p\mathbf{n} = -p_0\mathbf{n} \text{ on } \partial\Omega_N \tag{3.9}$$

where p_0 is some prescribed pressure. With the tensor notation of ∇, the normal derivative is defined as $\frac{\partial \mathbf{v}}{\partial n} = \mathbf{n} \cdot \nabla \mathbf{v}$. This boundary condition is often associated with the Laplace form of the Navier-Stokes equation as it is what naturally appears on the boundary when integrating the weak form of the Laplace term by parts.

It should also be noted that the physical implications between the pseudo-traction condition is different from the external force boundary condition $\sigma \cdot \mathbf{n} = \mathbf{F}$. Assume we have two-dimensional horizontal channel, and take a moment to examine the interpretation, or physical implications, of the pseudo-traction condition (3.9) on the outlet ($\mathbf{n} = (1, 0)$)

$$\mu \frac{\partial \mathbf{v}}{\partial n} - p\mathbf{n} = -p_0 \mathbf{n}.$$

With unit-vectors $\mathbf{i}$ and $\mathbf{j}$ in the x- and y-direction and the velocity vector $\mathbf{v} = (v_1, v_2)$, the two components can be written

$$\mu \frac{\partial v_1}{\partial x} - p = -p_0,$$
$$\mu \frac{\partial v_2}{\partial x} = 0.$$

The second condition can be interpreted as having the vertical component, v_2 equal just outside and just inside the domain. This should mimic a continuation of the channel under the assumption that $v_2 = 0$ inside the channel which is valid due to mass conservation.

A condition on $\sigma \cdot \mathbf{n}$ on the boundary is a more general approach for setting external forces on the boundary. The physical implications of no external forces on the outlet in the previous example could be compared to a garden hose, where water can exit in all directions and creep around the corners of the outlet.

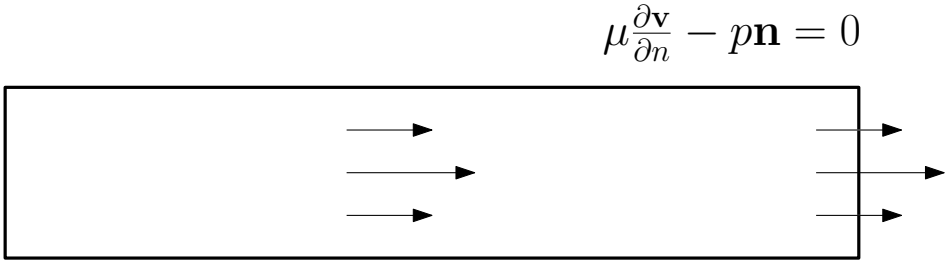

Figure 3.3: The pseudo traction boundary condition implies a continuation of the channel

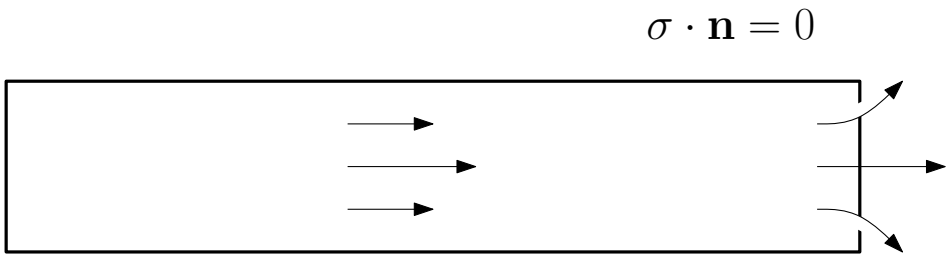

Figure 3.4: No external forces implies an open end of the channel, and fluid can escape in all directions

3.3 Linear Elasticity

The equation describing elasticity is derived by using Reynolds Transport theorem on a moving domain, Ω^t, consisting of the same particles at all times. For conservation of momentum, the change in momentum must equal the applied forces to the system as well as body forces:

$$\frac{\mathrm{d}}{\mathrm{d}t}\int_{\Omega^t}\rho\mathbf{v}\mathrm{d}V = \int_{\Omega^t}\rho\frac{\partial\mathbf{v}}{\partial t}\mathrm{d}V + \int_{\partial\Omega^t}\rho\mathbf{v}\mathbf{v}\cdot\mathbf{n}\mathrm{d}S = \int_{\partial\Omega^t}\sigma_s\cdot\mathbf{n}\mathrm{d}S + \int_{\Omega^t}\mathbf{F}_v\mathrm{d}V,$$

where σ_s is the stress tensor describing the elastic material. By applying the divergence theorem again, we end up with the general elasticity equation in a moving domain:

$$\rho\frac{\partial\mathbf{v}}{\partial t} + \rho(\mathbf{v}\cdot\nabla)\mathbf{v} = \nabla\cdot\sigma_s + \mathbf{F}_v. \tag{3.10}$$

Linear elasticity is an approximation used for small deformations for elastic solids. As a rule of thumb, the approximation of linear elasticity is usually valid for deformations up to 10% relative to the solid. The stress tensor for a linear elastic medium is very similar to (3.8) describing an incompressible Newtonian fluid, except there is no fluid pressure, and the stress is related to the total displacement $\mathbf{U}$ rather than the velocity $\mathbf{v}$. Assuming a linear relation between stress and strain, the stress tensor for such a material reads $\sigma_s = 2\mu\epsilon(\mathbf{U}) + \lambda\mathrm{tr}(\epsilon(\mathbf{U}))\delta$, where ϵ is defined exactly as the strain rate tensor for a Newtonian fluid. Within the framework of linear elasticity, the convective term is regarded as small and thus neglected. It is then common to write the equation only involving one unknown, $\mathbf{U}$ by substituting $\frac{\partial\mathbf{U}}{\partial t} = \mathbf{v}$.

We choose to keep the equation (3.10) for simulations in this thesis. The reason for choosing the solid velocity $\mathbf{v}$ as the unknown will be discussed in chapter 5. Also, by using this form, the nonlinear term add no complexity to the coupled system we want to solve later, as the momentum equation in the fluid will have a similar term. Thus, our linear elasticity approximation lies in the inexact description of σ_s, which in general will consist of nonlinear terms depending on the elasticity model.

3.4 Linear Poroelasticity

In this section, the equations describing fluid flowing through an elastic, porous medium is presented. For a more detailed discussion, derivation and history within the field we refer to Wang [33] on Linear Poroelasticity. The equations describing linear poroelasticity are often referred to as Biot's equations.

3.4.1 Fluid flow through a porous medium

A porous medium is a solid structure with pores in which fluid can flow. The principles of modeling porous flow consist of macroscopic averaging over the pores. The structural part is often denoted skeleton, matrix or frame, and in general all the pores will have different size and shape. In this subsection the skeleton is assumed rigid. The nature of the material defines whether we will be able to fully solve the problem with no-slip conditions on all skeleton parts, or if some kind of volumetric averaging can be done. If the observer is interested in velocity variations on the scales of the pores, conventional fluid dynamics must be used. When there are many pores and channels, the complexity of the problem makes the full Navier-Stokes system difficult to solve. In these cases, macroscopic volume averaging is usually done, where the effects of the skeleton is modeled by introducing parameters constant over the material considered, such as permeability and conductivity.
These kinds of simplifications results in the famous Darcy's law (see e.g. Nield and Bejan (2013)[34]) generalized in three dimensions:

$$\mathbf{q} = -\frac{1}{\mu}\mathbf{K} \cdot \nabla p. \tag{3.11}$$

Here $\mathbf{K}$ is the *permeability* tensor, and μ is the dynamic viscosity of the fluid. If the medium considered is isotropic, the permeability is a scalar value and equation (3.11) can be expressed as

$$\mathbf{q} = -\frac{K}{\mu}\nabla p.$$

Sometimes the permeability is given through the *hydraulic conductivity*, κ, where $\kappa = \frac{K}{\mu_f}$ relates the two parameters for a fully saturated porous medium. It should be noted that the velocity $\mathbf{q}$, known as the Darcy velocity (or Darcy flux), represents the average flux over a representative elementary volume, and thus the average fluid velocity experienced by a particle in the pores will be $\mathbf{v}_p = \frac{\mathbf{q}}{\phi}$ where ϕ is the *porosity* and describes the ratio of the pore volume versus the total volume. A high porosity indicates a large volume of pores compared to the skeleton and in general less obstruction of fluid.

3.4.2 Biot's equations

As in the previous section, we let the domain consist of a skeleton with fluid filled pores. The extension for the Biot problem is that the skeleton is now free to move as an elastic material. Incompressibility for the fluid and solid is assumed. We define the filtration velocity $\mathbf{q} = \phi(\mathbf{v}_p - \mathbf{v}_s)$ where $\mathbf{v}_p$ is the fluid velocity in the pores and $\mathbf{v}_s$ is the structural velocity. $\mathbf{q}$ is thus regarded as the relative velocity of the fluid compared to the solid. The velocity of the skeleton $\mathbf{v}$, the filtration velocity $\mathbf{q}$, and the pore pressure p, can now be related by the following set of equations[35],[36],[37]

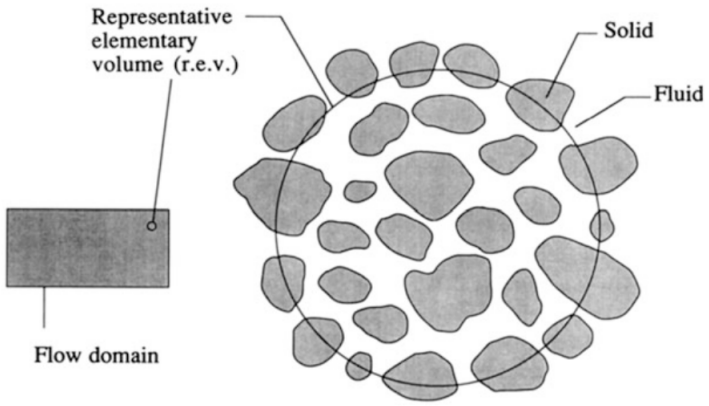

Figure 3.5: Representation of porous media where the averaging approach is used. From Nield and Bejan (2013)

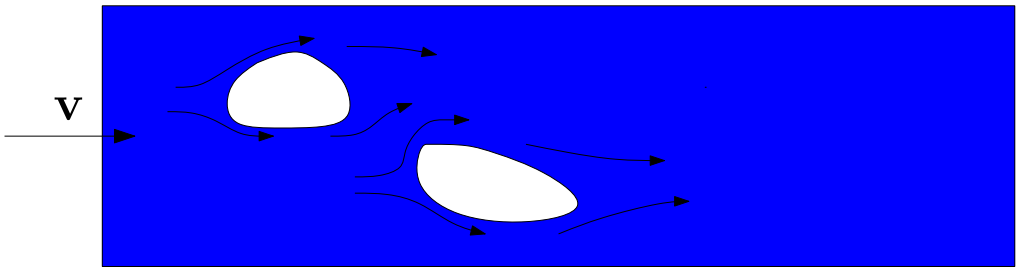

Figure 3.6: River flow around two islands representing the pores. The full Navier-Stokes system should be solved for this problem

$$\rho_p \frac{\mathrm{d}\mathbf{v}_s}{\mathrm{d}t} + \rho_f \frac{\mathrm{d}\mathbf{q}}{\mathrm{d}t} + \nabla p - \nabla \cdot \sigma_s(\mathbf{U}) = \mathbf{f}_s \tag{3.12}$$

$$\rho_f \frac{\mathrm{d}\mathbf{v}_s}{\mathrm{d}t} + \rho_f \frac{\mathrm{d}\mathbf{q}}{\mathrm{d}t}\frac{1}{\phi} + K^{-1}\mathbf{q} + \nabla p = \mathbf{f}_d \tag{3.13}$$

$$\nabla \cdot (\mathbf{v}_s + \mathbf{q}) = 0. \tag{3.14}$$

These equations state conservation of momentum equation for the total force balance (3.12), conservation of momentum for the fluid phase only, (3.13) and the constraint of incompressibility (3.14). ρ_f is the density of the fluid in the pores, and $\rho_p = \rho_s(1-\phi) + \rho_f\phi$ where ρ_s is the density of the skeleton.

In relation to Darcy's law without external forces, equation (3.13) describes an extension both in terms of the material derivative of $\mathbf{q}$, as well as extension into the poroelastic regime. The former is an extension to Darcy's law as proposed by Nield and Bejan (2013), where originally we have used $\frac{1}{\phi}$ as the acceleration coefficient tensor. Biot's equations have been much used in applied geoscience and hydrogeology, where the time derivative $\frac{\mathrm{d}\mathbf{q}}{\mathrm{d}t}$ is small. This assumption is probably less valid for some applications within biomedical computing, however as the spinal

cord has previously believed to be impermeable, and also according to previous results by Drøsdal [38], we expect $\mathbf{q}$ to be small and that the material derivative can be dropped. The term $K^{-1}\mathbf{q}$ should be kept, as K is assumed to be comparable to $\mathbf{q}$ in orders of magnitude.

3.5 Descriptions of Motion

The conservation equations for Newtonian fluids were derived from Reynolds' transport theorem by using a control volume fixed in space, while for elastic materials a moving control volume was used. In addition, we saw for instance that the stress tensor for elastic solids were linked to the total displacement, or deviation from the stress-free configuration, in the material. The stresses and velocity in the material will depend on the current deformation of the material with respect to the stress-free configuration.
To this end, it will be convenient to provide the reader with two classical descriptions of a continuum in motion.

3.5.1 Lagrangian and Eulerian descriptions of motion

We consider a domain $\Omega_{\mathbf{X}} \in \mathbb{R}^3$ consisting of material particles $\mathbf{X}$. The domain can undergo deformations, and the deformed domain, $\Omega_{\boldsymbol{x}}$, is the current configuration at time t.

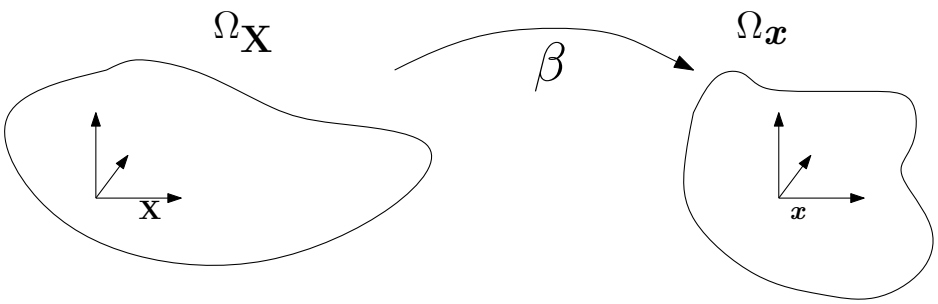

Figure 3.7: Lagrangian description of motion. The mapping β maps the reference coordinates to the spatial ones

We define the one-to-one mapping:

$$\begin{aligned} \beta \ : \ & \Omega_{\mathbf{X}} \times [0,T] \to \Omega_{\mathbf{x}} \times [0,T] \\ & (\mathbf{X},t) \to \beta(\mathbf{X},t) = (\mathbf{x},t), \end{aligned}$$

which takes any point $\mathbf{X}$ in the reference configuration to a new position $\mathbf{x} = \beta(\mathbf{X},t)$ at time t. As the mapping is one-to-one, it is also possible to keep track of the history of the motion by the inverse, β^{-1}. Time is measured with the same variable, t, in

both domains. The gradient of β with respect to $(\mathbf{X}, t)$ can be written in matrix form as:

$$\frac{\partial \beta}{\partial(\mathbf{X}, t)} = \begin{pmatrix} \frac{\partial \mathbf{x}}{\partial \mathbf{X}} & \mathbf{v} \\ 0^T & 1 \end{pmatrix},$$

where the material velocity

$$\mathbf{v}(\mathbf{X}, t) = \frac{\partial \mathbf{x}}{\partial t}\Big|_{\mathbf{X}}, \tag{3.15}$$

is the temporal change in the spatial variable $\mathbf{x}$ while holding $\mathbf{X}$ fixed. 0^T denotes a null vector.
The *Lagrangian* description, where we follow a fixed set of material particles as suggested by the mapping β, is often used. In the Lagrangian description all quantities are expressed in terms of the reference configuration $\Omega_{\mathbf{X}}$ and time. In other words, even though the material is deformed, we can still compute displacements and particle velocities using the material coordinates $\mathbf{X}$. For instance, the displacement from the starting material configuration will be given as $\beta(\mathbf{X}, t) - \mathbf{X}$ and the velocity as given in equation (3.15).
Because the grid coincides with the material coordinates, there are no convective terms in the Lagrangian description. In the context of Reynold's Transport theorem, the Lagrangian approach coincides with a moving control volume consisting of the same material points at all time. When a material undergoes large deformations, or for instance vortices or turbulence occur, the material velocity from the Lagrangian point of view becomes difficult to handle.

In fluid mechanics the *Eulerian* description is the most used, which means that fluid flows through a fixed region in space and in each point we can measure various properties or quantities such as velocity, pressure and temperature. The conservation equations in the Eulerian description are expressed in terms of the spatial coordinates $\mathbf{x}$ and time, and are neither connected to a reference configuration nor the material coordinates. Compared to the Lagrangian approach, large material deformations is not a problem, as material can enter and leave the fixed domain. This movement of a material through a fixed region results in convective effects, and convection operators can often be problematic in computational fluid dynamics due to their non-symmetric nature.

3.5.2 The Arbitrary Eulerian Lagrangian description

In order to couple the Lagrangian approach for the solid with the Eulerian approach for the fluid, we need some referential system, not attached to the material points neither totally fixed in space. This type of description is common in FSI analysis and is known as the *arbitrary Lagrangian-Eulerian* (ALE) description.

The following derivation is inspired by the work on Arbitrary Lagrangian-Eulerian

methods by Donea et al. (2004) [39].

In need of an additional set of coordinates, an independent referential system with reference coordinates χ is introduced. This introduces two new mappings to relate all the different configurations as shown in figure 3.8

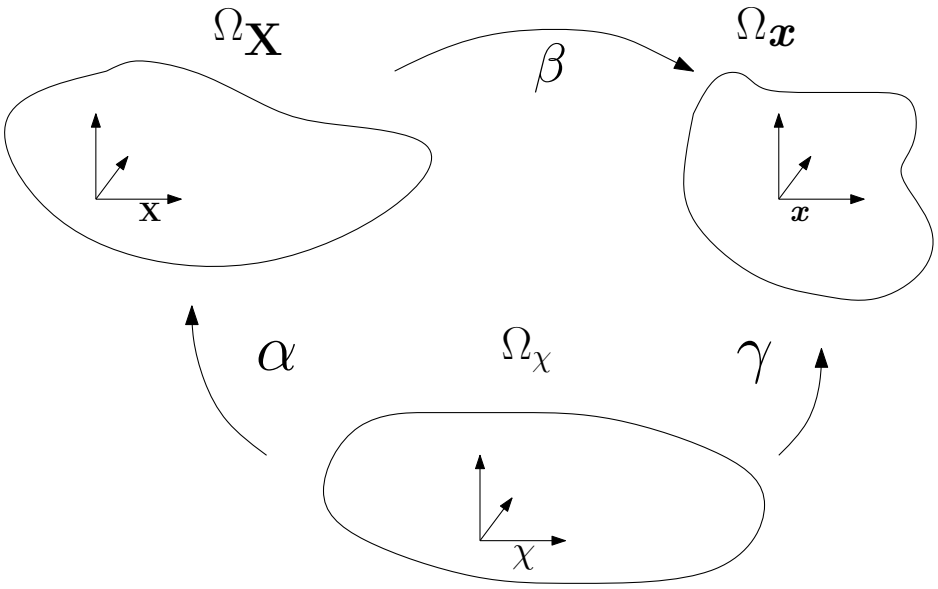

Figure 3.8: The three domains needed in the ALE formulation

The mappings are defined similarly to β:

$$\begin{aligned} \gamma \ : \ \Omega_\chi \times [0,T] &\to \Omega_{\mathbf{x}} \times [0,T] \\ (\chi, t) &\to \gamma(\chi, t) = (\mathbf{x}, t), \end{aligned}$$

and the gradient of γ is

$$\frac{\partial \gamma}{\partial(\chi, t)} = \begin{pmatrix} \frac{\partial \mathbf{x}}{\partial \chi} & \mathbf{w} \\ 0^T & 1 \end{pmatrix}.$$

In addition

$$\mathbf{w}(\chi, t) = \left.\frac{\partial \mathbf{X}}{\partial t}\right|_\chi$$

denotes mesh velocity. Both the mesh and the material can move independently of the fixed set of laboratory coordinates. More precise, relative to some referential point in space, the fluid moves with velocity $\mathbf{v}$ and the domain moves with velocity $\mathbf{w}$.

To complete the relation between the different velocities, we define the inverse of α directly:

$$\begin{aligned} \alpha^{-1} \ : \ \Omega_{\mathbf{X}} \times [0,T] &\to \Omega_\chi \times [0,T] \\ (\mathbf{X}, t) &\to \alpha^{-1}(\mathbf{X}, t) = (\chi, t). \end{aligned}$$

The gradient is given as

$$\frac{\partial \alpha^{-1}}{\partial(\mathbf{X},t)} = \begin{pmatrix} \frac{\partial \chi}{\partial \mathbf{X}} & \hat{\mathbf{v}} \\ 0^T & 1 \end{pmatrix},$$

where the velocity

$$\hat{\mathbf{v}}(\mathbf{X},t) = \frac{\partial \chi}{\partial t}\Big|_{\mathbf{X}}, \tag{3.16}$$

denotes the temporal change in the referential system while holding the material particle $\mathbf{X}$ fixed. Therefore the velocity $\hat{\mathbf{v}}$ can be interpreted as the particle velocity in the referential domain.

We use that $\beta = \gamma \circ \alpha^{-1} = \gamma(\alpha^{-1}(\mathbf{X},t))$ and obtain a relation between the different velocities by differentiating β:

$$\begin{aligned} \frac{\partial \beta}{\partial(X,t)}(\mathbf{X},t) &= \frac{\partial \gamma}{\partial(\chi,t)}(\alpha^{-1}(\mathbf{X},\mathbf{t}))\,\frac{\partial \alpha^{-1}}{\partial(\mathbf{X},t)}(\mathbf{X},t) \\ &= \frac{\partial \gamma}{\partial(\chi,t)}(\chi,t)\,\frac{\partial \alpha^{-1}}{\partial(\mathbf{X},t)}(\mathbf{X},t). \end{aligned}$$

In matrix form this equation is written

$$\begin{pmatrix} \frac{\partial \mathbf{x}}{\partial \mathbf{X}} & \mathbf{v} \\ 0^T & 1 \end{pmatrix} = \begin{pmatrix} \frac{\partial \mathbf{x}}{\partial \chi} & \mathbf{w} \\ 0^T & 1 \end{pmatrix} \begin{pmatrix} \frac{\partial \chi}{\partial \mathbf{X}} & \hat{\mathbf{v}} \\ 0^T & 1 \end{pmatrix}.$$

After block-multiplication of the right hand side, we end up with an equation relating the different velocities:

$$\mathbf{v} = \frac{\partial \mathbf{x}}{\partial \chi} \cdot \hat{\mathbf{v}} + \mathbf{w}.$$

To this end, it is convenient to define the convective velocity

$$\mathbf{c} := \mathbf{v} - \mathbf{w} = \frac{\partial \mathbf{x}}{\partial \chi} \cdot \hat{\mathbf{v}},$$

which is the relative velocity between the material and the mesh.

To obtain relation between quantities to formulate the balance equations, we let a scalar quantity, Q be defined as $Q(\mathbf{x},t), Q^*(\chi,t)$ and $Q^{**}(\mathbf{X},t)$ in the spatial, referential and material domains respectively.

To obtain a relation between the spatial description, Q, and material description Q^{**} we use the previously described mapping β:

$$Q^{**}(\mathbf{X},t) = Q(\beta(\mathbf{X},t),t) = Q \circ \beta.$$

The gradient of Q^{**} can then be computed as

$$\frac{\partial Q^{**}}{\partial(\mathbf{X},t)}(\mathbf{X},t) = \frac{\partial Q}{\partial(\mathbf{x},t)}(\mathbf{x},t)\,\frac{\partial \beta}{\partial(\mathbf{X},t)}(\mathbf{X},t), \tag{3.17}$$

or in matrix form:

$$\begin{pmatrix} \frac{\partial Q^{**}}{\partial \mathbf{X}} & \frac{\partial Q^{**}}{\partial t} \end{pmatrix} = \begin{pmatrix} \frac{\partial Q}{\partial \mathbf{x}} & \frac{\partial Q}{\partial t} \end{pmatrix} \begin{pmatrix} \frac{\partial \mathbf{x}}{\partial \mathbf{X}} & \mathbf{v} \\ 0^T & 1 \end{pmatrix}. \tag{3.18}$$

After matrix multiplication, one can obtain the well known equation between material and spatial time derivatives:

$$\frac{\partial Q^{**}}{\partial t} = \frac{\partial Q}{\partial t} + \frac{\partial Q}{\partial \mathbf{x}} \cdot \mathbf{v} \tag{3.19}$$

To ease notation we now recognize the material and spatial time derivatives $\frac{\partial Q^{**}}{\partial t} = \frac{\partial Q}{\partial t}\Big|_{\mathbf{X}}$, $\frac{\partial Q}{\partial t} = \frac{\partial Q}{\partial t}\Big|_{\mathbf{x}}$, and define the material and spatial derivatives the following way

$$\frac{\mathrm{d}}{\mathrm{dt}} := \frac{\partial}{\partial t}\Big|_{\mathbf{X}} \qquad\qquad \frac{\partial}{\partial t} := \frac{\partial}{\partial t}\Big|_{\mathbf{x}}$$

The relation (3.19) can now be written in a form probably already known to the reader:

$$\frac{\mathrm{d}Q}{\mathrm{dt}} = \frac{\partial Q}{\partial t} + (\mathbf{v} \cdot \nabla)Q. \tag{3.20}$$

The next step is to relate the material and the referential description of the quantity, Q^{**} and Q^{*} respectively, by the mapping α. This relation is written as

$$Q^{**} = Q^{*} \circ \alpha^{-1}.$$

By proceeding the exact same way as way as in (3.17) and (3.18), the relation between material and referential time derivatives is written

$$\frac{\partial Q^{**}}{\partial t} = \frac{\partial Q^{*}}{\partial t} + \frac{\partial Q^{*}}{\partial \chi} \cdot \hat{\mathbf{v}}.$$

If we rather want to express the spatial derivative of Q^{*} in the spatial domain, we can use the definition of $\hat{\mathbf{v}}$ from equation (3.16) to end up with

$$\frac{\partial Q^{**}}{\partial t} = \frac{\partial Q^{*}}{\partial t} + \frac{\partial Q}{\partial \mathbf{x}} \cdot \mathbf{c}.$$

This equation can be written in more common notation, and the following is known as *The fundamental ALE equation*

$$\frac{\mathrm{d}Q}{\mathrm{dt}} = \frac{\partial Q}{\partial t}\Big|_{\chi} + (\mathbf{c} \cdot \nabla)Q \tag{3.21}$$

and states that the time derivative in the material configuration equals its local (referential) derivative plus a convective term taking into account the relative difference in velocity between the two systems. It should be noted that the relations presented also holds for vector quantities.

Also, by combining equations (3.20) and (3.21), we can relate the spatial time derivative with the referential time derivative as

$$\frac{\partial Q}{\partial t} = \frac{\partial Q}{\partial t}\Big|_{\chi} - (\mathbf{w} \cdot \nabla)Q \tag{3.22}$$

3.6 Balance equations in the ALE framework

To obtain appropriate balance equations in the ALE framework we start by noting that the balance equations can be written in terms of the material derivatives as

$$\frac{\mathrm{d}\rho}{\mathrm{dt}} = \frac{\partial \rho}{\partial t} + \mathbf{v} \cdot \nabla \rho = -\rho \cdot \nabla \mathbf{v}$$

$$\rho \frac{\mathrm{d}\mathbf{v}}{\mathrm{dt}} = \rho \Big(\frac{\partial \mathbf{v}}{\partial t} + (\mathbf{v} \cdot \nabla)\mathbf{v} \Big) = \nabla \cdot \sigma.$$

By using equation (3.22), the spatial time derivatives can be replaced to obtain equations ine the ALE framework. The following equations should hold in *any* time-dependent domain which does not necessarily need to coincide with the movement of material particles.

$$\begin{aligned} \frac{\partial \rho}{\partial t}\Big|_{\chi} + \mathbf{c} \cdot \nabla \rho &= -\rho \nabla \cdot \mathbf{v} \quad \text{in } \Omega^t \\ \rho \Big(\frac{\partial \mathbf{v}}{\partial t}\Big|_{\chi} + (\mathbf{c} \cdot \nabla)\mathbf{v} \Big) &= \nabla \cdot \sigma \quad \text{in } \Omega^t \end{aligned}$$

These equations show that all one have to do in order to transform the Eulerian form of the balance equations into the ALE formulation is to replace the convective velocity with the relative velocity between the material and the mesh. In our simulations the solid domain and interface physically moves, and the fluid domain adjusts thereafter. It could be argued that mesh update is not necessary in combination with linear elasticity, and for the solid domain, this might be the case. The benefit of such a description is reflected in solid-to-fluid coupling by geometry change. For instance, if the fluid region is computed to be narrowed, fluid will flow faster through these areas with our description. This would not be the case when solving fluid equations in the rigid domain. The close relation to the Eulerian method has induced some authors to denote this approach the *quasi-Eulerian* description. (See e.g. [40]

3.6.1 Mesh updating

The velocity $\mathbf{w}$ can be seen as the mesh velocity when a computational mesh is used. In FSI, the ALE framework provides flexibility to combine the Lagrangian and Eulerian descriptions of motion. On the structural part, as well as on the fluid-structure interface, the domain Ω_s consists of the same material particles at all times and moves exactly with the material points within the structure. That is, $\mathbf{v}_s = \mathbf{w}_s$. The fluid domain has to follow the changes on the fluid-structure interface. Other than that the mesh velocity in the fluid domain is arbitrary in principle, but the choice of mesh velocity in the fluid domain is important for the accuracy of the solver. In general, important aspects to consider is distortion and squeeze of each element in the fluid domain.

A Laplacian smoothing algorithm is used to update the mesh, consisting of solving

a Laplace (or Poisson) equation for the mesh displacement in the fluid. The method is a mesh regularization method where the lines in the mesh have equal potential. This method was first introduced by Winslow in 1963 [41].

3.7 Fluid Structure Interaction

By establishing the flexibility of the ALE formulation together with an equation for a moving domain we can now state the governing equations for the Fluid-Structure interaction problem. In the case of an Newtonian incompressible fluid together with a linear elastic material in the absence of body forces, the mathematical problem consists of solving the following set of equations:

$$\begin{aligned} \rho_f\Big(\frac{\partial \mathbf{v}}{\partial t} + ((\mathbf{v}-\mathbf{w})\cdot\nabla)\mathbf{v}\Big) - \nabla\cdot\sigma_f(\mathbf{v},p) = 0 \quad & \text{in } \Omega_f^t \\ \nabla\cdot\mathbf{v} = 0 \quad & \text{in } \Omega_f^t \\ \nabla^2\mathbf{U} = 0 \quad & \text{in } \Omega_f^t \end{aligned}$$

$$\begin{aligned} \rho_s\frac{\partial \mathbf{v}}{\partial t} + \rho_s(\mathbf{v}\cdot\nabla)\mathbf{v} - \nabla\cdot\sigma_s(\mathbf{U}) = 0 \quad & \text{in } \Omega_s^t \\ \mathbf{w} = \mathbf{v} \quad & \text{in } \Omega_s^t \end{aligned}$$

In the case of fluid interacting with a solid structure, no material can cross the moving boundary Γ^t, and thus the fluid and solid velocity must be equal on the interface between the fluid and the solid. In general, mass conservation on the boundary must be ensured. In addition, the forces acting on each side of the surface must be equal. A difference in forces from each material on the interface would result in infinite acceleration on the infinitely thin surface. Mathematically, these two conditions can be stated as

$$\left.\begin{aligned} \sigma_f\cdot\mathbf{n} &= \sigma_s\cdot\mathbf{n} \\ \mathbf{v}_f &= \mathbf{v}_s \end{aligned}\right\} \text{ on } \Gamma^t,$$

and will be used at all interfaces in FSI simulations. Kinematic or dynamic boundary conditions will be needed on the other boundaries as well, but will differ depending on the problem considered.

3.8 Coupling Fluid Flow with Poroelasticity

In a similar fashion to the Fluid-Structure interaction problem, and with the simplifications assuming a small filtration velocity, the Biot problem together with

Navier-Stokes equations consists of solving:

$$\begin{aligned} \rho_f\Big(\frac{\partial \mathbf{v}_f}{\partial t} + ((\mathbf{v}_f - \mathbf{w})\cdot\nabla)\mathbf{v}_f\Big) - \nabla\cdot\sigma_f(\mathbf{v}_f, p_f) = 0 \quad &\text{in } \Omega_f^t \\ \nabla\cdot\mathbf{v}_f = 0 \quad &\text{in } \Omega_f^t \\ \nabla^2\mathbf{U} = 0 \quad &\text{in } \Omega_f^t \end{aligned}$$

$$\begin{aligned} \rho_p\frac{\partial \mathbf{v}_s}{\partial t} + \rho_p(\mathbf{v}_s\cdot\nabla)\mathbf{v}_s - \nabla\cdot\sigma_s(\mathbf{U}) + \nabla p_s = 0 \quad &\text{in } \Omega_s^t \\ \rho_p\frac{\partial \mathbf{v}_s}{\partial t} + \rho_p(\mathbf{v}_s\cdot\nabla)\mathbf{v}_s + K^{-1}\mathbf{q} + \nabla p_s = 0 \quad &\text{in } \Omega_s^t \\ \nabla\cdot(\mathbf{v}_s + \mathbf{q}) = 0 \quad &\text{in } \Omega_s^t \end{aligned}$$

Boundary conditions at the interface for the given problem have been discussed over the years, and in 1967 Beavers and Joseph [42] published a paper describing experiments investigating the slip rate at a horizontal permeable wall located at $y = 0$ with fluid flow above the porous medium. According to Beavers and Joseph, the boundary condition at the wall $y = 0$ should be

$$\frac{\partial v_f}{\partial y} = \frac{\alpha_{\mathrm{BJ}}}{K^{1/2}}(v_f - q), \tag{3.23}$$

where v_f is the fluid velocity tangential to the plane, q is the seepage or filtration velocity in the porous medium, K is the permeability, and α_{BJ} is a constant depending on the material parameters of the porous medium close to the boundary. The derivative on the left hand side of equation (3.23) should be evaluated just above the plane, while q should be evaluated just below the plane. In 1971 Saffmann [43] generalized the problem to other geometries, showing that the filtration velocity q could be left out of the equation only adding errors of order $\mathcal{O}(K)$. Jones, (1973) [44] assumed shortly afterwards that the velocity jump was proportional to the shear stress rather than velocity shear. These additions to the original boundary condition proposed by Beavers and Joseph (known as the Beavers-Joseph-Saffmann (BJS) condition) was used in spinal canal models by Drøsdal:

$$2\mathbf{n}\cdot\epsilon(\mathbf{v}_f)\cdot\tau = \alpha_{\mathrm{BJ}}K^{-1/2}\mathbf{v}_f\cdot\tau$$

and showed to have minimal effect on key value measurements such as filtration velocity in the cord as well as fluid velocity in both the SAS and inside the syrinx. (Values changed by $10^{-4}\%$ for α_{BJ} ranging from 0 to 1). This condition is therefore omitted in this thesis.

As in the FSI case, we assume conservation of mass and continuity of stresses at the interface. The boundary condition is related through the velocities and the Darcy flux at the boundary:

$$\left.\begin{aligned} \mathbf{v}_f &= \mathbf{v}_s + \mathbf{q} \\ \sigma_f\cdot\mathbf{n} &= \sigma_s\cdot\mathbf{n} - p_p\mathbf{n} \end{aligned}\right\} \text{ on } \Gamma^t \tag{3.24}$$

Strictly speaking, mass conservation does not necessarily imply the tangential velocitites to be continuous at the interface, and the transition in tangential velocity is what the BJS-condition tries to capture. However, as we shall see later, with the limitiations by using continuous functions in the computational modeling the tangential velocities will also have to be continuous. This limitation is also the case for the pressure, and as pointed out by Nield and Bejan (2013) [34] these assumptions together with the BJS-condition results in an overdetermined system. The pressure will be continuous on the microscopic scale, but only approximately continuous on the macroscopic (averaging) scale. Despite these limitations, we stick with the boundary conditions (3.24) assuming, as showed on porous flow, the BJS-condition barely alters the solution.

Chapter 4

Numerical Methods

4.1 The Finite Element Method

The theory presented in this section is partly inspired by the works of Langtangen in Finite Element Method - INF5620 lecture notes" [45]
Consider the Poisson-equation with generalized boundary conditions:

$$-\nabla^2 v = f \quad \text{in } \Omega \tag{4.1}$$

$$v = v_0 \quad \text{on } \partial\Omega_D \tag{4.2}$$

$$\frac{\partial v}{\partial n} = g \quad \text{on } \partial\Omega_N \tag{4.3}$$

Here, $\Omega \in \mathbb{R}^d$ is a domain, $v = v(x)$ is an unknown function, and f is a source function. The boundary, $\partial\Omega$ is divided into two parts: $\partial\Omega_D$ for the Dirichlet boundary condition, and $\partial\Omega_N$ for the Neumann condition.

4.1.1 Variational formulation

Equation (4.1) is known as the strong form of problem. In order to obtain the weak formulation, we multiply the equation with a test function, $\phi \in \hat{V}$, where $\hat{V}$ is some function space, and integrate over the domain. Weak formulations allow differential equations to be transformed into systems of linear equations. In the rest of this text, the following notation is used for the inner product of two functions

$$(v, \phi)_\Omega = \int_\Omega v\,\phi \,\mathrm{d}x.$$

By multiplying (4.1) with a test function, ϕ and integrating over the domain, the weak form is obtained:

$$(\nabla^2 v + f, \phi)_\Omega = 0 \quad \forall\, \phi \in \hat{V}.$$

We are now searching for a v to satisfy the weak form instead of the strong. This equation should hold for all ϕ in the function space $\hat{V}$. The trial function does not

necessarily have to lie in the same function space, in general $v \in V$.

In this thesis we will use two Sobolev spaces (named after the Russian mathematician Sergei Sobolev) widely used in Finite Element computing. For these definitions to be valid, we assume that the functions v are all **locally integrable** and in the case of definition (4.2), has one **weak derivative**. For more details on weak derivatives and the generalized concept of Sobolev spaces and functional analysis, we refer to the textbook by Brenner and Scott [46].

Definition 4.1 *Let Ω be an open subset of $\mathbb{R}$ with a piecewise smooth boundary. We then define the L^2-norm as follows*

$$||v||_{L^2(\Omega)} = (\int_\Omega v^2 \mathrm{d}x)^{\frac{1}{2}}$$

The corresponding L^2-space is defined via

$$L^2(\Omega) = \{v : \Omega \to \mathbb{R} | \int_\Omega v^2 \mathrm{d}x < \infty\}$$

Definition 4.2 *Let Ω be an open subset of $\mathbb{R}$ with a piecewise smooth boundary. We then define the H^1-norm as follows*

$$||v||_{H^1(\Omega)} = (\int_\Omega [v^2 + (\nabla v)^2] \mathrm{d}x)^{\frac{1}{2}}$$

The corresponding H^1-space is defined via

$$H^1(\Omega) = \{v : \Omega \to \mathbb{R} | \int_\Omega [v^2 + (\nabla v)^2] \mathrm{d}x < \infty\}$$

In other words, using functions from these spaces, we are guaranteed that the integrals involved in the variational form are bounded. By the divergence theorem (3.1), we can state the variational problem as follows:
find $v \in V$ such that

$$(\nabla v, \nabla \phi)_\Omega = (f, \phi)_\Omega + (g, \phi)_{\partial\Omega_N} \quad \forall \phi \in \hat{V} \tag{4.4}$$

Where we have used that $\frac{\partial v}{\partial n} = g$ on $\partial\Omega_N$. (4.4) is known as the variational formulation of the Poisson problem. The left hand side is known as the bilinear form while the right hand side is the linear form. In generic form the equation can be written

$$a(v, \phi) = L(\phi) \tag{4.5}$$

The first derivative of v appears in the variational form. A common choice is then

$$V := \{v \in H^1(\Omega) : v = v_0 \text{ on } \partial\Omega_D\}$$
$$\hat{V} := \{v \in H^1(\Omega) : v = 0 \text{ on } \partial\Omega_D\}$$

In other words, the trial and test functions are in the same function space, except on the boundary.

4.1.2 Finite elements

The next step is to approximate v with a sum of basis functions in the finite-dimensional function space, $V = \text{span}\{\phi_0, \phi_1, ..., \phi_N\}$. Here, ϕ_i represents the basis functions and we search for a solution $v_h \in V$ such that v_h can be written as a linear combination of the basis functions. The first step in the finite element method consists of dividing the domain into smaller parts

$$\Omega = \Omega_0 \cup \Omega_1 \cup ... \cup \Omega_{N_e}$$

where N_e is the number of elements. Each element have a number of nodes within them depending on what type of basis functions to be used. Let us first consider the continuous Galerkin basis functions in a one-dimensional domain. There is exactly one basis function for each node located at x_i. These basis functions have the following property:

$$\phi_i(x_j) = \begin{cases} 1 & \text{for } i = j \\ 0 & \text{for } i \neq j \end{cases} .$$

That is, the basis functions ϕ_i are zero on all nodes except at node i. Each ba-

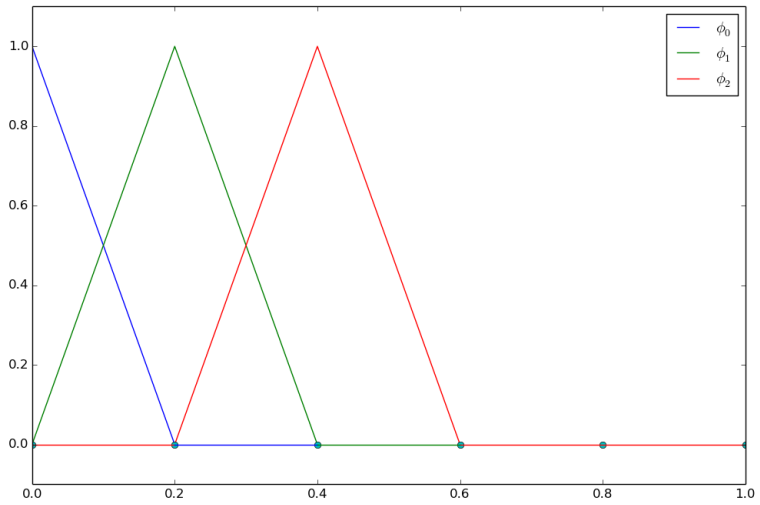

Figure 4.1: The three first linear basis functions on the unit interval divided uniformly into 5 elements, $\Omega_0 = [0, 0.2], \Omega_1 = [0.2, 0.4]$ and so on. In the case of Dirichlet Boundary conditions at $x = 0$, ϕ_0 will not be included in the function space

sis function is constructed by taking the Lagrange-polynomial with value 1 at the given node and 0 on the neighboring nodes. Note that the basis functions are two Lagrange-polynomials "pieced together" at the node where its value is 1. On the rest of the domain, the basis functions are defined to be 0.

Now, let us consider the original problem (4.1)-(4.3) in scalar form. We start by approximating v as a linear combination of all the basis functions.

$$v_h = \sum_{i=0}^{N} c_i \phi_i.$$

The definitions of v_h and V now give rise to a linear system. Using the Einstein summation convention, $x_i\, y_i = \sum_{i=0}^{N} x_i y_i$, the discretized version of (4.4) is now written

$$-c_i(\nabla\phi_i, \nabla\phi_j)_\Omega = (f, \phi_j)_\Omega - (g, \phi_j)_{\partial\Omega_N}.$$

In the case of Dirichlet boundary conditions, all test functions ϕ_j will take the value 0 on $\partial\Omega_D$, so the linear system will be adjusted to take these boundary conditions into account.
The system can be written in matrix form, and in the end the problem consists of solving the linear system

$$A_{i,j}c_i = b_j.$$

4.2 The FEniCS software

When the variational form has been carried out, implementation in FEniCS is relatively simple. The following examples and programs in this thesis are all written in Python. When programming with Python, we first need to import DOLFIN to access the DOLFIN library, containing classes convinient and efficient for finite element computing. In Python the full library can be imported using

```
from dolfin import *
```

Now, let us focus our attention on solving the following problem:

$$\begin{aligned} \nabla^2 v &= 20x \quad \text{in } \Omega \\ v(0,y) = 0, &\quad v(1,y) = 1 \\ \frac{\partial v(x,0)}{\partial n} &= \frac{\partial v(x,1)}{\partial n} = 0, \end{aligned}$$

where Ω is the unit square, $\Omega = [0,1] \times [0,1]$.

The first step is to define the computational mesh:

```
mesh = UnitSquareMesh(10,10)
```

The class UnitSquareMesh initializes a mesh with triangular cells. The mesh consists of $n \times m$ squares depending on the arguments n and m, sent into the constructor. Each of these squares are divided on the diagonal to form two triangles, and these triangles are the computational cells. In this case we get the unit square divided into 10×10 smaller squares and thus the total number of triangles, or cells, will be 200.
The next thing to do is to define an appropriate function space for the test functions. The solution will be a linear combination of these functions and will be in (almost) the same function space.

```
V = FunctionSpace(mesh,'CG',1)
```

The function space needs a domain, type of element, and the degree of the element. In this case we use continuous Galerkin elements (CG) with degree 1. These basis functions are visualized in Figure 4.1
We can then define our test and trial functions v and ϕ through

```
v = TrialFunction(V)
phi = TestFunction(V)
```

Note that the test and trial functions seem to be in the exact same function space. This is the case except when imposing Dirichlet boundary conditions. The functions f, v_0, and g can be defined by using the classes Constant or Expression. We set $f = 20x$, use the Dirichlet boundary conditions $v(0, y) = 0$, $v(1, y) = 1$, and the Neumann conditions $\frac{\partial v(x,0)}{\partial n} = \frac{\partial v(x,1)}{\partial n} = 0$. The homogeneous Neumann condition is simple in the finite element method as the terms appearing after integration by parts can be dropped. If this is not the case, we can insert g for $\frac{\partial u}{\partial n}$ on the boundary integral appearing in the variational form. When the Neumann conditions are incorporated this way we say that the boundary conditions are weakly imposed. Functions (or classes) describing the boundaries must also be defined:

```
f = Expression('20*x[0]')
def boundary0(x,on_bnd):
        return on_bnd and near(x[0],0.0)
def boundary1(x,on_bnd):
        return on_bnd and near(x[0],1.0)

bc0 = DirichletBC(V,0.0,boundary0)
bc1 = DirichletBC(V,1.0,boundary1)
bcs = [bc0,bc1]
```

Note that "x[0]" means first dimension in space, "x[1]" means second dimension and so on. The Dirichlet conditions are put in a list. Next, the variational form is defined, and when solving for a function v, the boundary conditions are added to the "magic" solve() function.

```
F = inner(grad(v),grad(phi))*dx - inner(f,phi)*dx
v = Function(V)
solve(lhs(F)==rhs(F),v,bcs)
plot(v)
```

The functions lhs and rhs separate the form F into the left hand side, equivalent to the bilinear form, and to the right hand side, equivalent to the linear form. Specifying the form F right away is convenient when the equations are short and simple. In writing these forms, the Unified Form Language (UFL) is used which is imported with DOLFIN. If we want to relate the code to the mathematics as written in equation (4.5), we can define these forms manually.

```
a = inner(grad(v),grad(phi))*dx
L = inner(f,phi)*dx
v = Function(V)
solve(a==L,v,bcs)
```

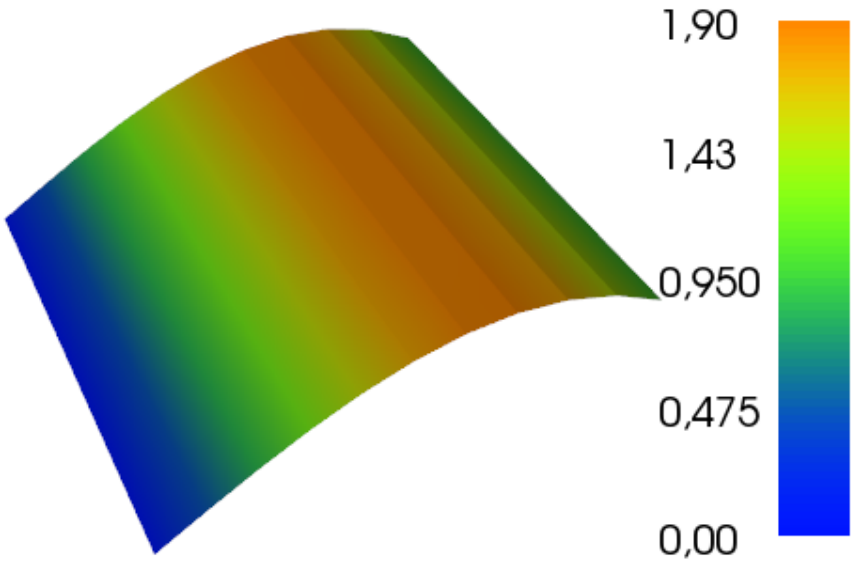

Figure 4.2: Slightly rotated plot of the computed solution. The solution is independent of y-position, as expected.

4.3 Womersley Flow

In the cardiovascular system, pressure pulses travel along different blood vessels such as veins, capillaries, and the aorta. These types of pulsating flows are named Womersley flow after John R. Womersley on his work with pulsatile blood flow [47]. The characteristics and velocity profile of the flow depend of several parameters such as the length of the tube or channel, pulsation frequency and fluid properties. In the end, the ratio between transient inertial forces and viscous forces is the fundamental difference separating flow patterns in pulsating flow. To this end the Womersley number α is defined as:

$$\alpha^2 = \frac{\text{transient inertial force}}{\text{viscous force}} = \frac{\rho\omega V}{\mu V L^{-2}} = \frac{L^2\omega\rho}{\mu},$$

where ρ is the fluid denisty, μ is the dynamic viscosity, L is a length scale and ω is the pulsation frequency. In the 2D-model presented here, the modeling of SAS around the spinal cord consists of two channels where the Womersley number

$$\alpha = L\big(\frac{\omega\rho}{\mu}\big)^{\frac{1}{2}},$$

would have a large impact on flow characteristics. A low Womersley number (typically $\alpha < 1$) suggests a low frequency, and hence the flow will develop a velocity profile close to a parabola at each cycle. When α is large ($\alpha > 10$) the inertial forces dominate and more complicated phenomena such as bidirectional flow, i.e. flow in opposite directions over a cross section, could occur.

Even though the flow should be aligned with the channel due to the incompressibility constraint, pulsating flow tends to give rise to some horizontal or radial flow with the boundary conditions previously described due to numerical errors. This error is associated with the Neumann condition on the boundary. We will return to this issue in the next subsection. For now we assume the following conditions to hold:

$$\begin{aligned} \mathbf{v}\cdot\tau = 0 \text{ on } \partial\Omega_{\text{in}} \\ \mathbf{v}\cdot\tau = 0 \text{ on } \partial\Omega_{\text{out}}, \end{aligned} \tag{4.6}$$

where τ is the tangential vector on the boundary surface, and $\partial\Omega_{\text{in}}$ and $\partial\Omega_{\text{out}}$ denotes the inlet and outlet of the channel.

If the channel walls are denoted $\partial\Omega_{\text{w}}$, the pulsating velocity and pressure should satisfy

$$\begin{aligned} \frac{\partial\mathbf{v}}{\partial t} + (\mathbf{v}\cdot\nabla)\mathbf{v} = \nabla\cdot\sigma \qquad & \text{in } \Omega, \\ \nabla\cdot\mathbf{u} = 0 \qquad & \text{in } \Omega, \\ \mathbf{v} = 0 \qquad & \text{on } \partial\Omega_{\text{w}}, \\ \mu\frac{\partial\mathbf{v}}{\partial n} - p\mathbf{n} = p_{\text{in}}(t)\mathbf{n} \text{ and } \mathbf{v}\cdot\tau = 0 \qquad & \text{on } \partial\Omega_{\text{in}}, \\ \mu\frac{\partial\mathbf{v}}{\partial n} - p\mathbf{n} = p_{\text{out}}(t)\mathbf{n} \text{ and } \mathbf{v}\cdot\tau = 0 \qquad & \text{on } \partial\Omega_{\text{out}}. \end{aligned}$$

We now aim to solve the problem 4.3 numerically to validate the CFD solver. In FEniCS, a mixed function space, consisting of one vector and one scalar function space, can be used to solve coupled equations. The implementation is explained more in detail in section 5.2.5.

Exact solutions exists to both the channel and pipe cases. Langlois and Deville [48] have derived several solutions to equations of viscous flow, including channel flow with a pulsatile pressure gradient as above. We now add a oscillating pressure gradient so that

$$-\frac{1}{\rho}\frac{\partial p}{\partial x} = -C\cos(\omega t), \tag{4.7}$$

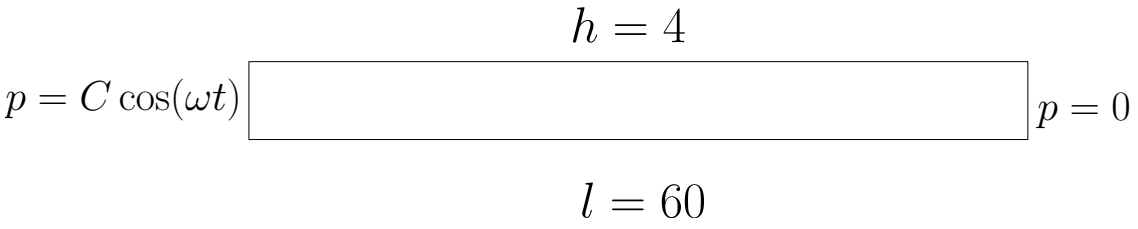

Figure 4.3: Schematic of Womersley flow with dimensions as in the upper spinal cord

where C is a constant describing the strength of the pulse. Due to the assumption of axial flow only, the momentum equation in x-direction gives:

$$\frac{\partial v_1}{\partial t} = -\frac{1}{\rho}\frac{\partial p}{\partial x_1} + \nu\frac{\partial^2 v_1}{\partial x_2^2}. \tag{4.8}$$

With the relation (4.7), the solution presented by Langlois and Deville is:

$$v_1 = -\frac{C}{\omega}\left[\left(1 - \frac{f_1(\omega, x_3)}{f_3(kh)}\right)\sin(\omega t) - \frac{f_2(\omega, x_3)}{f_3(kh)}\cos(\omega t)\right] \tag{4.9}$$

where

$$\begin{aligned} k &= \sqrt{\frac{\omega}{2\nu}}, \\ cc(x) &= \cos(x)\cosh(x), \\ ss(x) &= \sin(x)\sinh(x), \\ f_1(\omega, x_3) &= cc(kx_3)cc(kh) + ss(kx_3)ss(kh), \\ f_2(\omega, x_3) &= cc(kx_3)ss(kh) - ss(kx_3)cc(kh), \\ f_3(\omega) &= cc^2(\omega) + ss^2(\omega). \end{aligned}$$

We found some descrepancy in the computed and analytical solutions, therefore an opportunity to use the symbolic Python package Sympy arose. The package lets the user define symbols to work with. Regular multiplication and general Python functions can also be used. In order to verify the solution, we assume (4.9) to be the correct velocity, solve equation (4.8) for $\frac{\partial p}{\partial x}$, and expect to obtain the relation (4.7).

```
from sympy import *
x3, C, x, h, t, w, nu = symbols('x3 C x h t w nu')
k = sqrt(w/(2*nu))
def cc(x):
        return cos(x)*cosh(x)
.
.
.

f3 = cc(w)**2 + ss(w)**2

u = -C/w*((1-f1/f3)*sin(w*t) - f2/f3*cos(w*t))   # presented solution
d2u = nu*diff(diff(u,x3),x3)
dt = diff(u,t)

print simplify(d2u-dt)
```

From (4.8) the code snippet should print the already known pressure gradient divided by the density

$$\frac{1}{\rho}\frac{\partial p}{\partial x_3} = C\cos(\omega t),$$

which was not the case when using the solution (4.9).
When using the solution

$$v_1 = -\frac{C}{\omega}\left[\left(1 - \frac{f_1(\omega, x_3)}{f_3(kh)}\right)\sin(\omega t) + \frac{f_2(\omega, x_3)}{f_3(kh)}\cos(\omega t)\right],$$

where the sign before the cos-term is changed, the code snippet gave the correct pressure gradient, and hence this solution was used when error-estimates were investigated.

4.3.1 Error estimates

To understand the problems arising with Neumann Conditions on both inlet and outlet we first consider the convection-diffusion equation.

$$\begin{aligned} -\mu\nabla^2 u + \mathbf{v}\cdot\nabla u &= f \quad \text{in } \Omega \\ u &= u_0 \text{ on } \partial\Omega_D \\ \mu\frac{\partial u}{\partial n} &= g \quad \text{on } \partial\Omega_N, \end{aligned} \tag{4.10}$$

where u is an unknown function, $\mathbf{v}$ is a prescribed velocity, μ is a diffusion constant and f is a source term. For the sake of simplicity we assume incompressibility. The weak formulation reads:

Find $u \in H^1_{u_0}$ *such that*

$$\mu(\nabla u, \nabla \phi)_\Omega + (\mathbf{v} \cdot \nabla u, \phi)_\Omega = (f, \phi)_\Omega + (g, \phi)_{\partial\Omega_N} \text{ for all } \phi \in H^1_0.$$

Where the subscript on the two H-spaces indicate the values for functions on $\partial\Omega_D$ for these spaces.

What has not been mentioned so far is the existence and uniqueness of the finite element solutions. To establish some concepts addressing these questions we let V denote a function space. V is now a Hilbert space, which has to satisfy given conditions on the associated inner product, where the inner product is denoted $(\cdot, \cdot)_V$ and the norm $||\cdot||_V$, (see e.g. Elman et al [49]). We define the following:

Definition 4.3 *(Coercivity)*
A bilinear form $a(\cdot, \cdot)$ *is said to be coercive with respect to the norm* $||\cdot||_V$ *if there is a positive constant* γ *such that*

$$a(u, u) \geq \gamma ||u||^2_V \text{ for all } u \in V$$

Definition 4.4 *(Continuity)*
A bilinear form $a(\cdot, \cdot)$ *is continuous with respect to the norm* $||\cdot||_V$ *if there is a positive constant* Γ *such that*

$$a(u, \phi) \leq \Gamma ||u||_V ||\phi||_V \text{ for all } u, \phi \in V$$

A linear functional $L(\phi)$ *is continuous with respect to* $||\cdot||_V$ *if there is a constant* Λ *such that*

$$L(\phi) \leq \Lambda ||\phi||_V \text{ for all } \phi \in V$$

In order to have a well posed problem, and ensure the existence of a unique solution $u \in V$ satisfying

$$a(u, \phi) = L(\phi) \text{ for all } \phi \in V,$$

$a(\cdot, \cdot)$ and $L(\cdot)$ have to satisfy these criteria. This is known as the Lax-Milgram lemma. If these criteria are satisfied, the following a priori error estimates are obtained:

$$||v - v_h||_{L^2} \leq C_1 h^{t+1} ||v||_{t+1}$$

$$||v - v_h||_{H^1} \leq C_2 h^t ||v||_{t+1}$$

where h is the cell size, t is the degree of the polynomial on the elements, v is the analytical solution and v_h is the computed solution. The convergence rate can then be computed as

$$\frac{\ln(\frac{e^{n+1}}{e^n})}{\ln(\frac{h^{n+1}}{h^n})}.$$

The convection term

$$c(u,\phi) = (\mathbf{v}\cdot\nabla u, \phi)_\Omega \tag{4.11}$$

makes the problem (4.10) more challenging to solve numerically than the Poisson-problem (4.1),(4.2), (4.3). In light of definitions 4.3 and 4.4, we apply the divergence theorem to equation (4.11):

$$\begin{aligned} c(u,\phi) &= \int_\Omega \phi\mathbf{v}\cdot\nabla u \mathrm{d}x \\ &= -\int_\Omega u\mathbf{v}\cdot\nabla\phi \mathrm{d}x - \int_\Omega u\phi\nabla\cdot\mathbf{v}\mathrm{d}x + \int_{\partial\Omega_N} u\phi\mathbf{v}\cdot\mathbf{n}\mathrm{d}S \\ &= -c(\phi,u) + \int_{\partial\Omega_N} u\phi\mathbf{v}\cdot\mathbf{n}\mathrm{d}S, \end{aligned} \tag{4.12}$$

where the last step follows from the assumption of incompressibility. Rearrangement of (4.12) yields:

$$c(u,u) = \frac{1}{2}\int_{\Omega_N} u^2\mathbf{v}\cdot\mathbf{n}\mathrm{d}S.$$

It is obvious that a Neumann condition on the inflow boundary, where $\mathbf{v}$ and $\mathbf{n}$ points in opposite directions, makes a negative contribution to the bilinear form $a(u,u)$. Therefore, coercivity can not be completely ensured, and stability typically depends on the magnitude of the velocity at the inlet.

In several problems, prescribing Neumann conditions are simpler than providing inlet velocities. The pressure is set as a scalar value and can be assumed to have no spatial variation over the boundaries if the model has flat surfaces with normals aligned with the longitudinal axis on the inlet and outlet.

4.3.2 A penalty method on the boundary

Barth and Carey [50] have described a penalty method for ensuring the constraint (4.6). This was needed as horizontal flow at, and close to the boundaries caused problems interacting with the elastic spinal cord. The penalty method consists of adding a term at the relevant boundaries, penalizing parts where the boundary condition do not hold. For the velocity, we want $\mathbf{v} - (\mathbf{v}\cdot\mathbf{n})\mathbf{n} = 0$ on the boundary, therefore the first variation of the least squares penalty functional is added to

the variational formulation. This has been done in all simulations with Neumann boundary conditions at the inlet in this thesis. The penalty functional is given as

$$I(\mathbf{v}) = \frac{1}{2\epsilon}\int_{\partial\Omega_p} \big[\mathbf{v} - (\mathbf{v}\cdot\mathbf{n})\mathbf{n}\big]\cdot\big[\mathbf{v} - (\mathbf{v}\cdot\mathbf{n})\mathbf{n}\big]\mathrm{d}S,$$

where $0 < \epsilon << 1$ is the penalty parameter. The contribution from the first variation will be

$$I'(\mathbf{v})(\mathbf{\Phi}) = \frac{1}{\epsilon}\int_{\partial\Omega_p} \big[\mathbf{v} - (\mathbf{v}\cdot\mathbf{n})\mathbf{n}\big]\cdot\big[\mathbf{\Phi} - (\mathbf{\Phi}\cdot\mathbf{n})\mathbf{n}\big]\mathrm{d}S.$$

This term will clearly contribute positively to the bilinear form, and the penalty parameter should ensure that this contribution is large. The method is tested on the coupled CFD solver, first with one time step of the Backwards Scheme and gradually refinement of the rectangular mesh consisting of N elements on each boundary. The time step is small ($\Delta t = 10^{-6}$), so the error introduced by the time discretization is negligible.

N	dofs	$\|\|v - v_h\|\|_{L^2}$	rate	$\|\|v - v_h\|\|_{H^1}$	rate
4	187	1.00e+00	–	6.65e+00	–
8	659	1.50e-01	2.739	1.95e+00	1.768
16	2467	1.91e-02	2.977	4.95e-01	1.981
32	9539	2.39e-03	2.997	1.24e-01	1.997
64	37507	2.99e-04	2.998	3.10e-02	1.999

Table 4.1: Errors P2-P1 elements

N	dofs	$\|\|v - v_h\|\|_{L^2}$	rate	$\|\|v - v_h\|\|_{H^1}$	rate
4	419	1.42e+01	–	1.43e+02	–
8	1539	7.84e-01	4.180	1.57e+01	3.186
16	5891	4.75e-02	4.045	1.90e+00	3.047
32	23043	2.97e-03	3.999	2.38e-01	3.000
64	91139	1.86e-04	3.999	2.97e-02	2.999

Table 4.2: Errors P3-P2 elements

Some error is also introduced by the time discretization. The Backward-Euler scheme is motivated by Taylor expansion around the time-point $t + \Delta t$ of a time dependent function $f(t)$

$$f(t) = f(t + \Delta t) - \Delta t f'(t + \Delta t) + \mathcal{O}(\Delta t^2),$$

which shows that the error introduced by one time step should be proportional to Δt^2. On the other hand, if we want to progress until a given end time T, the number of steps will be $N = \frac{T}{\Delta t}$. The error each time step is $\mathcal{O}(\Delta t^2)$, so the accumulated

error introduced by the time discretization will be $\mathcal{O}(\Delta t)$. We test both these error estimates on the Womersley flow and the results are summarized in table 4.3 and table 4.4. It should be noted that no a priori error estimate has been done for the H^1-norm of the error in relation to the time step. However, it should be expected to decrease with Δt. Similarly to the previous tables, we used a fine grid (N=128) so the error introduced by spatial discretization is negligible in comparison.

Δt	dofs	L2 error	rate	H1 error	rate
1.00e-01	148739	2.08e+02	–	3.26e+02	–
5.00e-02	148739	3.48e+01	2.581	6.72e+01	2.278
2.50e-02	148739	6.63e+00	2.394	1.58e+01	2.089
1.25e-02	148739	1.44e+00	2.203	4.02e+00	1.974

Table 4.3: Errors, one time step. P2-P1 elements.

Δt	dofs	L2 error	rate	H1 error	rate
1.00e-01	148739	2.08e+02	–	3.26e+02	–
5.00e-02	148739	9.65e+01	1.111	1.58e+02	1.045
2.50e-02	148739	4.63e+01	1.058	7.81e+01	1.017
1.25e-02	148739	2.27e+01	1.030	3.88e+01	1.007

Table 4.4: Errors at T=0.1. P2-P1 elements.

In figure 4.4, the effect of adding the penalty term is shown in comparison to the regular method. We have used a strong driving force (C = 1000 in equation (4.7)), and compared the two methods at t = 0.1 with $\Delta t = 0.001$. Velocities are approximately 100 in magnitude so the velocities in y-direction are small ($\approx 0.1\%$ and $\approx 0.02\%$ of the magnitude), but accumulates over time in the regular method.

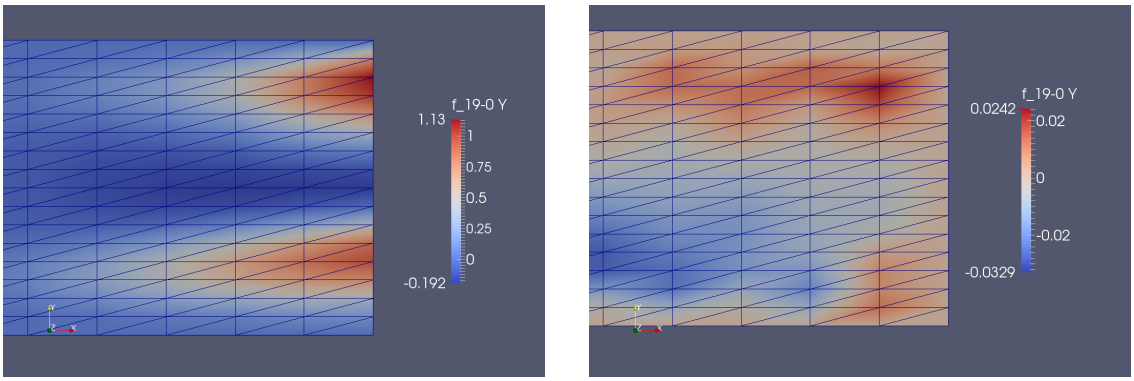

Figure 4.4: Velocity distribution in y-direction without (left) and with (right) the penalty term at the outlet.

Chapter 5

Numerical methods for FSI

5.1 A benchmark FSI problem

Within CFD, a benchmark is a configuration or a test case which should help to validate and compare different numerical methods and code implementations. A classical Fluid Dynamics problem regarding flow around a circular cylinder has been under vast research the last 50 years, working as a test case for both laminar and turbulent flows. One of the most cited benchmark proposals for this case is the problem described by Michael Schäfer et. al in 1996 [51]. Schäfer's research group still focus on these kinds of problems. In 2006 one of the co-authors of the 1996 paper, Stefan Turek, together with Jaroslav Hron proposed a similar benchmark for FSI solvers, consisting of the exact same domain and rigid cylinder, but now with an elastic flag attached to it [52].
The first results presented will contain a validation of the present FSI-solver implemented in FEniCS compared to the results of Turek and Hron in their benchmark proposal. These results are not directly comparable for large deformations. We have used a linear elasticity model while the reference results are results from a nonlinear constitutive model (St. Venant-Kirchhoff)
A proper validation of a FSI solver requires separate verification of the fluid and structural parts as well as coupled tests. In the present study we solve the system of equations with a *monolithic* approach, i.e. full coupling between the fluid and solid. The alternative would be a *partitioned* approach, where the fluid and solid equations are solved separately. For instance, one can solve the fluid equations independently and then proceed by solving the solid equation with prescribed stress on the interface computed from the fluid solution. Iteration back and forth would be needed until convergence.
The fully coupled monolithic scheme is usually preferred with respect to accuracy and stability. Also, when the systems are strongly coupled in nature, i.e. the solid movement is affected by the fluid movement and vice versa, a monolithic scheme would be advantageous. The partitioned approach, on the other hand, can benefit from numerous previous studies where efficiency and stability for various solution techniques have been investigated. See e.g. [53] for a short review. In addition, solving many smaller matrix systems will be way faster than solving one large system with the same number of unknowns.

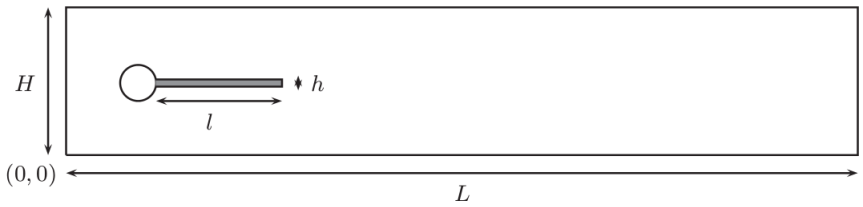

Fig. 1. Computational domain

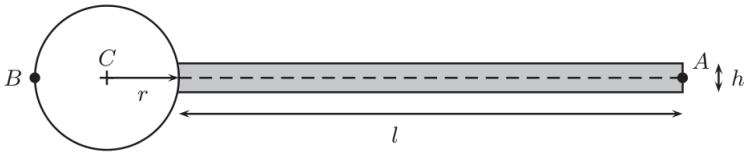

Fig. 2. Detail of the structure part

Figure 5.1: The Domain as published in [52]

5.1.1 Problem Set Up

The origin is set at the bottom left corner. We also set:
- The channel height, H = 0.41
- The channel length, L = 2.5
- The circle center C = (0.2,0.2)
- The right bottom corner of the elastic structure has position (0.6,0.19)
- The elastic structure has length, l=0.35 and heigth h=0.02

- At the left boundary, the inlet, of the channel, we set a prescribed parabolic velocity profile

$$\mathbf{v}_{\text{in}}(0, y) = 1.5\bar{v_0}\frac{y(H-y)}{(\frac{H}{2})^2}$$

- In the case of unsteady flow a smooth increase in time is used:

$$\mathbf{v}_{\text{in}}(t, 0, y) = \begin{cases} \mathbf{v}_{\text{in}}(0, y)\frac{1-\cos(\frac{\pi}{2}t)}{2} & \text{if } t < 2.0 \\ \mathbf{v}_{\text{in}}(0, y) & \text{otherwise} \end{cases}$$

- On the outlet, the condition $\sigma \cdot \mathbf{n} = 0$ is applied
- On rigid walls the no-slip condition is used
- On the interface, Γ^t, the following coupling conditions are applied:

$$\left.\begin{aligned} \sigma_f \cdot \mathbf{n} &= \sigma_s \cdot \mathbf{n} \\ \mathbf{v}_f &= \mathbf{v}_s \end{aligned}\right\} \text{ on } \Gamma^t$$

In addition to the interface Γ^t it may be convenient to define the other boundaries as well. We let $\partial\Omega_f^t$ consist of the outer rectangle and the part of the circle boundary in contact with the fluid, and the solid boundary, $\partial\Omega_s^t$ consist of the circle boundary in contact with the solid.

5.2 FSI using the Finite Element Method

A solver was implemented from scratch in Python using the DOLFIN library even though FSI solvers within the FEniCS framework already exists (e.g. Unicorn or CBC.twist). For instance, Selin [54] implemented a partitioned solver in FEniCS in his PhD-thesis, using the already existing modules for solving fluid flow and structural deformations separately (CBC.Flow and CBC.Twist). The approach we have used is aimed to explain how a simple FSI model can be implemented in FEniCS. If the underlying concepts are understood, the equations can be changed whether we want the spinal cord to be porous, elastic, poroelastic or viscoelastic. The use of two separate solvers is also problematic for the monolithic approach, when all equations should be solved simultaneously. On the other hand, solvers implemented by experienced and skilled research groups will probably be more efficient and already validated.

In the rest of this section, we give a brief explanation of the mathematics and implementation in FEniCS. Thanks to UFL, we saw in section 4.2 the close link between code and mathematics:

$$a(\mathbf{v}, \Phi) = (\nabla\mathbf{v}, \nabla\Phi)_\Omega$$
$$L(\mathbf{v}) = (\mathbf{f}, \Phi)_\Omega$$

Translates to

```
a = inner(grad(v),grad(phi)*dx
L = inner(f,phi)*dx
```

In deriving variational forms, we try to keep this close link by recalling the symbols used for velocity ($\mathbf{v}$), total displacement ($\mathbf{U}$), pressure (p), and mesh velocity ($\mathbf{w}$). Also, recall that in the solid the mesh moves exactly with the velocity of the structure, and thus $\mathbf{w}_s = \mathbf{v}_s$

5.2.1 Temporal discretization

In order not to overload this thesis with notation and superscripts, we have used the notation $\mathbf{v} := \mathbf{v}^{n+1}$ to denote the value of a function at the next time-step. Similarly, we define $\mathbf{v}^{(\mathbf{1})} := \mathbf{v}^n$ to denote the (known) value of a function at the present time step.

The total displacement $\mathbf{U}$ can be expressed as a function of the displacement from the previous time step, $\mathbf{U}^{(1)}$, and the mesh velocity $\mathbf{w}$. We have used an implicit scheme in time, i.e, $(\frac{\partial\mathbf{v}}{\partial t})^{n+1} = \frac{\mathbf{v}^{n+1}-\mathbf{v}^n}{\Delta t}$, and $\frac{\partial\mathbf{U}}{\partial t}^{(n+1)} = \frac{\mathbf{U}-\mathbf{U}^{(1)}}{\Delta t} = \mathbf{w}$.

5.2.2 Spatial discretization

When dealing with nonlinear equations, such as the Navier-Stokes equations, *linearization* is needed in order to solve these. In nonlinear terms, we simply replace one (or more) of the unknown $\mathbf{v}$'s with a "guess" to get an equation linear in $\mathbf{v}$. This guess is denoted as $\mathbf{v}^{(0)}$. Since we have three unknown functions, we use a mixed function space with three function spaces, Φ, η and Ψ. We now aim to solve the FSI system as presented in section 3.7. In the fluid we multiply the momentum equation with Φ, the continuity equation with η and the equation for mesh velocity with Ψ and integrate over the domain in its *current* configuration, Ω^t. In the fluid, this yields:

$$\frac{\rho_f}{\Delta t}(\mathbf{v},\Phi)_{\Omega_f} + \rho_f(((\mathbf{v}-\mathbf{w})\cdot\nabla)\mathbf{v}^{(0)},\Phi)_{\Omega_f^t} - (p,\nabla\cdot\Phi)_{\Omega_f^t} + 2\mu_f(\epsilon(\mathbf{v}),\nabla\Phi)_{\Omega_f^t} = \frac{\rho_f}{\Delta t}(\mathbf{v}^{(1)},\Phi)_{\Omega_f^t} - (\sigma_f(p,\mathbf{v})\cdot\mathbf{n},\Phi)_{\partial\Omega_f^t} - (\sigma_f(p,\mathbf{v})\cdot\mathbf{n}_f,\Phi)_{\Gamma^t},$$

$$-(\nabla\cdot\mathbf{v},\eta)_{\Omega_f^t} = 0,$$

$$\Delta t(\nabla\mathbf{w},\nabla\Psi)_{\Omega_f^t} = -(\nabla\mathbf{U}^{(1)},\nabla\Psi)_{\Omega_f^t} + ([\nabla\mathbf{U}^{(1)} + \Delta t\nabla\mathbf{w}]\cdot\mathbf{n},\Psi)_{\partial\Omega_f^t} + ([\nabla\mathbf{U}^{(1)} + \Delta t\nabla\mathbf{w}]\cdot\mathbf{n}_f,\Psi)_{\Gamma^t},$$

and in the solid

$$\frac{\rho_s}{\Delta t}(\mathbf{v},\Phi)_{\Omega_s} + \rho_s((\mathbf{v}\cdot\nabla)\mathbf{v}^0,\Phi) + \Delta t(\sigma_s(\mathbf{v}),\nabla(\Phi))_{\Omega_s} = \frac{\rho_s}{\Delta t}(\mathbf{v}^{(1)},\Phi)_{\Omega_s} - (\sigma_s(\mathbf{U}^{(1)}),\nabla\Phi)_{\Omega_s} - ([\sigma_s(\mathbf{U}^{(1)}) + \Delta t\sigma_s(\mathbf{v})]\cdot\mathbf{n},\Phi)_{\partial\Omega_s^t} - ([\sigma_s(\mathbf{U}^{(1)}) + \Delta t\sigma_s(\mathbf{v})]\cdot\mathbf{n}_s,\Phi)_{\Gamma^t},$$

$$\frac{1}{\delta}(\mathbf{v},\Psi)_{\Omega_s} - \frac{1}{\delta}(\mathbf{w},\Psi)_{\Omega_s} = 0.$$

The parameter δ should be small and ensures the importance of $\mathbf{v_s} = \mathbf{w_s}$ inside the solid. On the interface, we have distinguished between the normal vector with respect to the fluid and solid domain. In general $\mathbf{n}_f = -\mathbf{n}_s$. To be able to set up and assemble the matrices for this system, the equations should be added to form one bilinear form $a(\mathbf{v},p,\mathbf{w},\Phi,\eta,\Psi)$ and one linear form $L(\Phi,\eta,\Psi)$.

5.2.3 A discussion on function spaces

We have previously defined the L^2 (def. 4.1) and H^1 (def. 4.2) spaces, as well as the linear continuous Galerkin basis functions (section 4.1.2). In order to have a well posed-problem, we need a triple (Φ,η,Ψ) to satisfy a few given conditions. In the following, a brief justification of the choice of function spaces used in this study are given.

For the incompressible Navier-Stokes equations, much of the mathematical theory

and understanding have been developed by investigation of the simplified Stokes flow where the acceleration term is neglected in the momentum equation, that is:

$$-\mu\nabla^2\mathbf{v} + \nabla p = \mathbf{f}$$

Numerous possible pairs (Φ, η) have been proposed over the years since the first report by Taylor and Hood (1973) [55]. The discretization used by Taylor and Hood consists of quadratic piecewise polynomials for the velocity components and linear piecewise polynomials for the pressure, and is still a very popular choice of basis functions. These types of elements are often referred to as Taylor-Hood elements or simply just P2-P1 elements.

As mentioned earlier, the final step in the finite element method consists of solving a linear system of equations. In the case of Stokes equations with body forces $\mathbf{f}$, a matrix system on the following form needs to be solved

$$\begin{bmatrix} \mathbf{A} & \mathbf{B} \\ \mathbf{B}^T & \mathbf{0} \end{bmatrix} \begin{bmatrix} \mathbf{v} \\ \mathbf{p} \end{bmatrix} = \begin{bmatrix} \mathbf{f} \\ \mathbf{0} \end{bmatrix}$$

Which means that

$$\mathbf{A}\mathbf{v} + \mathbf{B}\mathbf{p} = \mathbf{f} \tag{5.1}$$

$$\mathbf{B}^T\mathbf{v} = \mathbf{0} \tag{5.2}$$

To get an expression for $\mathbf{v}$, we multiply (5.1) with $\mathbf{A}^{-1}$ to obtain

$$\mathbf{v} = \mathbf{A}^{-1}(\mathbf{f} - \mathbf{B}\mathbf{p})$$

And insert this expression into (5.2) to get an equation only involving the pressure

$$\mathbf{B}^T\mathbf{A}^{-1}(\mathbf{f} - \mathbf{B}\mathbf{p}) = \mathbf{0}$$

or

$$\mathbf{B}^T\mathbf{A}^{-1}\mathbf{B}\mathbf{p} = \mathbf{B}^T\mathbf{A}^{-1}\mathbf{f}$$

For the solution to be unique, the matrix $\mathbf{B}^T\mathbf{A}^{-1}\mathbf{B}$ often referred to as the *Schur complement* needs to be non-singular. A necessary and sufficient condition for this is that $\mathrm{Ker}(\mathbf{B}) = \{0\}$, or

$$\sup_{\mathbf{v}_h} \int p_h \nabla \cdot \mathbf{v}_h > 0.$$

For all discrete pressures $p_h \neq 0$. This ensures solvability. For convergence, the famous Babuska-Brezzi (BB), or inf-sup condition needs to be satisfied [56]

$$\inf_{p_h} \sup_{\mathbf{v}_h} \frac{\int_\Omega p_h \nabla \cdot \mathbf{v}_h}{||\mathbf{v}_h||_1 ||p_h||_0} \geq D > 0,$$

where D is a constant independent of the mesh resolution.

Provided this condition is satisfied, the following error estimate holds for Stokes equations

$$||\mathbf{v}_h - \mathbf{v}||_1 + ||p_h - p||_0 < C(h^k||\mathbf{v}||_{k+1} + h^{l+1}||p||_{l+1})$$

Where k and l are the degrees of polynomials used for velocity components and pressure, respectively. To obtain optimal convergence for the solution the polynomial degree should be one higher for the velocity components than for the pressure, that is, $k = l + 1$. For instance, using P3-P1 elements, computer resources are "wasted" by introducing more degrees of freedom (dofs) without improving convergence. Several choices of element type combinations, for instance Linear elements (P1) both for velocity and pressure do not satisfy the BB condition, and as a consequence unphysical oscillations in pressure can be seen.

Elements not satisfying the BB condition can be used if a proper stabilization is introduced. Due to the drastic reduction of dofs, P1-P1 elements are often used when large systems are solved for instance in commercial software. This combination is default in COMSOL, while for 3D problems in FLUENT, a slightly different element, the "mini-element" is used as first developed by Fortin (1981) [57]. This element is linear but with an extra degree of freedom known as a bubble in the center.

In this study, P2-P1 elements are used for the material velocity and pressure. However, a function space is also needed for the domain velocity, $\mathbf{w}$. As discussed by Quaini [58], P1-elements for the domain velocity will ensure the transformation of straight lines in the new domain. In the fluid momentum equation, the function $\mathbf{w}$ is only used in the term $((\mathbf{v} - \mathbf{w}) \cdot \nabla)\mathbf{v}^{(0)}$ and since $\mathbf{v}$ is a polynomial of degree 2, $\mathbf{v} - \mathbf{w}$ will also be a polynomial of degree 2. Therefore, we use the combination P2-P1-P1 for velocity, pressure and displacement, respectively.

5.2.4 Treatment of boundary conditions

In addition to the boundary conditions described by Turek and Hron [20], homogenuous Dirichlet conditions are prescribed to the mesh displacement velocity on the domain boundary, i.e

$$\mathbf{w} = 0 \text{ on } \partial\Omega_f^t \cup \partial\Omega_s^t$$

Except for the fluid velocity on the outlet, the domain boundaries (not interface) have prescribed Dirichlet conditions on both $\mathbf{u}$ and $\mathbf{w}$. Therefore the test functions Φ and Ψ will be zero on these boundaries.

If we add all the equations in the previous section together, the contributions to the boundary integral on the interface gives:

$$-(\sigma_f(p, \mathbf{v}) \cdot \mathbf{n}_f, \Phi)_{\Gamma^t} - ([\sigma_s(\mathbf{U}^{(1)}) + \Delta t \sigma_s(\mathbf{w})] \cdot \mathbf{n}_s, \Phi)_{\Gamma^t}$$

By leaving this out of the variational form, we weakly impose

$$\sigma_f(p, \mathbf{v}) \cdot \mathbf{n} = \sigma_s(\mathbf{U}) \cdot \mathbf{n}$$

On the interface. The choice of $\mathbf{n}$ ($\mathbf{n} = \mathbf{n}_f$ or $\mathbf{n} = \mathbf{n}_s$) is arbitrary, but the same for each side of the equation.

Because we use the same function for fluid velocity and solid velocity, the no-slip condition is naturally incorporated for the fluid on the structure

$$\mathbf{v}_f = \mathbf{v}_s \text{ on } \Gamma^t$$

Because the functions $\mathbf{v}_f$ and $\mathbf{v}_s$ share nodes on the interface.

The additional equation for $\mathbf{w}$ in the fluid also gives rise to boundary conditions on $\frac{\partial \mathbf{U}}{\partial n}$ on the interface. To this end we set

$$\frac{\partial \mathbf{U}}{\partial n} = 0$$

and rather let the parameter δ underline the importance of $\mathbf{w} = \mathbf{v}$ *inside* the solid, whereas $\mathbf{w}$ in the fluid should just ensure a smooth mesh displacement.

On the outlet, we assign the stress-free condition $\sigma_f(p, \mathbf{v}) \cdot \mathbf{n} = 0$ so the boundary integral also vanish on the outlet for the momentum equation in the fluid.

This means that all integrals involving boundaries will vanish in the variational form. The Dirichlet conditions are imposed in FEniCS as described in section 4.2.

5.2.5 FSI in FEniCS

There will be some changes and a great leap in complexity compared to the previous example using FEniCS. The main differences and additions are explained here. The code snippets in this section is of course subject to changes and updates in the DOLFIN library. This thesis do not intend to present a full solver with great complexity and many dependencies, but rather outline the most important lines of code and explain difficulties behind the FSI problem in FEniCS. The explanation here is meant such that a reader familiar with FEniCS should be able to implement such a code within a short amount of time.

The computational mesh is constructed in Gmsh with a straight boundary dividing the fluid and the solid. This way, the class MeshFunction can be used to divide the mesh into two subdomains. We now assume we have classes describing the solid and fluid region, implemented simliary to the boundary functions in the Poisson example 4.2.

```
mesh = Mesh('FSI_mesh.xml')
SD = MeshFunction('uint', mesh, mesh.topology().dim())
SD.set_all(0)
Elastic().mark(SD,1)
```

where

```
class Elastic(SubDomain):
        def inside(self,x,on_bnd):
                # returns True if vector x in solid.
```

'uint' means that the MeshFunction has values of nonnegative integers. The last argument ensures the MeshFunction to have the same dimension as the mesh. Using the MeshFunction, the fluid domain has been marked 0, and the solid domain has been marked 1. Integration over the two domains can be separated by passing this number to dx in the variational formulation. A similar class, the FacetFunction

```
boundaries = FacetFunction("size_t",mesh)
```

is used to mark the boundaries and, if needed, separate integration over specific parts of the boundary.

For the FacetFunction, 'size_t' has the same interpretation as 'uint' has for the MeshFunction.

We need function spaces for all three test functions, corresponding to $\mathbf{v}, p$ and $\mathbf{w}$, and in this case we can use a class in FEniCS to create a mixed function space. Test and trial functions should also be created from this mixed space.

```
V = VectorFunctionSpace(mesh,'CG',2)
P = FunctionSpace(mesh,'CG',1)
W = VectorFunctionSpace(mesh,'CG', 1)
VPW = MixedFunctionSpace([V,P,W])
v,p,w = TrialFunctions(VPW)
phi,eta,psi = TestFunctions(VPW)
```

All Dirichlet boundary conditions need to be specified, and the functions need to be in the space of the respective trial function where the condition is set. For instance, the top boundary of the domain has been marked 2 with the FacetFunction, and we want to prescribe the no-slip condition on the fluid velocity.

```
noslip = Constant((0.0,0.0))
bcv2 = DirichletBC(VPW.sub(0),noslip,boundaries,2) # Top
```

All Dirichlet boundary conditions are put together in a list, bcs.

When the MeshFunction and FacetFunction have been properly marked, we need to map the information from these classes to the different measures, dx, ds, and dS representing integration over cells, exterior facets and interior facets, respectively. This is done by:

```
dS = Measure('dS')[boundaries]
dx = Measure('dx')[SD]
ds = Measure('ds')[boundaries]

dx_f = dx(0,subdomain_data=SD)
dx_s = dx(1,subdomain_data=SD)
```

The last two lines simplifies the integrands in the variational form and make it more clear which expressions have to be used in the fluid domain, and which should be used in the solid domain.
It can be convinient to define the constants used in FEniCS as instances of the class Constant, to avoid re-compiling if the value of the constant is changed:

```
dt = 0.0003
k = Constant(dt)
```

Initial conditions are needed, and are imposed by setting

```
U = Function(W)
v1 = Function(V)
v0 = Function(V)
```

The initial conditions are simply set to be zero both for velocity and displacement. Before preceding to the variational formulation, note that regular Python functions can be used within UFL. For example:

```
def eps(v):
        return sym(grad(v))

def sigma_s(U):
        return 2*mu_s*eps(U) + lamda*tr(eps(U))*Identity(2)
```

We define the bilinear and linear forms, a and L, for each separate equation, momentum, continuity and the movement of the domain in both the fluid and solid domain (except for continuity in the solid). For instance, aMF will denote the bilinear form a for the momentum equation in the fluid.

```
# FLUID
aMF = rho_f/k*inner(v,phi)*dx_f \
        + rho_f*inner(grad(v0)*(v-w),phi)*dx_f \
        - inner(p,div(phi))*dx_f \
        + 2*mu_f*inner(eps(v),grad(phi))*dx_f

LMF = rho_f/k*inner(v1,phi)*dx_f

aCF = -inner(div(v),eta)*dx_f

aDF = k*inner(grad(w),grad(psi))*dx_f
LDF = -inner(grad(U),grad(psi))*dx_f

aF = aMF + aCF + aDF
LF = LMF + LDF

# SOLID
aMS = rho_s/k*inner(v,phi)*dx_s \
        + rho_s*inner(grad(v0)*v,phi)*dx_s
        + k*inner(sigma_s(v),grad(phi))*dx_s

LMS = rho_s/k*inner(v1,phi)*dx_s \
        - inner(sigma_s(U),grad(phi))*dx_s

aDS = 1/delta*inner(v,w)*dx_s \
        - 1/delta*inner(d,w)*dx_s

aS = aMS + aDS
LS = LMS
```

The forms can now be added to obtain one bilinear and one linear form:

```
a = aS + aF
L = LS + LF
```

Before the time loop starts we define a function to hold the solution:

```
VPW_ = Function(VPW)
```

This function will consist of all values for $\mathbf{v}$, p and $\mathbf{w}$.

The time loop runs until the current time exceeds the specified end time, T. The forms change in time, and thus needs to be assembled to use correct values for $\mathbf{v}^{(1)}, \mathbf{w}^{(1)}, \mathbf{U}^{(1)}$ and $\mathbf{v}^{(0)}$. The linear form needs an update each time step, while the bilinear form needs to be updated every single iteration inside the time loop. For the iterative method, we have chosen the Picard iteration based on the simplicity of the algorithm compared to Newton's method, especially when dealing with a mixed

function space consisting of three separate spaces. Balaban (2012) [59] implemented a Netwon iteration method for FSI, but the code is not compatible with newer versions of DOLFIN. The Picard iteration runs until the L^2 norm of $(\mathbf{v} - \mathbf{v}^{(0)})$ is less than a given tolerace, or if the number of iterations becomes to large.

```
while t < T:
        ...
        b = assemble(L)
        ...
        while error > tau and k_iter < max_iter:
                A = assemble(a)
                A = ident.zeros()
                [bc.apply(A,b) for bc in bcs]
                solve(A,VPW_.vector,b,'lu')
                v_,p_,w_ = VPW_.split(True)
                eps = errornorm(v_,v0,degree_rise=3)
                k_iter += 1

                v0.assign(v_)
```

The second statement within the iteration loop is needed because the lack of an equation for p within the solid. The *ident.zeros()* function replaces zeros with ones on the diagonal of the matrix block, and the solution vector for p will be zero inside the solid. In FEniCS, a Function has to be defined over the whole mesh, and adjusting the linear system as described is a way to overcome this issue in the present version of DOLFIN (1.6.0). To assign a new value for v0, and later be able to calculate drag and lift, we split the solution vector with the argument True. The chosen solver is the direct "lu" solver. Iterative solvers are in general faster, but in this case no Krylov Solver was found to converge.

The next step is to address how the mesh should be updated. The domain should now move with velocity $\mathbf{w}$, so the mesh moves $\Delta t\mathbf{w}$ from one time step to the next. For the total displacement, the update $\mathbf{U} = U^{(1)} + \Delta t\mathbf{w}$ should also be taken into account. In FEniCS, the actual update of the mesh is done with the functions *ALE.move()* and *bounding_box_tree().build()*

```
        w_vector()[:] *= float(k)
        U_.vector()[:] += w_vector()[:]
        ALE.move(mesh,w_)
        mesh.bounding_box_tree().build(mesh)

        v1.assign(v_)
```

The final line updates the velocity in order to proceed to the next time step. Note that the velocity in both the fluid and the solid is updated by this call.

5.3 Benchmark Results

5.3.1 CFD tests

For the CFD tests we perform tests treating the flag as a rigid object. This can be done by changing the structural parameters, or simply by adjust the mesh to include the fluid domain only. In this validation we choose the latter. We show convergence with Mesh, where mesh 0 is the coarsest version. The **Ref.** are the reference values as given in the original benchmark paper.

Parameter	CFD1	CFD2	CFD3
$\rho_f\,[10^3\frac{\mathrm{kg}}{\mathrm{m}^3}]$	1	1	1
$\nu_f\,[10^{-3}\frac{\mathrm{m}^2}{\mathrm{s}}]$	1	1	1
$\bar{v_0}$	0.2	1	2
$\mathrm{Re} = \frac{Ud}{\nu_f}$	20	100	200

Table 5.1: Parameters for the CFD test cases

cells	dofs	Drag	Lift
1334	6443	13.9344	1.0980
5336	24892	14.1165	1.0836
21344	97808	14.1865	1.0944
Ref.		**14.29**	**1.119**

Table 5.2: Results for CFD1

cells	dofs	Drag	Lift
1334	6443	130.092948352	10.9117261826
5336	24892	134.43022177	10.473965217
21344	97808	135.777285175	10.7118857057
Ref.		**136.7**	**10.53**

Table 5.3: Results for CFD2

5.3.2 CSM tests

The structural tests are performed by adding the gravitational force to the structural part only. The CSM3 test is computed as a time-dependent case, starting from the initial position while CSM1 and CSM2 are Steady State (SS) solutions. For CSM3, the total energy is not conserved as the Backward Euler scheme used to discretize in time slightly reduces the amplitude for oscillating solutions. For this reason,

cells	dofs	Drag	Lift
1334	6443	391.305 ± 2.039	-28.536 ± 200.149
5336	24892	428.769 ± 5.735	-18.001 ± 429.410
21344	97808	437.211 ± 5.802	-16.204 ± 422.331
cells	dofs	Drag	Lift
755	6443	391.401 ± 2.460	-22.652 ± 232.090
5336	24892	428.787 ± 5.773	-14.575 ± 441.152
21344	97808	438.013 ± 5.822	-14.819 ± 425.841
Ref.		**439.45 ± 5.6183**	**-11.893 ± 437.81**

Table 5.4: Results for CFD3 for $\Delta t = 0.0005$ *and* $\Delta t = 0.0001$

a third parameter of interest is included in the results, namely the reduction of amplitude from one cycle to the next. From the reference results it appears that the flag bounces above the initial position in steady state, meaning that some energy must have been added due to their choice of scheme. This is also clear when closely examining the attached plots. This was not further discussed, and no time-dependent amplitude was reported. The temporal discretization in the original benchmark proposal was done by the Cranck-Nicholson scheme, which in general have better conservation properties than the Backward-Euler scheme but is known to be less stable [20]. Again, it should be noted that we did not used the same constitutive model for the elastic material, so some differences would be expected in cases with large displacements.

Parameter	CSM1	CSM2	CSM3
$\rho_s \, [10^3 \frac{\text{kg}}{\text{m}^3}]$	1	1	1
ν_s	0.4	0.4	0.4
$\mu_s \, [10^6 \frac{\text{m}^2}{\text{s}}]$	0.5	2	0.5
$g \, [\frac{\text{m}^2}{s}]$	2	2	2

Table 5.5: Parameters for the CSM test cases

cells	dofs	U_x of A $[10^{-3}]$	U_y of A $[10^{-3}]$
738	4596	-12.410569	-60.599246
2952	17305	-12.419505	-60.622920
11808	67077	-12.422290	-60.630433
Ref.		**-7.187**	**-66.10**

Table 5.6: Results for CSM1

cells	dofs	U_x of A $[10^{-3}]$	U_y of A $[10^{-3}]$
738	4596	-0.92479395	-16.853778
2952	17305	-0.92558954	-16.861757
11808	67077	-0.92583356	-16.864252
Ref.		**-0.4690**	**-16.97**

Table 5.7: Results for CSM2

cells	dofs	U_x of A $[10^{-3}]$	U_y of A $[10^{-3}]$	Amp reduction y (%)
738	4596	-44.175 ± 44.007	-72.712 ± 65.281	5.4
2952	17305	-44.176 ± 44.001	-72.720 ± 65.281	5.4
11808	67077	-44.177 ± 44.001	-72.720 ± 65.281	5.4
Ref.		**-14.305 ± 14.305**	**-63.607 ± 65.160**	

cells	dofs	U_x of A $[10^{-3}]$	U_y of A $[10^{-3}]$	Amp reduction y (%)
738	4596	-44.631 ± 44.628	-69.702 ± 69.290	0.3
2952	17305	-44.633 ± 44.629	-69.701 ± 69.289	0.3
11808	67077	-44.094 ± 44.091	-69.703 ± 69.289	0.3
Ref.		**-14.305 ± 14.305**	**-63.607 ± 65.160**	

Table 5.8: Results for CSM3, $\Delta t = 0.01, 0.001$

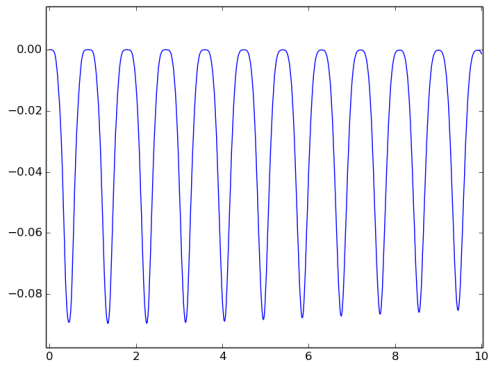

(a) displacement x vs time

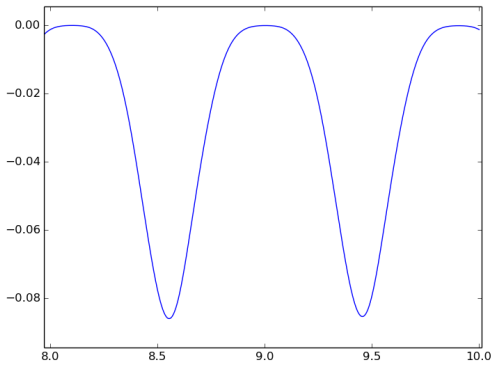

(b) displacement x vs time

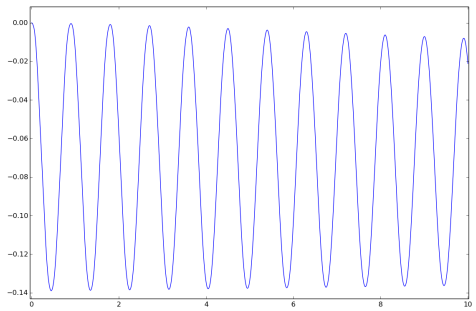

(c) displacement y vs time

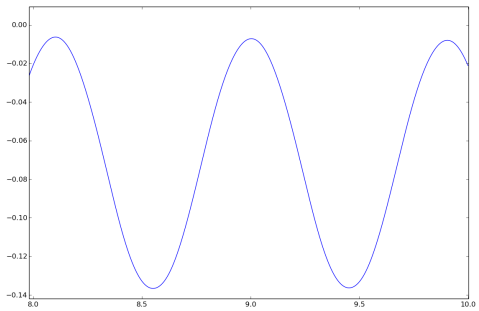

(d) displacement y vs time

Figure 5.2: Displacements for the CSM3 test case. $\Delta t = 0.001$

5.3.3 FSI tests

Parameter	FS1	FSI2	FSI3
$\rho_f \, [10^3 \frac{\text{kg}}{\text{m}^3}]$	1	1	1
$\nu_f \, [10^{-3} \frac{\text{m}^2}{\text{s}}]$	1	1	1
$\bar{v}_0$	0.2	1	2
$\text{Re} = \frac{Ud}{\nu_f}$	20	100	200

Parameter	FSI1	FSI2	FSI3
$\rho_s \, [10^3 \frac{\text{kg}}{\text{m}^3}]$	1	10	1
ν_s	0.4	0.4	0.4
$\mu_s \, [10^6 \frac{\text{m}^2}{\text{s}}]$	0.5	0.5	2

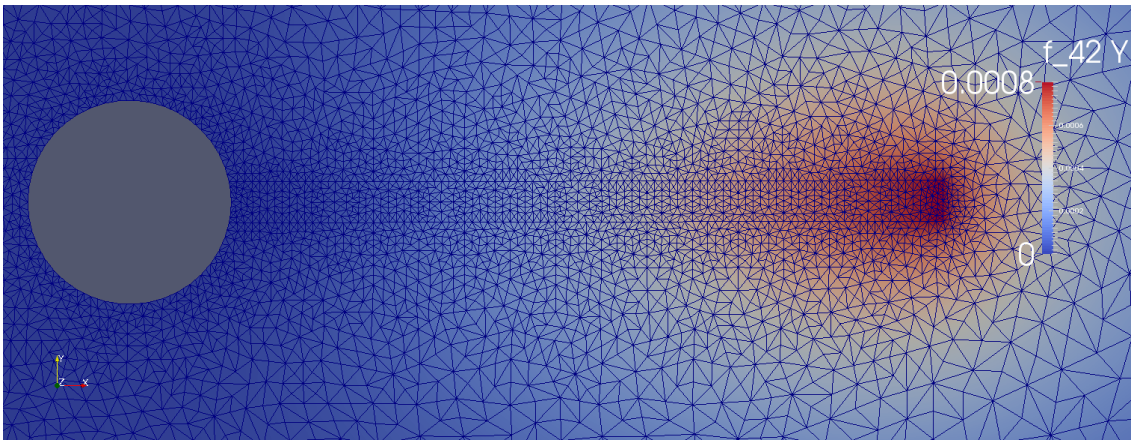

Figure 5.3: Steady state displacement in y-direction for the FSI1 test case for the medium refinement version of the mesh. The mesh around the structural part also has been slightly adjusted

cells	dofs	U_x of A $[10^{-3}]$	U_y of A $[10^{-3}]$	Drag	Lift
2698	15329	0.015596	0.74221	14.0876279441	0.756130219216
10792	60336	0.017738	0.77686	14.1777783843	0.763145083966
43168	239384	0.019824	0.79558	14.1869409712	0.758109277348
Ref.		**0.0227**	**0.8209**	**14.295**	**0.7638**

Table 5.9: Results for FSI1

cells	dofs	U_x of A $[10^{-3}]$	U_y of A $[10^{-3}]$	Drag	Lift
2698	15329	-4.33 ± 4.54	1.40 ± 29.96	441.45 ± 33.15	-2.30 ± 178.00
10792	60336	-4.84 ± 4.62	1.27 ± 31.74	469.11 ± 44.50	0.92 ± 97.27
Ref.		**-2.69 ± 2.53**	**1.48 ± 34.38**	**457.3 ± 22.66**	**2.22 ± 149.78**

Table 5.10: Results for FSI3, $\Delta t = 0.0003$

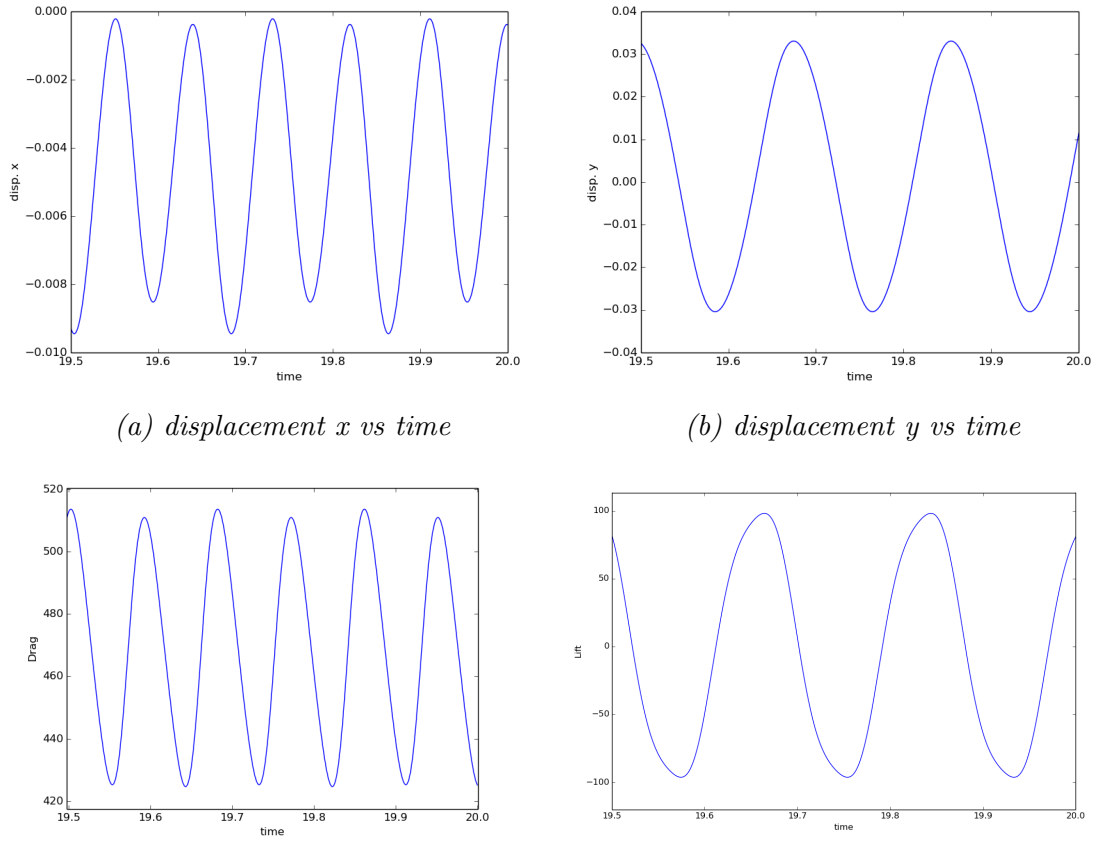

(a) displacement x vs time

(b) displacement y vs time

(c) Drag vs time

(d) Lift vs time

Figure 5.4: Plots from the FSI3 test case. $\Delta t = 0.0003$

5.3.4 Comments

The FSI 2 test case includes displacements ≈ 2.5 times greater than the flag height. The linear elasticity model was not applicable to these magnitudes. In addition, further mesh refinement of the FSI 3 case was not possible due to problems with mesh updates. Rapid changes and great magnitudes in displacement caused some cells to overlap to other, causing instabilities. Whether this is due to how the function mesh.move() works, or a result of the discrete equations itself remains unclear. However, results in this chapter indicates that our models performs qualitatively well when the mesh acts as expected. However, the relative displacements in these tests are many orders of magnitude higher than in the spinal cord.

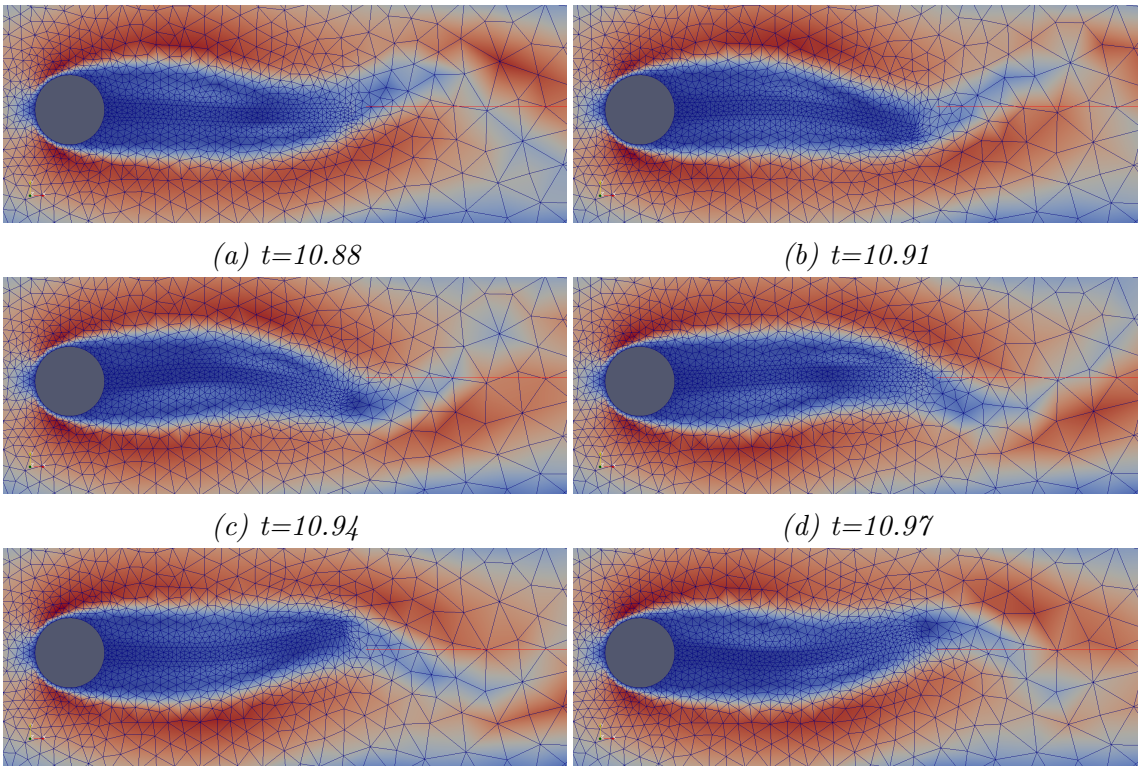

(a) t=10.88 *(b) t=10.91*

(c) t=10.94 *(d) t=10.97*

(e) t=11.00 *(f) t=11.03*

Figure 5.5: The colormap shows the magnitude of the velocity around the flag at six different states of time in fully developed flow on the coarsest mesh. Maximum velocity reaches 4.37. The mesh consists of a smooth curve at the interface, and the domains are separated beforehand in FEniCS

Chapter 6

Numerical Methods for the Biot Problem

As seen in chapter 3, the Biot problem is similar to linear elasticity, but from the modeling point of view, some problems arise. We have previously taken advantage of the continuous Galerkin elements in the sense that the fluid velocity is continuous with the structural velocity. The boundary condition

$$\mathbf{v}_f = \mathbf{v}_s + \mathbf{q} \text{ on } \Gamma, \tag{6.1}$$

will not allow us to have one continuous function describing fluid velocity $\mathbf{v}_f$, in the fluid domain and skeleton velocity $\mathbf{v}_s$, in the poroelastic medium. The right hand side of the boundary condition describes the total (macroscopic) velocity in the poroelastic medium. Therefore, if continuous Galerkin elements are used we automatically end up with $\mathbf{v}_f = \mathbf{v}_s$ on the interface, implying $\mathbf{q} = 0$ and no flux over the surface. In the following we show a workaround for this problem, and it should now be stressed that the notation have to change in a way to implement the problem in FEniCS. We now use the following:

$\mathbf{v}$ – fluid velocity in the fluid domain. Total velocity (darcy flux + skeleton velocity) in the poroelastic domain.

$\mathbf{w}$ – domain (or mesh) velocity in the fluid domain. Skeleton velocity in the poroelastic domain.

p – fluid pressure in the fluid domain. Pore pressure in the poroelastic domain.

$\mathbf{U}$ – domain (or mesh) displacement in the fluid domain. Skeleton displacement in the poroelastic domain.

6.1 Previous work

Within biomechanics poroelasticity is a subject of interest as fluid frequently flow through tissue in the human body. The spinal cord has been modeled as a poroelastic structure by Støverud (2015) [18], without coupling to the surrounding SAS. Coupling between poroelastic and viscous equations have been done to model flow through the brain, e.g. by Tully and Ventikos (2009) [60] and Vardakis et al. (2016) [61]. The two latter have used iterative methods both to couple pressure and velocity in the fluid domain as well as a partitioned approach regarding the coupling between viscous and poroelastic equations. However, in hemodynamics fluid and structure densities are of the same order making these equations hard to couple [62]. We aim to have the whole system coupled, making the problem easier with respect to stability, however the computational time needed is greatly increased.

6.2 Weak form of the equations

The weak form is obtained in a similar way as for the FSI problem. The notation has changed slightly and the equations in the poroelastic domain are slightly different. By omiting the inertia term $\frac{\mathrm{d}\mathbf{q}}{\mathrm{d}t}$, the momentum equation (3.13) for the fluid phase can be written

$$\mathbf{q} = -K\nabla p - \rho_p \frac{\mathrm{d}w}{\mathrm{d}t},$$

and inserting this into equation (6.1), now using $\mathbf{w}$ as the skeleton velocity gives

$$\mathbf{v} = \mathbf{w} - K\nabla p - \rho_p \frac{\mathrm{d}w}{\mathrm{d}t}.$$

As before let the domain Ω^t be split into the deformable fluid domain Ω_f^t and the deformable solid domain Ω_s^t. The exterior boundaries are denoted $\partial\Omega_f^t$ and $\partial\Omega_s^t$, and the interface is named Γ^t. In the fluid, the weak form reads

$$\begin{aligned}\frac{\rho_f}{\Delta t}(\mathbf{v},\Phi)_{\Omega_f} + \rho_f(((\mathbf{v}-\mathbf{w})\cdot\nabla)\mathbf{v}^{(0)},\Phi)_{\Omega_f^t} - (p,\nabla\cdot\Phi)_{\Omega_f^t} + 2\mu_f(\epsilon(\mathbf{v}),\nabla\Phi)_{\Omega_f^t} = \\ \frac{\rho_f}{\Delta t}(\mathbf{v}^{(1)},\Phi)_{\Omega_f^t} - (\sigma_f(p,\mathbf{v})\cdot\mathbf{n},\Phi)_{\partial\Omega_f^t} - (\sigma_f(p,\mathbf{v})\cdot\mathbf{n}_f,\Phi)_{\Gamma^t},\end{aligned}$$

$$-(\nabla\cdot\mathbf{v},\eta)_{\Omega_f^t} = 0,$$

$$\begin{aligned}\Delta t(\nabla\mathbf{w},\nabla\Psi)_{\Omega_f^t} = -(\nabla\mathbf{U}^{(1)},\nabla\Psi)_{\Omega_f^t} + ([\nabla\mathbf{U}^{(1)} + \Delta t\nabla\mathbf{w}]\cdot\mathbf{n},\Psi)_{\partial\Omega_f^t}, \\ + ([\nabla\mathbf{U}^{(1)} + \Delta t\nabla\mathbf{w}]\cdot\mathbf{n}_f,\Psi)_{\Gamma^t},\end{aligned}$$

and in the poroelastic medium we have

$$\frac{\rho_s}{\Delta t}(\mathbf{w},\Phi)_{\Omega_s^t}+\rho_s((\mathbf{w}\cdot\nabla)\mathbf{w}^0,\Phi)_{\Omega_s^t}-(p,\nabla\cdot\Psi)_{\Omega_s^t}+\Delta t(\sigma_s(\mathbf{w}),\nabla(\Phi))_{\Omega_s}=\frac{\rho_s}{\Delta t}(\mathbf{w}^{(1)},\Phi)_{\Omega_s}$$

$$-(\sigma_s(\mathbf{U}^{(1)}),\nabla\Phi)_{\Omega_s}-([\sigma_s(\mathbf{U}^{(1)})+\Delta t\sigma_s(\mathbf{w})]\cdot\mathbf{n},\Phi)_{\partial\Omega_s^t}$$

$$-([\sigma_s(\mathbf{U}^{(1)})+\Delta t\sigma_s(\mathbf{w})]\cdot\mathbf{n}_s,\Phi)_{\Gamma^t},$$

$$\frac{1}{\delta}(\mathbf{v},\Psi)_{\Omega_s^t}-\frac{1}{\delta}(\mathbf{w},\Psi)_{\Omega_s^t}+\frac{K}{\delta}(\nabla p,\psi)_{\Omega_s^t}+\rho_f\frac{K}{\delta\,\Delta t}(\mathbf{w},\Psi)_{\Omega_s^t}=\rho_f\frac{K}{\delta\,\Delta t}(\mathbf{w}^0,\Psi)_{\Omega_s^t},$$

$$-(\nabla\cdot\mathbf{v},\eta)_{\Omega_s^t}=0.$$

It should be noted that in order to have a well posed problem, we would have to use P2-P1-P2 elements for $\mathbf{v}$, p and $\mathbf{w}$ because $\mathbf{w}$ is now basically the solution to a Navier-Stokes equation. (ref. discussion in section 5.2.3)

Chapter 7

Material parameters

The governing equations describing fluid flow, linear elasticity and poroelasticity requires material parameters describing properties of the fluid and the solid material. The dura mater (outside fluid walls) are assumed rigid. In the following, a justification of the material parameters used in our models is given. While some material parameters are relatively easy to determine, other are reported to differ with several orders of magnitude. At this point, some choices regarding material parameters have to be made, and in the following we explain these coices.

We have used a simple geometry, consisting of two rectangular channels on each side of the rectangular spinal cord. A comparison of model and real MRI-images are given in the next chapter under figure 8.2. Branching nerves from the spinal cord were neglected to simplify the problem from the modeling point of view. This last simplification has been done in similar studies within CFD and FSI, both computational and experimental, using idealized and patient-specific models. [6, 7, 8, 9, 12, 13, 14, 15, 63]

In the simulations the units millimeters and grams are used. This combination gives back the SI-unit $\frac{N}{m^2} = \frac{kg\,m}{s^2 m^2} = \frac{g}{s^2\,mm} = Pa$ for pressure, and is also convenient when considering the scale of the spinal cord. CSF consists of 99% water [64], and thus CSF is modeled as water at 37^oC, i.e $\rho_f = 10^{-3}\frac{g}{mm^3}$ and $\nu_f = 0.658\frac{mm^2}{s}$.

For the spinal cord, studies have shown a huge variety in material parameters. One of the most measured properties in the mammalian central nervous system is probably the Young's modulus, E according to Smith, Humphrey [65]. In addition to this, values for Poisson's ratio, ν_P needs to be found. In the literature, there is a huge gap in reported Young's modulus for spinal cord tissue. These values lie in the range 0.0119-1.198MPa. Most of these studies do not distinguish between grey and white matter in the spinal cord, and neither will we. In general, grey and white matter will have different elastic and porous properties, however, as shown by Støverud et al (2015) [18], the distinction between the two as well as the inclusion of the median fissure as shown in figure 2.1, have shown to have negligible effect except for in small local regions depending on the anatomy of each patient. Developing patient-specific models are highly relevant for a precise description of the CSF flow,

but is not the main goal for this thesis. In the same study, inclusion of a stiffer pia surrounding the spinal cord tissue was also investigated and was shown to affect the pressure distribution within the cord in poroelastic models. In this thesis, we will test different values of Young's modulus for the Spinal cord, but similar to models by Bertram et al. [13, 14, 15], and Martin et al. [12], the pia itself is not included.

Article	Region	Model	Parameters
Hung et al. [66]	spinal cord	Experimental	E = 0.26 MPa
Ben-Hatira et al. [67]	spinal cord	Nonlinear elastic	E = 1.4 MPa ν = 0.499
Ozawa et al. [68]	spinal cord	Experimental	E = 16 kPa
Smith and Humphrey [65]	brain	Experimental	E = 5.0 kPa ν = 0.479
Cheng et al. [69]	spinal cord	Review	E = 0.0119-1.98 MPa
Clarke [70]	spinal cord	Review	E = 0.012-1.37 MPa
Persson et al. [71]	spinal cord	Review (linear elastic)	E = 0.26-1.3MPa

Table 7.1: Summary of elastic parameters used in literature (as presented in Kylstad [17])

From this, Lame's parameters for the spinal cord were determined as

$$\mu_s = \frac{E}{2(1+\nu_P)}$$

and

$$\lambda_s = \frac{\nu_P E}{(1+\nu_P)(1-2\nu_P)}$$

The spinal cord has fibers oriented in the axial direction and a direction-dependent Young's modulus would then be expected. In the literature values range between 0.012 to 1.98 MPa. As reported by Clarke (2010) [70], most spinal cord experimental studies use a tensile test, and the stress-strain and stress-relaxation responses of the spinal cord are nonlinear. Therefore, it will in general be hard to compare results from different studies using different arbitrary levels of strain. Another approach used by Kwon (2002) [72], focuses more on spinal cord injuries and are thus more interested in properties during compression at greater stress. Studies focusing on spinal cord injury due to impact needs stress to be several orders of magnitude higher than for stress occurring during the cardiac cycle. The linear slope of stress as a function of strain is what determines the value of Young's modulus to be used. This slope is probably very different in the regions of stress during the cardiac cycle compared to the regions capable of inflicting injury to the cord, and might explain some of the differences in reported values. Better constitutive models could be attained by combining results from several of these studies. Also, studies by Zarzur

(1996) [73] and Patin et al. (1993) [74] have shown that the cord is substantially stronger transversally than axially. In this work, however, we limit Young's modulus to be a constant independent of spatial direction. For the spinal cord, this assumption has been made in most previous cited works in this thesis. Ozawa et al. (2004) [68] measured the spinal cord with and without an intact pia mater. Without the pia, Young's modulus were measured as 5 kPa and the value reported in table 7.1 is with an intact pia. This value is of interest as there might not be a stiff protecting membrane surrounding the syrinx, and thus the fluid inside the syrinx interacts with a structure with this property. We also use the value used by Bertram (2009) [15] without time dependence, which leaves us with three values of Young's modulus to test for E = 5 kPa, E = 16 kPa and E = 62.5 kPa.

As for the density of the spinal cord, no value were found in the literature. For human bone however, density values from literature were reported between 1500 and 2010 kg/m^3, with an average of 1750 kg/m^3 [75]. In general, spinal cord densities should differ between elastic and poroelastic models because the spinal cord consists of fluid filled pores. When using an elastic model, spinal cord density should simply be the weight per volume of the saturated cord. Poroelasticity, on the other hand is requires the density of the spinal cord tissue itself to be determined. Assuming the fluid filled pores to occupy 20 % of the cord, (porosity, $\phi = 0.2$) based on Nicholson (2001) [76], yields little difference between the two approaches. Therefore a denisty of

$$\rho_s = 1.75\rho_f, \tag{7.1}$$

have been used for both models. In Watsons textbook on the spinal cord [77] the weight of the cord was given as 35g. A different study by Ko (2004) [78] measured spinal cord segment volumes, but were not interested in the total volume of the cord. A rough estimate of the added volumes of all segments gave a total spinal cord volume of 16-17 cm^3 yielding a density of just above 2000 kg/m^3 which means that the assumption (7.1) is probably not too far away.

The permeability, κ is used as a measurement for the how fluid flows in a porous medium. A large permeability indicates a pervious medium. We use the value

$$\kappa = 1.4 \cdot 10^{-15} m^2$$

which has been used in previous studies. [38, 79]

Chapter 8

Simulating CSF Flow and Spinal Cord Motion

8.1 Overview of previous studies

Some studies have investigated the effects of FSI on the spinal cord movement and CSF pressure in geometries without a syrinx. Clark (2013) [9] assumed the Young's modulus to be 1 MPa for the spinal cord, and in their initial tests this choice caused only small displacements. Therefore the conclusion was that FSI had a negligible effect on CSF pressure in the SAS.
Cheng et al. (2014) [10] investigated FSI effects on a patient-specific 3D-geometry. In their model they assumed a Young's modulus of 0.7 MPa, and reached the same conclusion as Clark. As highlighted: *This study informs that fluid structure interaction has no effect on CSF pressure"*.
Clearly, a too high elastic modulus will undermine the effects of FSI, if they do exist. Considering the wide range of material parameters reported in the literature for the spinal cord, we believe further investigation is necessary to be able to make such a statement. In addition, these two studies do not seem to investigate syringomyelia as a primary target, and therefore important effects of FSI could have been overlooked in these specific cases. It has correctly been argued that the pressures involved in these studies ($< 100Pa$) are almost negligible in magnitude compared to even the lowest estimates of the elastic modulus of the Spinal cord ($> 5kPa$). This should cause only very small displacements, and this also seem to be the case for healthy subjects. However, when the syrinx is large, there is only a thin membrane of spinal cord tissue separating the SAS and the fluid in the syrinx allowing larger cord movements.

In porous models presented by Drøsdal, [38] fluid pressure within the cord was altered by the presence of a syrinx but the CSF pressure in the SAS was not. Velocities up to only 3e-7 cm/s inside the syrinx were reported, and therefore there must be some other effects causing the more rapid fluid movement inside the syrinx.

To our knowledge, the most noted groups working on mechanical explanations of

syringomyelia using FSI, include the groups of Chris D. Bertram at the University of Sydney and Bryn Martin at the University of Idaho. Bertram's work include research on pressure waves propagating in the spinal cord in the presence of a syrinx [13, 14, 15, 16]. Even though in this series of papers the main focus is on the overlap between the cervical and thoracic segments of the spinal cord, the mechanisms of interest remains the same. Reflections back and forth are also discussed, which in our opinion only could be related to amplitudes associated with coughing. Bryn Martin has made several in vitro models of the CSF-cord system [11, 12, 80, 81] and shown altered pressure environments due to the presence of a syrinx and obstructions in the SAS.

Even with today's high quality magnetic resonance imaging, (MRI) or phase contrast MRI (PC-MRI), exact velocities are hard to measure. Healthy subjects also have more complex CSF flow and thus difficult to observe or quantify. Since the Chiari I malformation is associated with abnormal CSF flow, a realistic model simulating the pre-operative case needs abnormal inflow or pressure boundary conditions. The latter is extremely hard to measure exact. To this end, it would be beneficial to quantitatively be able to describe the pressure environment in the cord as a possible source of applying correct boundary conditions.

8.1.1 Pressure measurements in patients with Chiari I

Williams (1981) [82] and Häck (2001) [83] investigated the pressure gradient between the intracranial and spinal (lumbar) CSF compartments. In their work the pulsatile pressure were not analyzed, which seem to be more reliable in predicting intracranial compliance according to more recent studies by Eide [84, 85, 86, 87]. Frič and Eide (2015) [88] also measured the pulsatile pressure gradient between the two compartments and have found significantly higher (mean wave amplitude, MWA) gradients in patients with evidence of syringomyelia (12/26 patients) than in those without. (3.7 ± 2.0 mmHg vs 2.1 ± 1.3 mmHg; $p = 0.02$). See figure 8.1 for a graphical representation.

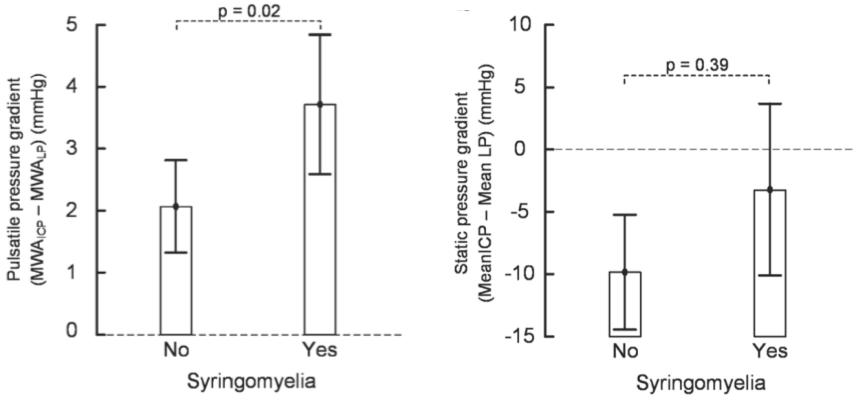

Figure 8.1: Pulsatile (left) and static (right) pressure gradient in patients as used in the study by Frič and Eide [88]

Frič and Eide (2015) [88] also reported that pulsatile intracranial pressure (ICP) as well as pulsatile pressure gradients were clearly abnormal or with borderline values in 69 and 71 % of Chiari I patients, respectively. Without any further speculation, it is interesting to note that these numbers are very close to the number of Chiari I patients that develops a syrinx. The median pressure difference in patients with abnormal pressure gradient were 2.6 mm Hg between the intracranial CSF pressure and the lumbar (LP) CSF pressure. The actual mean static ICP was measured to a median of 7.1 mmHg for the patients (range -0.7 – 13.0), whereas the median of the mean lumbar pressure LP in the patients were 15.1 mm Hg. Czosnyka and Pickard [89] reported ICP for healthy adult subjects to be $7-15$ mm Hg. Williams [90] measured pressure up to 70 mm Hg and 97 mmHg in the SAS in the cisternal (just below the cerebellum) and lumbar region, respectively during coughing. Sansur et al. [91] measured the SAS pressure at the L5-level and found pressures up to 125 mm Hg in patients coughing. The baseline pressures for healthy subjects were reported to be 8.6 – 13.4 mm Hg.

These studies have provided useful information in determining abnormal pressure environment related to the Chiari as well as the possible importance of coughing on the pathogenesis of syringomyelia. Whether or not these pressure measurements can be used in computer models are discussed in the following.

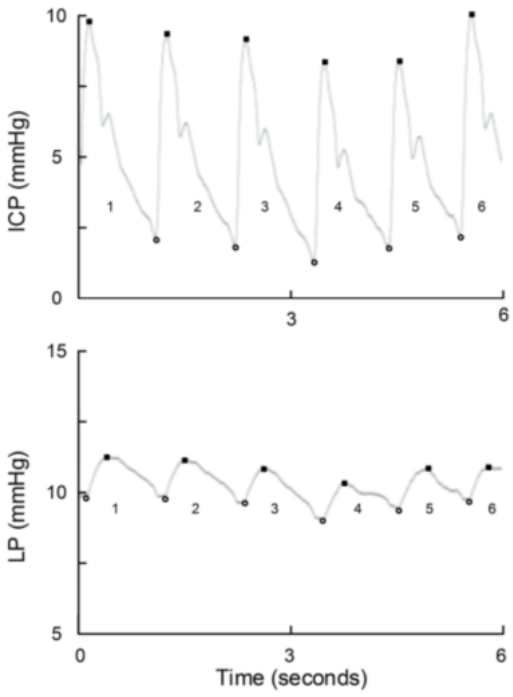

Figure 8.2: Intracranial (ICP) and lumbar (LP) pressure measured simultaneuously by Frič and Eide

8.1.2 Applicability of medical measurements

From the modeling point of view, pressure measurements are of high interest in prescribing the correct boundary conditions at the top and bottom of the cord and SAS model. There are some challenges however. From our understanding, the main focus in most of the studies mentioned in the previous section seem to be to measure pressure differences in Chiari patients *compared* to healthy subjects. As shown by all these studies, altered pressure environment, and thus altered CSF dynamics is somehow related to syringomyelia. However, from a CFD point of view, the actual values of the pressure is also of high interest, and in particular the pressure difference between the Intracranial region and the lumbar region for a specific patient. Simultaneous measurements of ICP and LP was measured for the first time by Frič and Eide (2015) [88]. They measured the pressure over night in subjects laying down. The mean LP was found to have a median value 8mmHg higher than the mean ICP. In addition to this, the pressure was always higher at the Lumbar region as depicted in figure 8.2. From a fluid mechanics point of view, this implies flow in the cranial direction at all times since no hydrostatic pressure should be present when laying down. This is in contradiction to results obtained by Bruker et al. (not yet published data, see A), where the net flux seem to be in the caudal direction. The measurements also contraticts the common belief that the net flux should be zero over a cycle, but according to flow measurements could be investigated further. As for now, these pressure measurements can probably be used for prescribing a normalized pressure waveform at the inlet, but to the authors opinion the actual pressure measurements can not to be used as boundary conditions to obtain reliable results. The minimal modifications must be a shift of baseline in either ICP or LP.

8.2 CSF velocities in syringomyelia

Substantial flow within the syrinx have been reported, e.g. by Brugières et al. (2000) [92] where large syrinxes (graded A or AB) had mean peak velocities of 2.93 cm/s, and small syrinxes (graded B or C) had mean peak velocities of 1.5 cm/s. Brucker et al. (A) reported flow up to 3.1 cm/s inside the syrinx in an assessment of CSF velocities and Cord Motion Before and After Chiari 1 Decompression. The weighted spatial average of the syrinx velocity were found to be 2.03 cm/s. Fluid flow within the syrinx is also supported by Pinna et al. (2000) [93], and it was also pointed out that flow direction inside the syrinx did not necessarily parallel with those observed in the SAS, and that these patterns may vary from patient to patient.

We hypothesized that FSI-effects (deformation and pressure wave propagation) was at least partially responsible for the syrinx velocities reported in the literature, and therefore aimed to match SAS velocities as reported by Brucker et al. A, and observe the effect on syrinx velocities. CSF flow was measured with PC-MRI on three different stages: Pre-operative, 2 months post-operative and 10 months post-operative, when the patient had no remaining symptoms. The peak velocity was reported to be 9.4 cm/s in the caudal direction for the pre-operative case. The

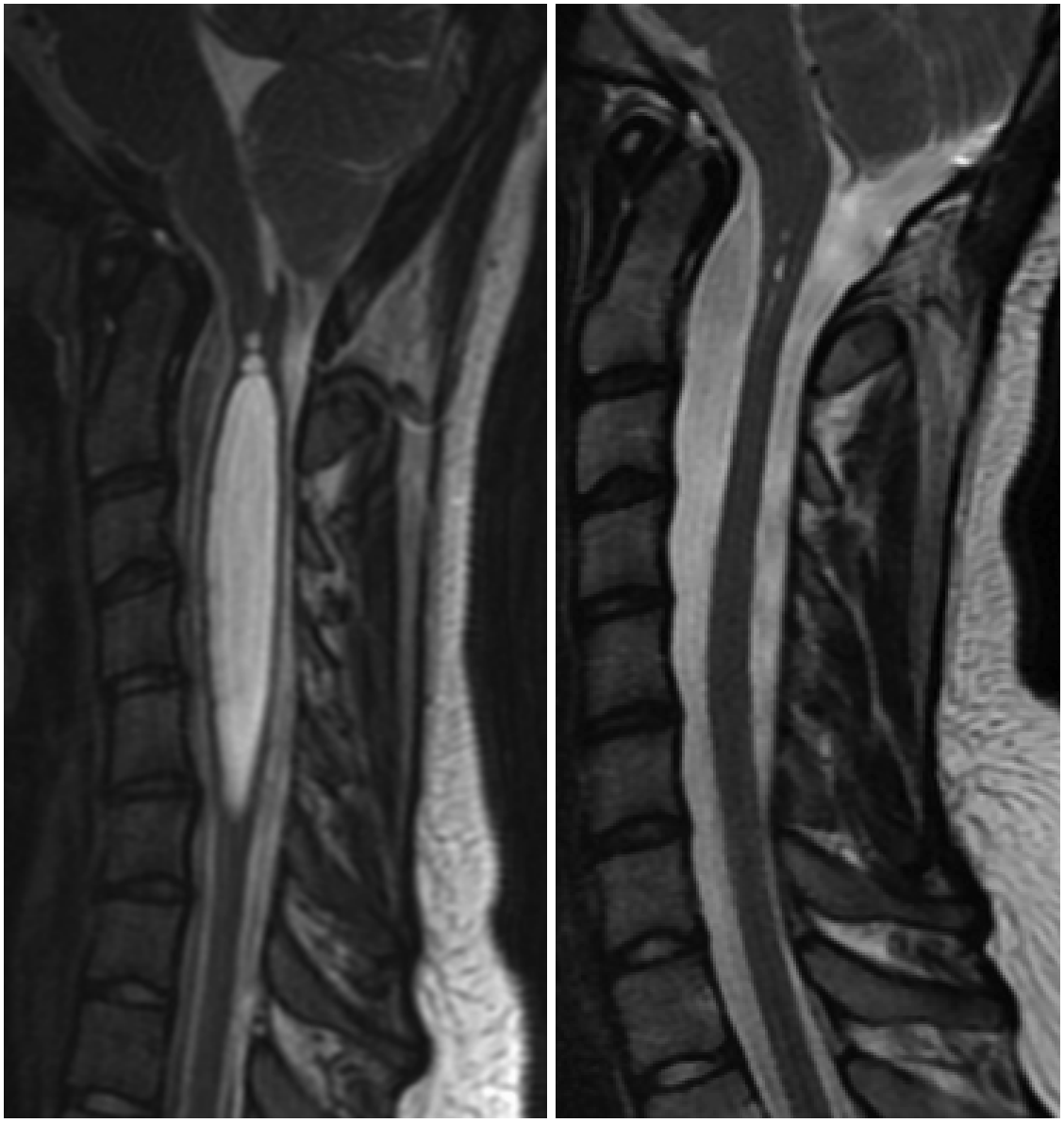

Figure 8.3: MRI image of 14 year old female subject before and 10 months after decompression. Note the withdrawal of the cerebellar tonsils in the post-operative image on the right

velocities varied a lot over a cross-section of the cord, meaning the peak velocity 9.4 cm/s is not representative for the general velocity in the SAS. For the Cross section depicted in figure 8.4 the maximal velocities were registered at the upper left and upper right part of the circle. Along the axis of the cord, velocities in these areas lie around 4-6 cm/s. Figures 8.5 and 8.6 show a comparison between MRI images and the idealized geometries used in this study.

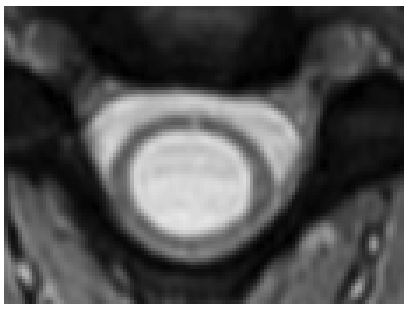

Figure 8.4: Cross-section of the spinal cord. The top of this cross-section is towards the face and the bottom is towards the neck

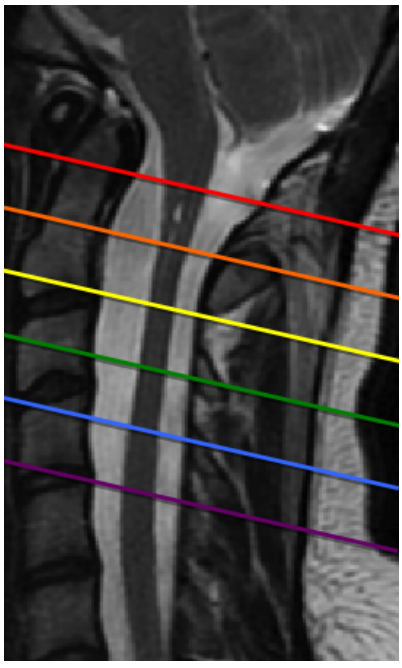

(a) Levels (from top to bottom) C1-C2, C2, C2-C3, C3, C3-C4 and C4-C5 of the spinal cord

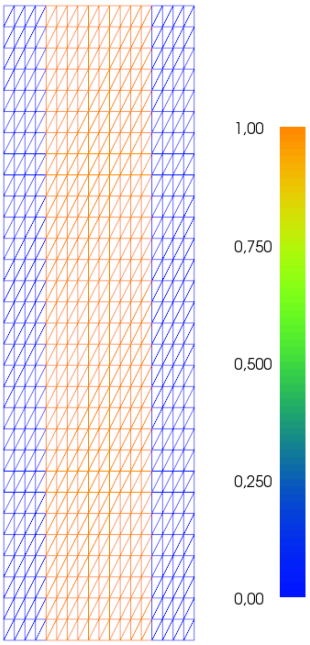

(b) Coarse version of the computational mesh

Figure 8.5: Comparison of the spinal cord and the coarsest version of the computational mesh (healthy subject)

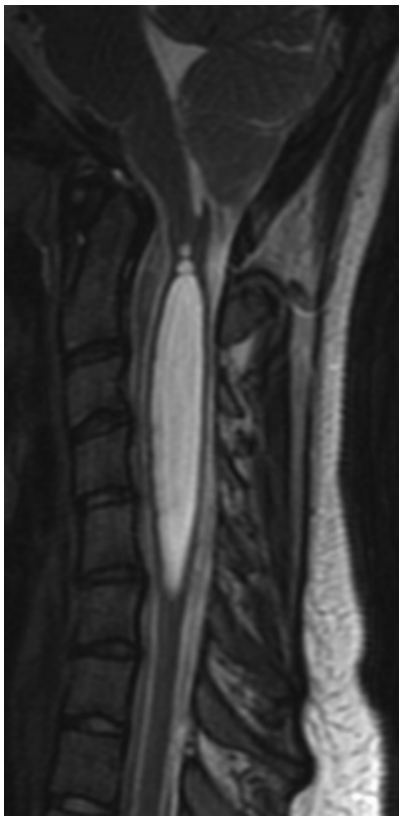

(a) Cord with fluid filled syrinx

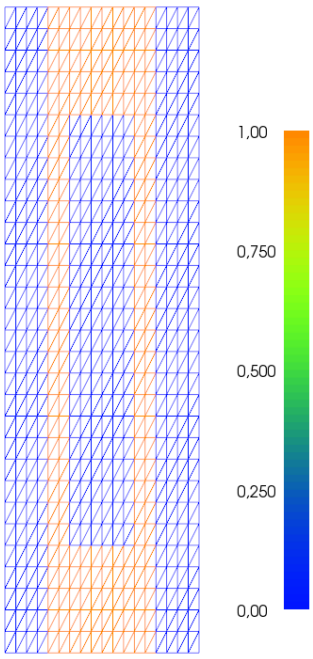

(b) Computational mesh with a fluid filled cavity

Figure 8.6: Comparison of the spinal cord an the coarsest version of the computational mesh (subject with syringomyelia)

8.3 A note on interface conditions

Since we want continuity of stresses on the interface, we use the divergence form (3.6) of the momentum equation, to obtain these when integrating by parts. For the outflow and inflow boundaries for the fluid the pseudo traction condition are the condition of interest. The unknown shear term $\mathbf{n} \cdot (\nabla \mathbf{v}^T)$ should then be added to the bilinear form in the variational formulation. With the pseudo traction condition we have:

$$\begin{aligned} \sigma \cdot \mathbf{n} = -p\mathbf{n} + \mu(\nabla \mathbf{v} + (\nabla \mathbf{v})^T) \cdot \mathbf{n} &= \big[-p\mathbf{n} + \mu \mathbf{n} \cdot \nabla \mathbf{v} \big] + \mathbf{n} \cdot (\nabla \mathbf{v}^T) \\ &= \big[-p\mathbf{n} + \mu \frac{\partial \mathbf{v}}{\partial n} \big] \quad + \mathbf{n} \cdot (\nabla \mathbf{v}^T) \\ &= \quad -p_0 \mathbf{n} \quad + \mathbf{n} \cdot (\nabla \mathbf{v}^T). \end{aligned} \tag{8.1}$$

It should be noted that the *grad* function in FEniCS is in fact given such that grad(v) $= (\nabla \mathbf{v})^T$, and the extra term in (8.1) can be written

```
grad(v).T*n
```

in FEniCS. So far we have only dealt with symmetric operations regarding the *grad* function and therefore this distinction did not have to be made before this point. Similarly, the term

$$\frac{\partial \mathbf{U}}{\partial n}$$

can in fact be included in the variational form by subtracting the term

```
k*inner(grad(w('-'))*n('-'),psi('-'))*dS(5)
```

to the domain bilinear form aDF in section 5.2.5. And adding the term

```
inner(grad(U('-'))*n('-'),psi('-'))*dS(5)
```

to the linear form LDF in the same set of equations. The interface have been given the value 5 and ('-') is used to distinguish variables in the fluid domain from the solid domain. This should give no restriction on **U** except that it will be continuous over the interface. In initial tests, the inclusion of these terms gave no visible effect on displacements, velocities or pressure. These terms were not included in the validation of the solver, but this is something that will not be further investigated at the present time, and we keep these terms in the following simulations.
Other than that, no slip conditions have been imposed at both ends of the spinal cord as well as the outer fluid walls for velocity and displacements. The no slip condition for displacement is also imposed on fluid inlets and outlets. All results presented up to section 8.7 are results obtained with an elastic description of the spinal cord.

8.4 Results: elastic cord

All results presented up to section 8.7 are results obtained with an elastic description of the spinal cord. The previously described models from chapter 5 and 6 is used on a geometry describing idealized versions of the spinal cord. The meshes have the same dimensions as found in previous work by Drøsdal (2011), [38]. The height of the model is 60mm, and the spinal cord have a radius r=5mm. The distance from the cord to the rigid dura mater is 4 mm, and this space is where CSF flows. The fluid cavity, where free fluid flow is allowed, is placed in the centre of the model, extending between heights 10mm and 50mm in the longitudinal direction. We investigate three cases: No syrinx, a case with syrinx 1 mm radius and a syrinx with 3 mm radius. We will refer to the case r=3mm as a large syrinx and r=1mm as a small syrinx. The origin is placed at the bottom of the cord at the centerline such that the geometry is spanned by the rectangle defined by the two points (-9,0) and (9,60).

First, a sinusoidal varying pressure was applied to the boundaries with a maximum of 20 Pa difference between top and bottom. This applied pressure gradient was reported by Drøsdal to result in peak velocities of around 5-6 cm/s assuming a rigid, but porous cord. Simulations were run 10 seconds where a steady state was reached (i.e. measurements do not change from cycle to cycle). To ensure our solution to be grid independent, mesh-refinement tests are done. The results are summarized in tables under the three following subsections. In doing so, quantities of interest are the peak velocity in the SAS, $\max|\mathbf{v}|$, the peak velocity inside the syrinx in the spinal canal, $\max|\mathbf{v}_{sc}|$ and the maximum displacement, $\max|\mathbf{U}|$ in both x- and y-direction.

Tables for the mesh refinement tests follow in the next three subsections.

8.4.1 No syrinx

N_x	N_y	dofs	max|**v**|[cm/s]	max|$\mathbf{U}_x$|[mm]	max|$\mathbf{U}_y$|[mm]
18	30	6281	5.68	0.007	0.02
36	60	24437	5.63	0.007	0.02
54	90	54473	5.63	0.007	0.02

Table 8.1: $E = 5kPa, \Delta t = 0.002s, T = 10, \rho_s = 1.75\rho_f$

N_x	N_y	dofs	max|**v**|[cm/s]	max|$\mathbf{U}_x$|[mm]	max|$\mathbf{U}_y$|[mm]
18	30	6281	5.68	0.002	0.006
36	60	24437	5.62	0.002	0.006
54	90	54473	5.62	0.002	0.006

Table 8.2: $E = 16kPa, \Delta t = 0.002s, T = 10, \rho_s = 1.75\rho_f$

N_x	N_y	dofs	max|**v**|[cm/s]	max|$\mathbf{U}_x$|[mm]	max|$\mathbf{U}_y$|[mm]
18	30	6281	5.67	5e-4	0.002
36	60	24437	5.61	5e-4	0.002
54	90	54473	5.62	5e-4	0.002

Table 8.3: $E = 62.5kPa, \Delta t = 0.002s, T = 10, \rho_s = 1.75\rho_f$

8.4.2 1mm syrinx

N_x	N_y	dofs	max|**v**|[cm/s]	max|$\mathbf{v}_{sc}$|[cm/s]	max|$\mathbf{U}_x$|[mm]	max|$\mathbf{U}_y$|[mm]
18	30	6281	5.94	2.10	0.20	0.08
36	60	24437	5.91	2.14	0.20	0.08
54	90	54473	5.91	2.17	0.20	0.08
72	120	96389	5.92	2.18	0.20	0.08

Table 8.4: $E = 5kPa, \Delta t = 0.002s, T = 10s, \rho_s = 1.75\rho_f$

N_x	N_y	dofs	max|**v**|[cm/s]	max|$\mathbf{v}_{sc}$|[cm/s]	max|$\mathbf{U}_x$|[mm]	max|$\mathbf{U}_y$|[mm]
18	30	6281	5.76	0.57	0.05	0.02
36	60	24437	5.68	0.57	0.05	0.02
54	90	54473	5.69	0.58	0.05	0.02
72	120	96389	5.70	0.58	0.05	0.02

Table 8.5: $E = 16kPa, \Delta t = 0.002s, T = 10s, \rho_s = 1.75\rho_f$

N_x	N_y	dofs	max|**v**|[cm/s]	max|$\mathbf{v}_{sc}$|[cm/s]	max|$\mathbf{U}_x$|[mm]	max|$\mathbf{U}_y$|[mm]
18	30	6281	5.69	0.14	0.01	0.005
36	60	24437	5.63	0.14	0.01	0.005
54	90	54473	5.64	0.14	0.01	0.005
72	120	96389	5.64	0.14	0.01	0.005

Table 8.6: $E = 62.5kPa, \Delta t = 0.002s, T = 10s, \rho_s = 1.75\rho_f$

8.4.3 3mm syrinx

N_x	N_y	dofs	max|**v**|[cm/s]	max|$\mathbf{v}_{sc}$|[cm/s]	max|$\mathbf{U}_x$|[mm]	max|$\mathbf{U}_y$|[mm]
18	30	6281	7.62	2.34	1.30	0.24
36	60	24437	7.15	2.54	1.13	0.23
54	90	54473	7.05	2.61	1.10	0.22
72	120	96389	7.01	2.66	1.07	0.22

Table 8.7: $E = 5kPa, \Delta t = 0.002s, T = 10s, \rho_s = 1.75\rho_f$

N_x	N_y	dofs	max|**v**|[cm/s]	max|$\mathbf{v}_{sc}$|[cm/s]	max|$\mathbf{U}_x$|[mm]	max|$\mathbf{U}_y$|[mm]
18	30	6281	6.11	0.79	0.34	0.06
36	60	24437	6.01	0.83	0.33	0.06
54	90	54473	6.00	0.84	0.33	0.06
72	120	96389	6.00	0.85	0.33	0.06

Table 8.8: $E = 16kPa, \Delta t = 0.002s, T = 10s, \rho_s = 1.75\rho_f$

N_x	N_y	dofs	max|**v**|[cm/s]	max|$\mathbf{v}_{sc}$|[cm/s]	max|$\mathbf{U}_x$|[mm]	max|$\mathbf{U}_y$|[mm]
18	30	6281	5.79	0.21	0.07	0.01
36	60	24437	5.70	0.21	0.07	0.01
54	90	54473	5.71	0.21	0.07	0.01
72	120	96389	5.72	0.22	0.07	0.01

Table 8.9: $E = 62.5kPa, \Delta t = 0.002s, T = 10s, \rho_s = 1.75\rho_f$

With the above tests, a mesh consisting of $2 * 54 * 90$ cells (row 3) should be sufficient to capture the qualitative behavior of the system as well as being acceptable on computational time. This version of the mesh is used in the following simulations. Most notable in these simulations is that syrinx velocities occur in the *opposite* direction to that of the surrounding CSF flow. Peak syrinx velocities range from 0.14 to 2.66 cm/s. Velocities within the syrinx only increase by approximately 25-55 % (depending on Young's modulus) when the syrinx is made 200 % wider. For a large Young's modulus, syrinx size is more critical for fluid velocities inside it. It should also be noted that syrinx size affects SAS velocities. For E = 5kPa, a small syrinx (r=1mm) increases the maximal CSF velocity in the SAS from 5.6cm/s to 5.9 cm/s. With a large syrinx, (r=3mm) maximal velocities up to 7.0 cm/s are measured. A large syrinx causes greater displacements and therefore a narrowing of the SAS. Figure 8.7 shows that this leads to greater pressure gradients in these regions and thus greater flow velocities. It is also evident that pressure amplitudes are greater in the SAS than in the syrinx, but the baseline pressure is zero for both regions. Flow patters are visualized under section 8.5.2 in comparison to

different pressure boundary conditions (left in figures 8.11 and 8.12). These figures also reveals that velocity patterns within the syrinx also differs between the two cases, something that could explain lower syrinx velocities than expected with a large syrinx. Figure 8.11 shows that the natural fluid frequency inside the large syrinx with a surrounding cord with E=5kPa is disrupted by the frequency in the SAS. This is not as evident with a small syrinx, but could be seen as syrinx as SAS velocities do not intersect at zero velocity. Figure 8.8 shows the inlet velocity as a result of the sinusoidal pressure boundary condition. The velocity profile at maximal flow is similar the parabolic Poiseuille flow, but peak velocities do not occur in the center of the SAS.

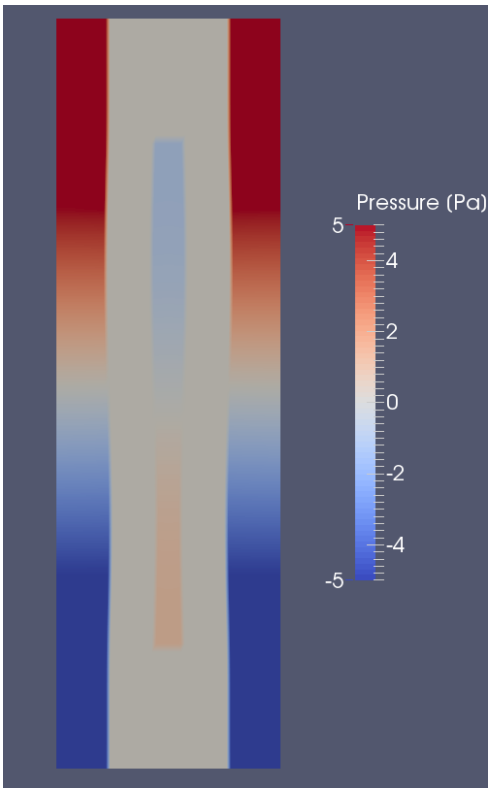

(a) Pressure field with a small syrinx

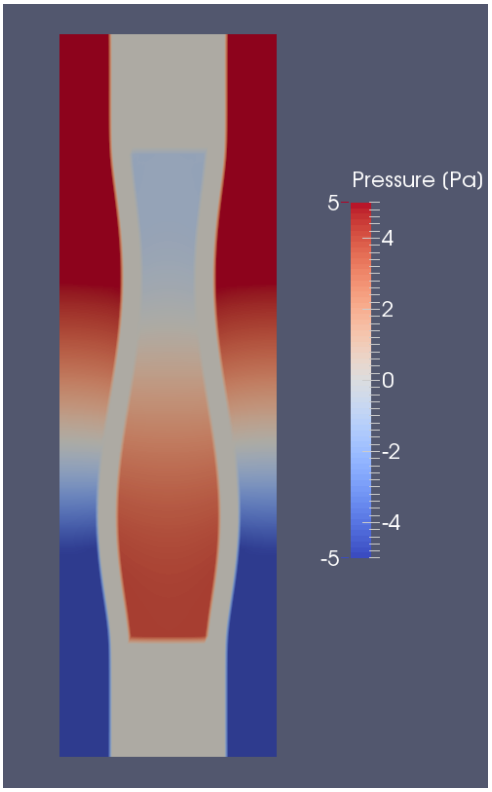

(b) Pressure field with a large syrinx

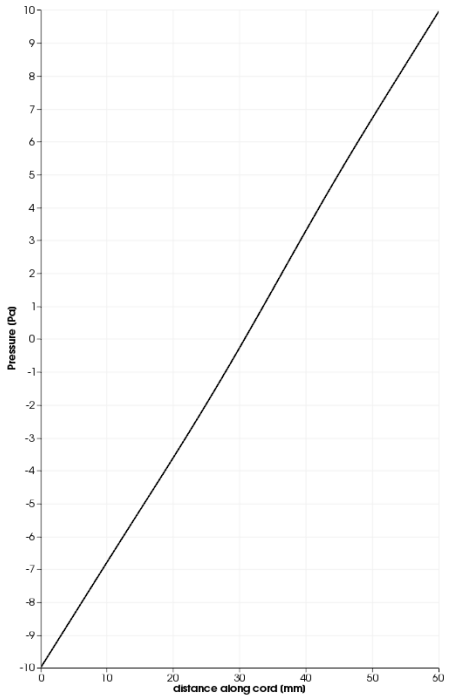

(c) Pressure along the centerline of the SAS with a thin syrinx, from bottom (y=0) to top (y=60)

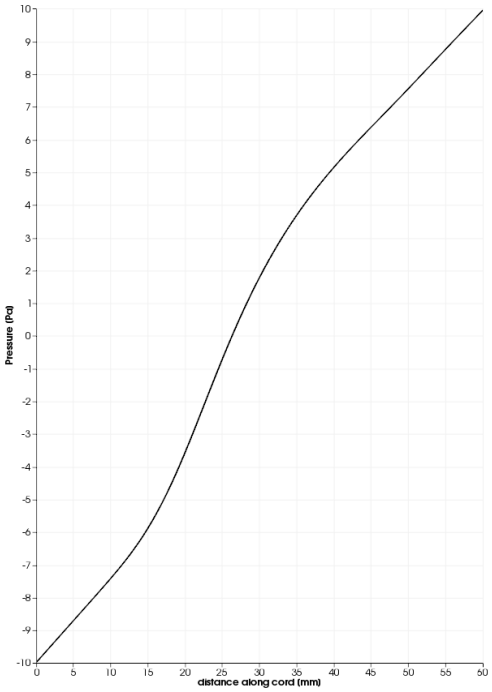

(d) Pressure along the center of the SAS with a thick syrinx, from bottom (y=0) to top (y=60)

Figure 8.7: Pressure characteristics at t=9.25 with E = 5kPa for a small (r=1mm) and large (r=3mm) syrinx. The pressure have been set to 0 Pa in the elastic cord.

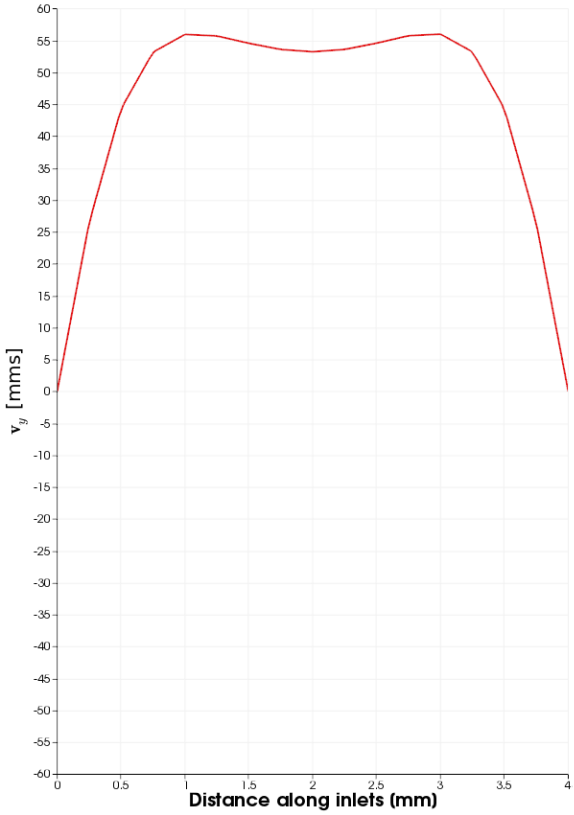

(a) Inlet velocity at t=9.0

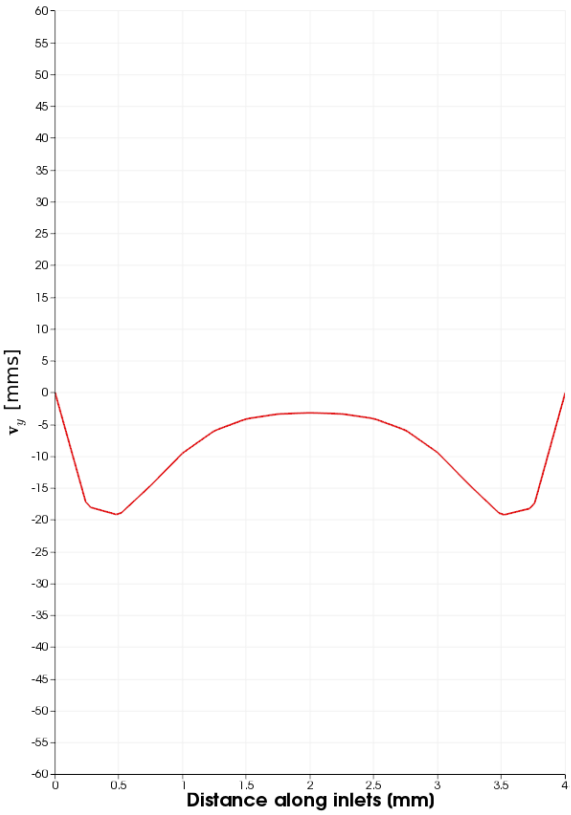

(b) Inlet velocity at t=9.25

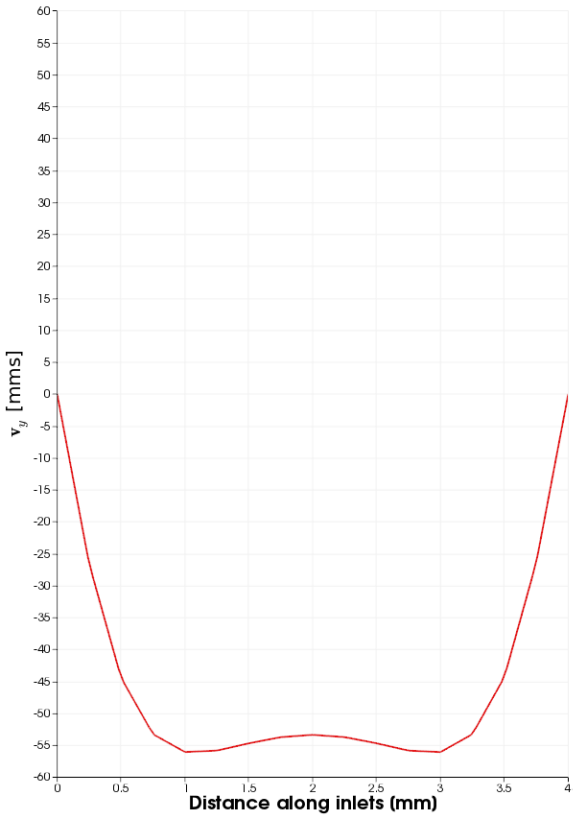

(c) Inlet velocity at t=9.5

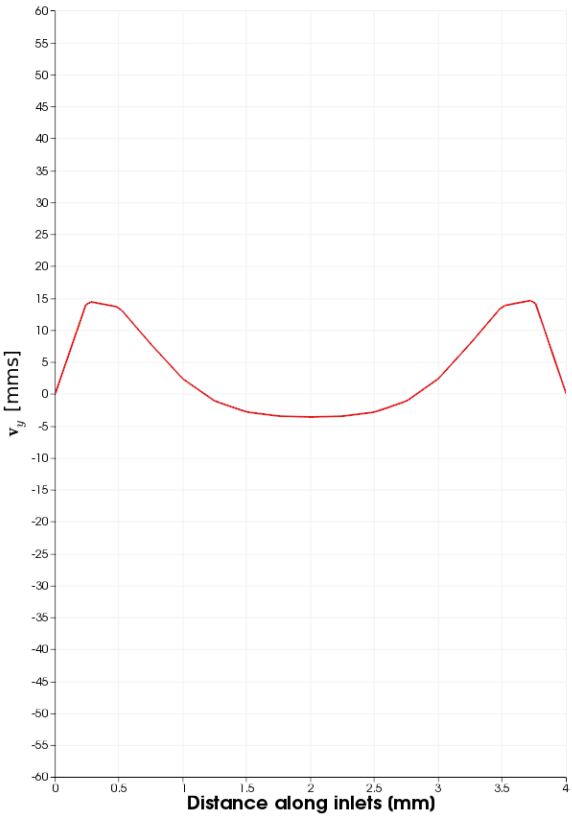

(d) Inlet velocity at t=9.75

Figure 8.8: Temporal and spatial characteristics of the resulting inlet velocities. The shape is similar on each inlet

8.5 Effect of asymmetric pressure gradient

As mentioned in section 8.1.2, pressure measurements comparing the top and bottom of the cord is hard to obtain. If the temporal data in figure 8.2 can be trusted, the temporal variation in the lumbar region is almost negligible compared to the wave amplitude in the cranial region. For this reason, we use the ICP measurements as the pressure difference between the top and bottom of the model and scale this data to obtain approximately expected CSF velocities. However, it should be noted that pressure measurements were done in the lumbar region, lower than the bottom part of the computational model presented here, and therefore the wave amplitude would be greater than in the lumbar region. The methodology is by no means perfect, but in light of theories describing formations of a syrinx, it models a more realistic case than prescribing symmetric pressure. The term *symmetric* boundary condition (or symmetric pressure gradient) is used when the applied pressure can be phase-shifted to a symmetric function. (e.g. $\sin(t)$ is denoted a symmetrical boundary condition because $\sin(t + \frac{\pi}{2})$ is a symmetric function)

The asymmetric applied pressure was obtained by extracting data from ICP measurements over one representative cycle (1.1 s) and fitting to a 5-th degree spline (See figure 8.9) to obtain continuous pressure data. The data extraction was done with ginput and image() in MATLAB with figure 8.2. This spline does not capture the pressure rise at t=0.4 of the cycle, but is reasonable within the limitations described above. The pressure was set to 0 on the bottom of the cord. Both boundary conditions were set with the Pseudo-traction condition as previously described in chapter 4 and section 8.3. Without the presence of a syrinx, this applied pressure caused maximal velocities of around 2-3 cm/s and 5-6 cm/s in the cranial and caudal directions, respectively. These values are in agreement with the studies discussed in the introduction to section 8.2. However, as can be seen in figure 8.10 flow in caudal direction has a longer duration than cranial flow, which is not the case according to the medical expert contributing to this work (Victor Haughton, M.D.). On the other hand, the data in (A) suggest net flux accumulating towards the center of the model, so these data should be used with care. In addition to setting up asymmetric velocity patterns, the asymmetric boundary condition has another interesting property in comparison to the sine-function: A steeper pressure gradient, which could be associated with the Chiari malformation as discussed in section 8.1.1, and as indicated to the left in figure 8.1. Even though the symmetric boundary conditions are not perfectly physiological plausible, we compare the symmetric and asymmetric boundary conditions to investigate the effects of a steeper pressure gradient.

To highlight differences between the two types of boundary conditions, we compare the two applied pressures with Young's modulus of E=5kPa.

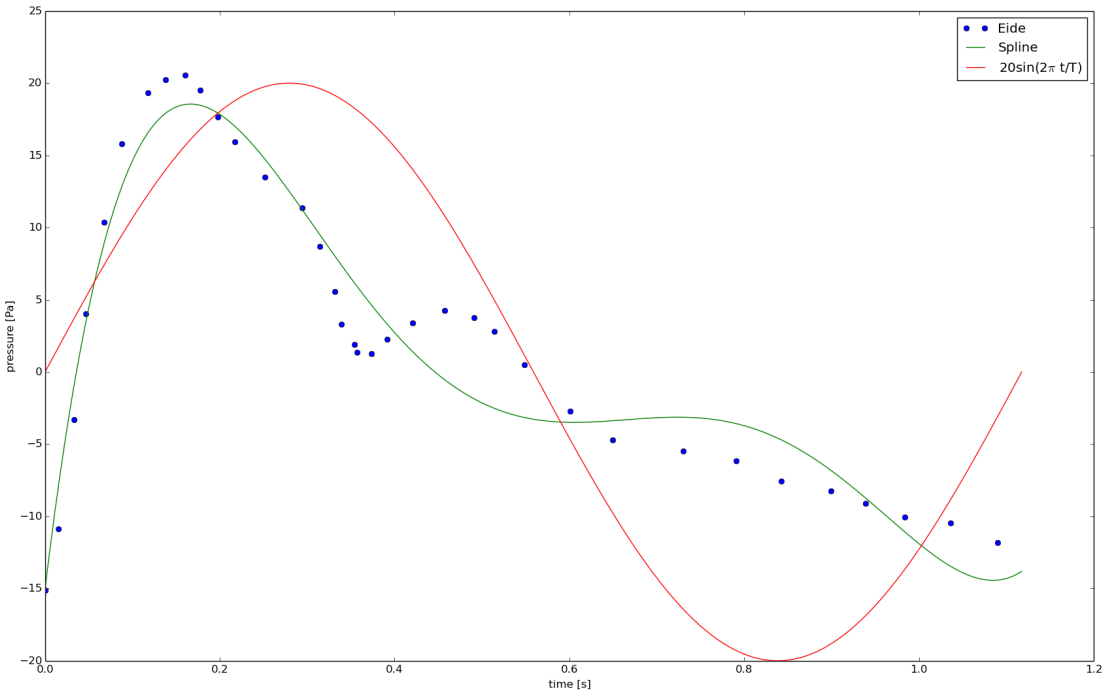

Figure 8.9: Pressure difference between top and bottom of the cord in comparison to measured ICP by Eide. In order to compare pressure characteristics, the sine function have been stretched out to match the period T=1.1 from the measured data.

8.5.1 No syrinx

Without a syrinx, radial displacements of the cord are in general very small compared to the diameter of the cord. (< 0.1 %). The manual shift of the spline in figure 8.9 to achieve the desired peak velocities in the SAS resulted in a considerable net flux in the caudal direction. This is not expected, and not realistic. However we investigate effects on cord motion and syrinx velocities as a preliminary result. At least, including the rapid rise in pressure should cause displacements patterns in the cord to differ compared to the sinusoidal wave. More discussion related to the pressure wave is given in section 8.6 and appendix B. Displacements and vertical velocities with the symmetric and asymmetric boundary conditions are shown in figure 8.10. Displacements are measured at the left cord wall at height y=55mm. The velocity is measured at the same height in the middle of the surrounding SAS. Radial displacement patterns are in phase with pressures from figure 8.9. The asymmetric pressure gradient causes greater displacements even though SAS velocities are lower.

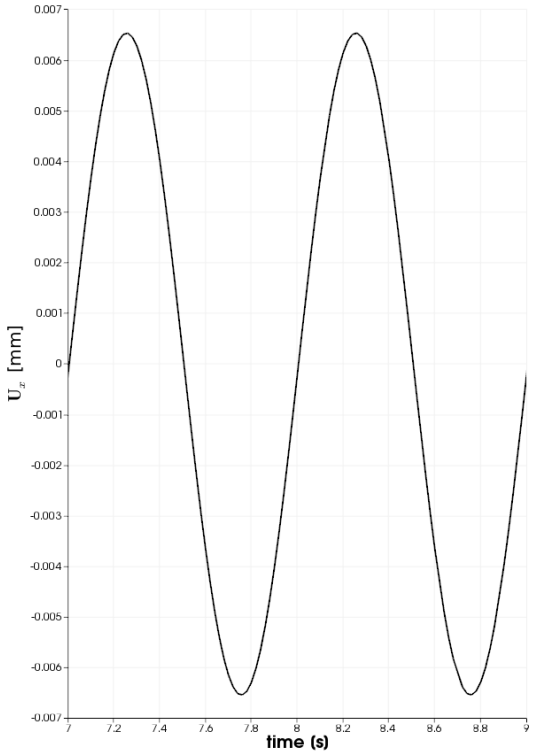

(a) Displacement in x-direction [mm] with symmetric applied pressure

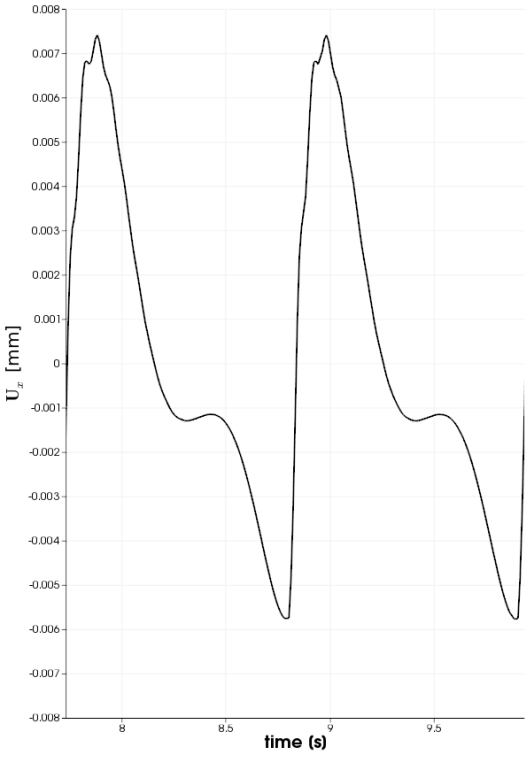

(b) Displacement in x-direction [mm] with asymmetric applied pressure

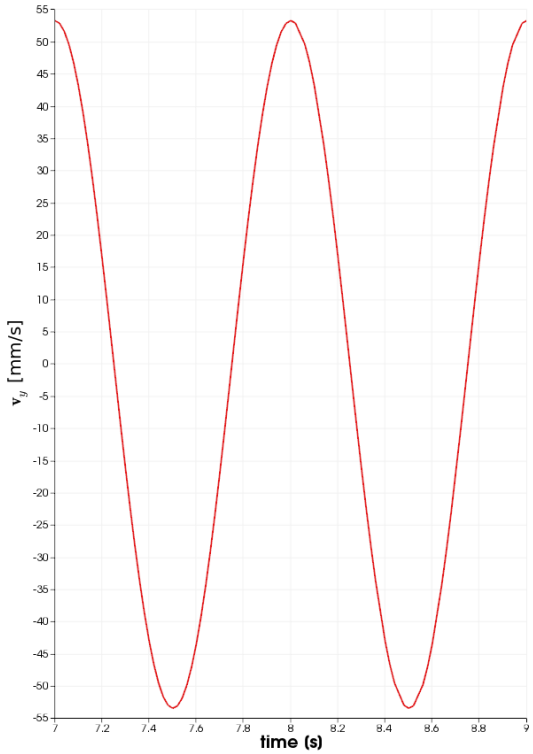

(c) Vertical velocity [mm/s] with symmetric applied pressure

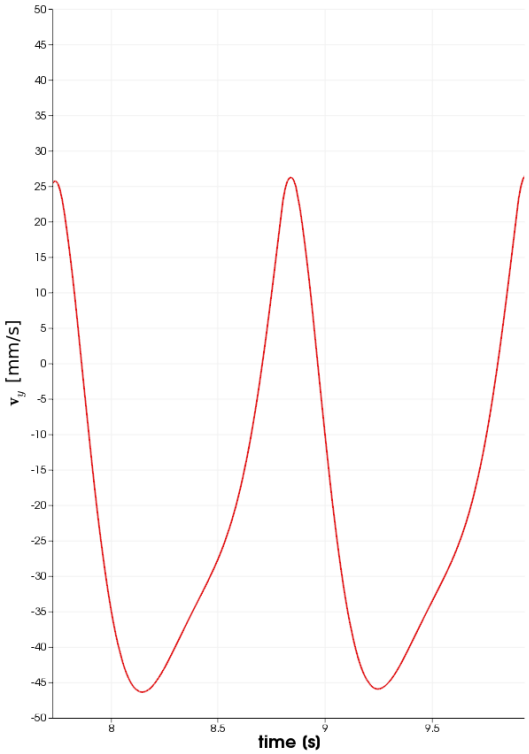

(d) Vertical velocity [mm/s] with asymmetric applied pressure

Figure 8.10: Comparison of displacement and velocity patterns over two cycles without syrinx. E=5kPa

8.5.2 Effect on syrinx velocity dynamics

SAS velocity patterns are affected by the change in pressure environment, but the shape is still fairly intact, not too different from a sinusoidal variation. On the other hand, velocities within the syrinx differ drastically. The introduction of an additional oscillation as well as increased peak velocities inside the syrinx, even though SAS velocities are lower are the most striking. Double syrinx velocity frequency compared to the surrounding SAS is also reported by Brucker et al. (A). Their subject had a large syrinx (depicted in the left frame of figure 8.2). In shape, post-operative syrinx velocities obtained with PC-MRI (A) seem to be in agreement with the right frame figure 8.11 (large syrinx), with every other peak being equal. A similar pattern is shown in figure 8.12 with a small syrinx. Symmetric boundary conditions causes CSF flow in the SAS and flow within the syrinx to be approximately 180 degrees out of phase. Our results suggests that the relative timing of the pressure wave compared to the oscillating fluid movement within the syrinx is of great importance. It seems evident that the timing of the pressure wave oppose fluid velocities within the syrinx to the left in figure 8.11. SAS velocities follow a sinusoidal pattern, while this periodic movement seem to be disturbed within the syrinx, causing peak velocities to slow down. This relative timing seem to be more enhancing on syrinx velocities in the right frame of figure 8.12, and might explain why peak syrinx velocities are higher with a small syrinx. It should also be noted that a small syrinx has less fluid to accelerate each cycle.

When cord motion is large, peak velocities might occur in different directions at different sections of the cord. The narrowing and widening of the cord causing CSF to flow faster in narrow regions and slower in wider regions. Temporal patterns in the middle of the SAS is shown in figure 8.13. In the most extreme cases, this effect might be partly responsible for abnormal pressure and flow environments in the short term after decompression surgery. Abnormalities in CSF short term following surgery was also shown by Brukcer et al. A. Visually, no difference in tonsillar herniation can be seen when comparing 2 months and 10 months post operative images. However, the associated velocity patters in the SAS were different.

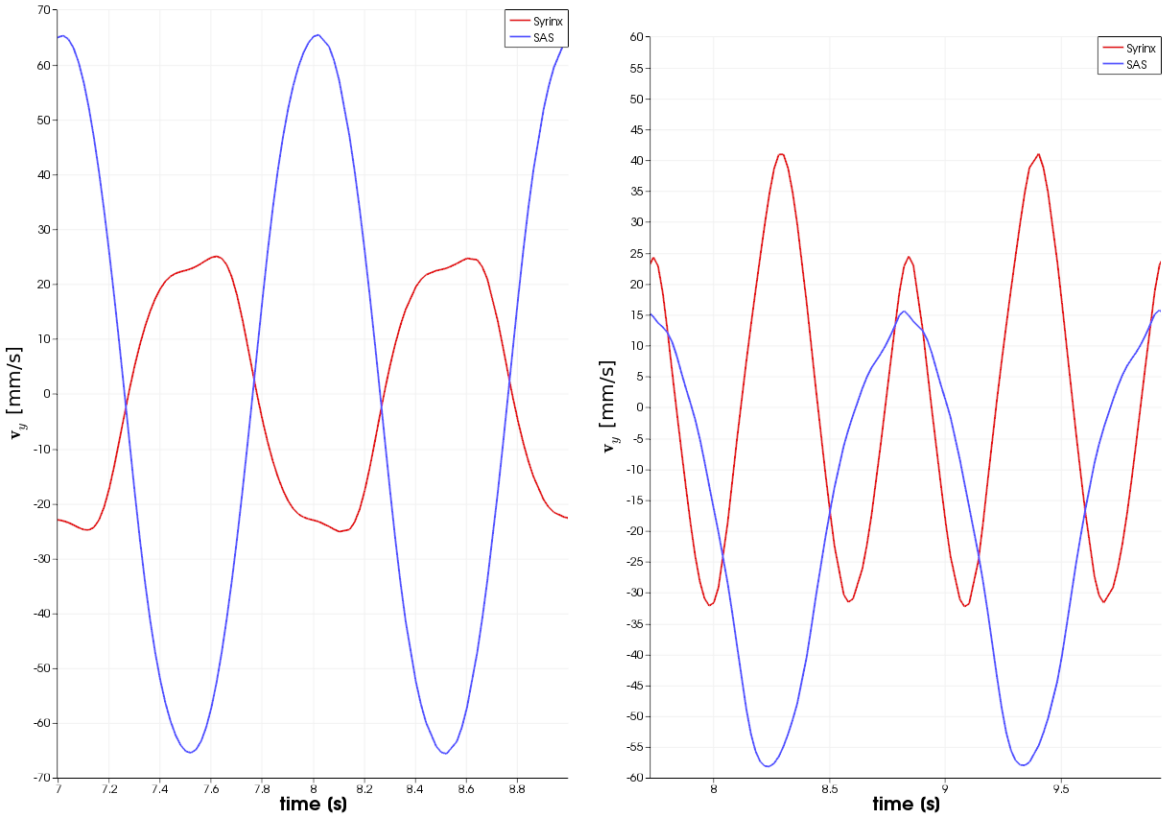

Figure 8.11: Syrinx velocity together with corresponding SAS velocities with symmetric (left) and asymmetric (right) boundary conditions with a large (r=3mm) syrinx. $E = 5$ kPa

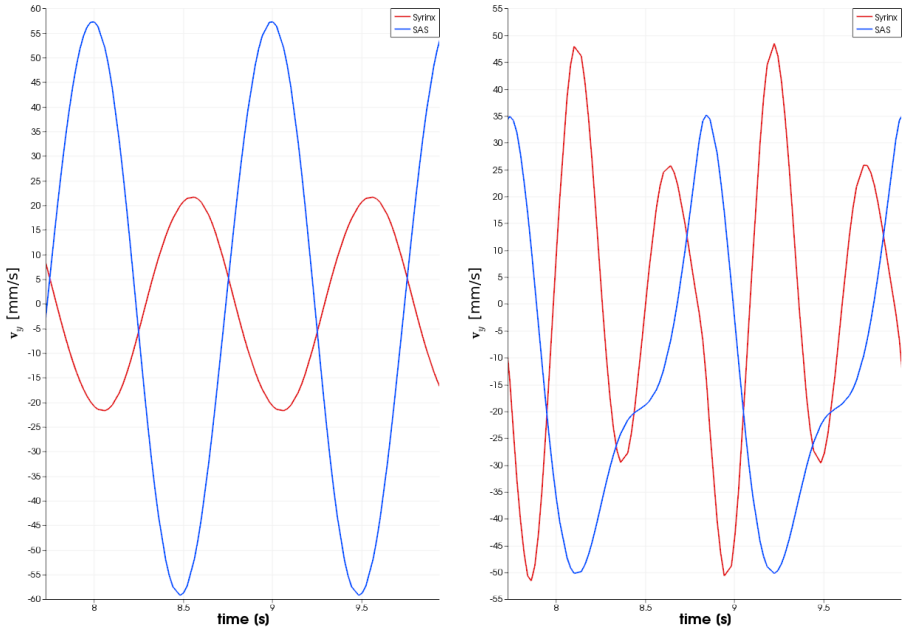

Figure 8.12: Syrinx velocity together with corresponding SAS velocities with symmetric (left) and asymmetric (right) boundary conditions with a small (r=1mm) syrinx. E = 5 kPa

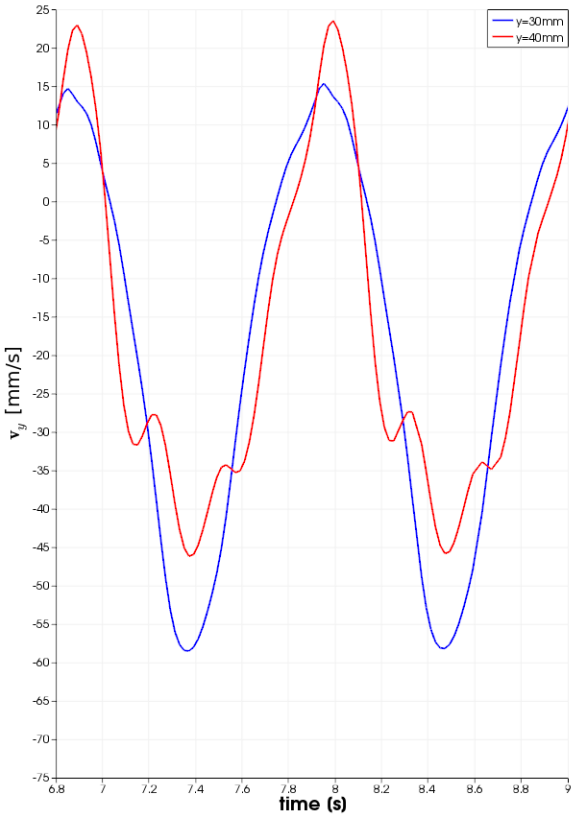

Figure 8.13: Comparison of SAS velocities at different heights of the model. E = 5kPa

8.6 Shape of the pressure wave

Previous authors [17, 79, 94] have frequently assumed a pressure similar to that reported as ICP by Frič and Eide (2015) [88] and shown in figure 8.9. It is possible that this pressure wave is the main driver of CSF flow, and that the pressure difference $\mathrm{d}p(t) = p_{C1} - p_{C7}$ between the regions C1 and C7 has a similar shape. This pressure difference is characterized by a short period of positive pressure gradient (i.e. $p_{C1} > p_{C7}$) during systole (heart contracts) and a long resting period with a small negative pressure gradient during diastole (heart refills with blood). It is commonly believed that these pressure waves causes short rapid fluid movement in the caudal direction and slow, steady flow in the cranial direction. This is not in agreement with our results from figure 8.10c, where cranial flow only occurs 25 % of the cardiac cycle. This is partly explained by greater peak velocities caudally, but is most probably caused by an incorrect shape of the pressure wave in our simulation.

If pressure is the main driver of channel flow, the velocity and pressure are related approximately through

$$\rho \frac{\partial v}{\partial t} = -\nabla p$$

And shows that if pressure is the main driver of channel flow, a pressure gradient causes *changes* in velocity, meaning changes in velocity sign must occur after than sudden changes in sign for pressure gradients (i.e. the velocity needs more time to "adjust" to sudden changes in pressure environment). From the opposite point of view, a forced change in velocity, must result in an even faster change in pressure gradient especially when there is a change in velocity direction. Therefore, if systole is characterized by the length of the positive plug-shaped pressure, the CSF may not change its flow direction before roughly halfway through systole. Similarly, the transition to diastole causes CSF to slow down, but because of the low magnitude of the negative pressure gradient during diastole, the velocity will flow the same direction for a longer period. This means that the plug shaped pressure gradient used causes longer periods of flow in the caudal direction unless some great downwards spike" also exists to quickly slow down the rapid fluid movement. At steady sinusoidal flow, the pressure wave is 90 degrees out of phase compared to the CSF wave. This need not be the case for other characteristics of flow or velocity.

It should also be noted that due to viscous forces, the integral of $\mathrm{d}p(t)$ does not necessarily need to be zero.

Using standard channel flow with the previously validated coupled CFD solver, the extracted pressure measurements by Eide at ICP was normalized and shifted to cause zero net flux and prescribed as the boundary condition at C1, the pressure (pseudo traction) was set to 0 Pa at the end of the channel. Surprisingly, if the function is turned upside down" (i.e. multiplied with -1), we obtain the velocity patterns as described in the literature. (see figure 8.14). The net flux over a cycle is zero, the maximal caudal velocity is 5-6 cm/s and the maximal cranial velocity is 3 cm/s. It still possible that the pressure gradient has a short, powerful upstroke but

these simple tests show that there also need to be a strong force (i.e. a great negative pressure gradient) quickly causing CSF to slow down and eventually change the flow direction to cranial. This observation was further investigated, by applying also these boundary conditions to the elastic and poroelastic models. To also investigate the pressure rise at $t \approx 0.4s$ of the cycle, we use a PChipInterpolator from scipy to fit the data set. This pressure rise is present at most heart beats, but does not occur every cycle (see B). To visualize the flow-pressure coupling, the vertical

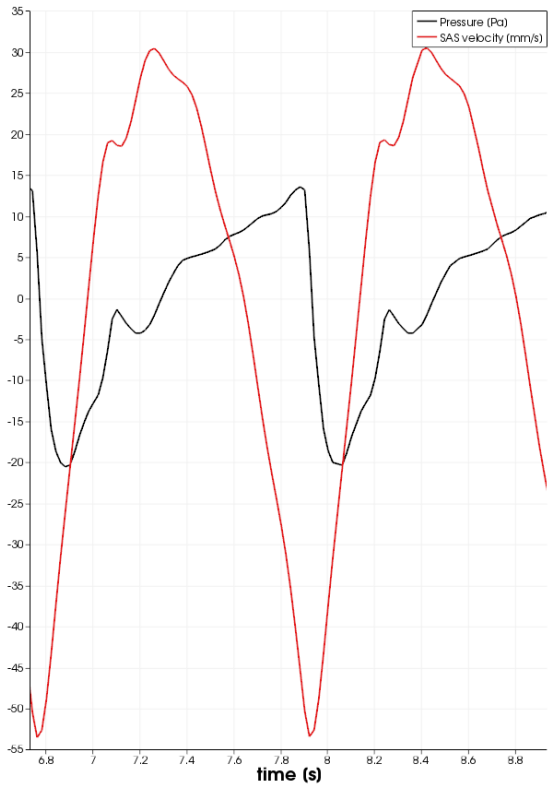

Figure 8.14: Pressure difference between top and bottom and velocities in the same plot for the elastic model. E=62.5 kPa, no syrinx

velocity is plotted together with velocity in figure 8.14 with the most rigid cord. The inlet velocities in the elastic model has the same shape as preliminary tests with rigid walls. Both quantities are measured at inflow boundaries, and the flow is aligned along the axis of the cord. The pressure rise at the middle of systole creates a short decline in velocity, which slightly prolongs the period of cranial flow. Other than that, this rise (here, decline) in pressure does not seem to qualitatively affect velocities in the SAS. However the short "bump" in velocity during upstroke is the exact same as seen in appendix A. Peak velocity occur in the caudal direction, but the temporal change of the velocity is considerably greater at upstroke because of the sharp decline in pressure at the top.

8.7 Results: poroelastic cord

Without a syrinx, we measure the same quantities as before in addition to the maximal Darcy flux in the cord, $\max|\mathbf{q}|$ as well as the magnitude of the flux in the center point of the cord, $\max|\mathbf{q}|_0$. The pressure boundary conditions are now sinusoidal, as in section 8.4. Additional mesh refinement tests are performed with a 1mm syrinx to ensure mesh independence. Other tables are given for different values of E,

8.7.1 No syrinx

E [kPa]	$\max\|\mathbf{U}_x\|$[mm]	$\max\|\mathbf{U}_y\|$[mm]	$\max\|\mathbf{q}\|$[cm/s]	$\max\|\mathbf{q}\|_0$ [cm/s]	
5	5.63	0.006	0.02	4.12e-6	3.28e-8
16	5.62	0.002	0.007	3.51e-6	3.36e-8
62.5	5.62	5e-4	0.002	2.42e-6	3.37e-8

Table 8.10: Comparison of different values of E. No syrinx, $\Delta t = 0.002$, $[N_x, N_y] = [54, 90]$

8.7.2 1mm syrinx

N_x	N_y	$\max\|\mathbf{v}\|$[cm/s]	$\max\|\mathbf{v}_{sc}\|$[cm/s]	$\max\|\mathbf{U}_x\|$[mm]	$\max\|\mathbf{U}_y\|$[mm]	$\max\|\mathbf{q}\|$[cm/s]
18	30	5.78	1.48	0.13	0.06	2.93e-6
36	60	5.71	1.46	0.13	0.06	7.82e-6
54	90	5.70	1.47	0.13	0.06	1.40e-5

Table 8.11: $E = 5$kPa, 1mm syrinx, $\Delta t = 0.002$

N_x	N_y	$\max\|\mathbf{v}\|$[cm/s]	$\max\|\mathbf{v}_{sc}\|$[cm/s]	$\max\|\mathbf{U}_x\|$[mm]	$\max\|\mathbf{U}_y\|$[mm]	$\max\|\mathbf{q}\|$[cm/s]
18	30	5.68	0.53	0.05	0.02	2.39e-6
36	60	5.67	0.53	0.05	0.02	6.72e-6
54	90	5.68	0.49	0.04	0.02	1.09e-5

Table 8.12: $E = 16$kPa, 1mm syrinx, $\Delta t = 0.002$

The Darcy flux is small but mesh dependent, and thus our model would need further refinement to capture effects of accumulation of flow towards the syrinx. This thesis do not intend to explain the accumulation towards the syrinx, but this could be investigated as future work. For the other variables, mesh refinement does not seem to critically alter the solution.

N_x	N_y	max|**v**|[cm/s]	max|$\mathbf{v}_{sc}$|[cm/s]	max|$\mathbf{U}_x$|[mm]	max|$\mathbf{U}_y$|[mm]	max|**q**|[cm/s]
18	30	5.69	0.13	0.01	0.005	2.05e-6
36	60	5.63	0.13	0.01	0.005	4.52e-6
54	90	5.63	0.13	0.01	0.005	7.30e-6

Table 8.13: E = 62.5kPa, 1mm syrinx, Δt = 0.002

8.7.3 3mm syrinx

E [kPa]	max|**v**|[cm/s]	max|$\mathbf{v}_{sc}$|[cm/s]	max|$\mathbf{U}_x$|[mm]	max|$\mathbf{U}_y$|[mm]	max|**q**|[cm/s]
5	6.26	1.14	0.41	0.08	7.32e-5
16	5.98	0.71	0.22	0.05	7.93e-5
62.5	5.61	0.21	0.07	0.01	1.70e-5

Table 8.14: Comparison of different values of E. 3mm syrinx, Δt = 0.002, $[N_x, N_y]$ = $[54, 90]$

Comparing table 8.14 with table 8.11, it is evident that a larger syrinx does not necessarily imply a larger peak syrinx velocity in the poroelastic model. This could be related to the relative timing of the pressure compared to syrinx velocities as discussed in section 8.5.2.

8.8 Comparison of Elastic and Poroelastic models

Poroelastic models predict smaller displacements and lower peak syrinx velocities than elastic models. Maximal peak syrinx velocities reached 2.66 cm/s in the elastic model and 1.47 cm/s in the poroelastic model. From a physical point of view, this is reasonable, as waves entering the poroelastic cord can also be damped by fluid entering the spinal cord, and thus some energy is transmitted to slow fluid movement within the cord rather than structural displacement. Elliott (2012) [95] discussed pressure wave damping in 1D-models, and found that the propagation of the pressure wave is aided by a less permeable pial membrane but a more permeable spinal cord. This suggests that syrinx velocities predicted by poroelastic models in this thesis might be underestimated, and that the permeability is an important factor in syrinx velocity dynamics. In the SAS, great displacements predicted by the elastic models causes CSF to flow faster in regions where the SAS is temporarily narrowed and slower where it is temporarily wider.

The velocity profile in the SAS is more sensitive to variations in Young's modulus with the elastic model than with the poroelastic model. This is due to greater displacements predicted by the elastic model. From figure 8.16 the velocity pattern seem to be completely different for the elastic model, with greater peak velocities in the cranial direction. At the middle height, the cord radially contracts with downward movements of fluid causing CSF to flow slower in the wider regions of the SAS. Similarly, when the cord radially contracts, a wider SAS results in faster upward fluid movement in these specific regions. At $y = 40$, for instance, the opposite is the case. Here the cord expands at downward fluid movement causing faster flow downwards.

To investigate differences during a sharp pressure pulse, we apply the asymmetric boundary condition as described in 8.6 to the two models. One of the most striking differences is the impact of the mentioned damping effect on syrinx velocities. Figure 8.15 compares elastic and poroelastic models with the most rigid cord (E=62.5 kPa). In the elastic model, the pressure pulse causes rapid fluid movement in the cranial direction (opposite to that in the SAS) within the syrinx and when the pulse reaches the bottom of the syrinx cavity, it is reflected back and forth until a new pulse arrives. These oscillating patterns are also predicted by Bertram (2009) [15] after a cough. With E = 62.5 kPa, peak syrinx velocities are below what is measured in vivo as mentioned in section 8.2. These velocities appears in the cranial direction and reaches 1.1 cm/s and 0.4 cm/s with the elastic and poroelastic models, respectively. In figure 8.16, it becomes evident that also syrinx velocities are more sensitive to variations in Young's modulus in elastic models compared to poroelastic. By reducing Young's modulus to E = 5 kPa, peak syrinx velocities increase to 6 cm/s in the elastic model, while only reaching 0.6 cm/s in the poroelastic model.

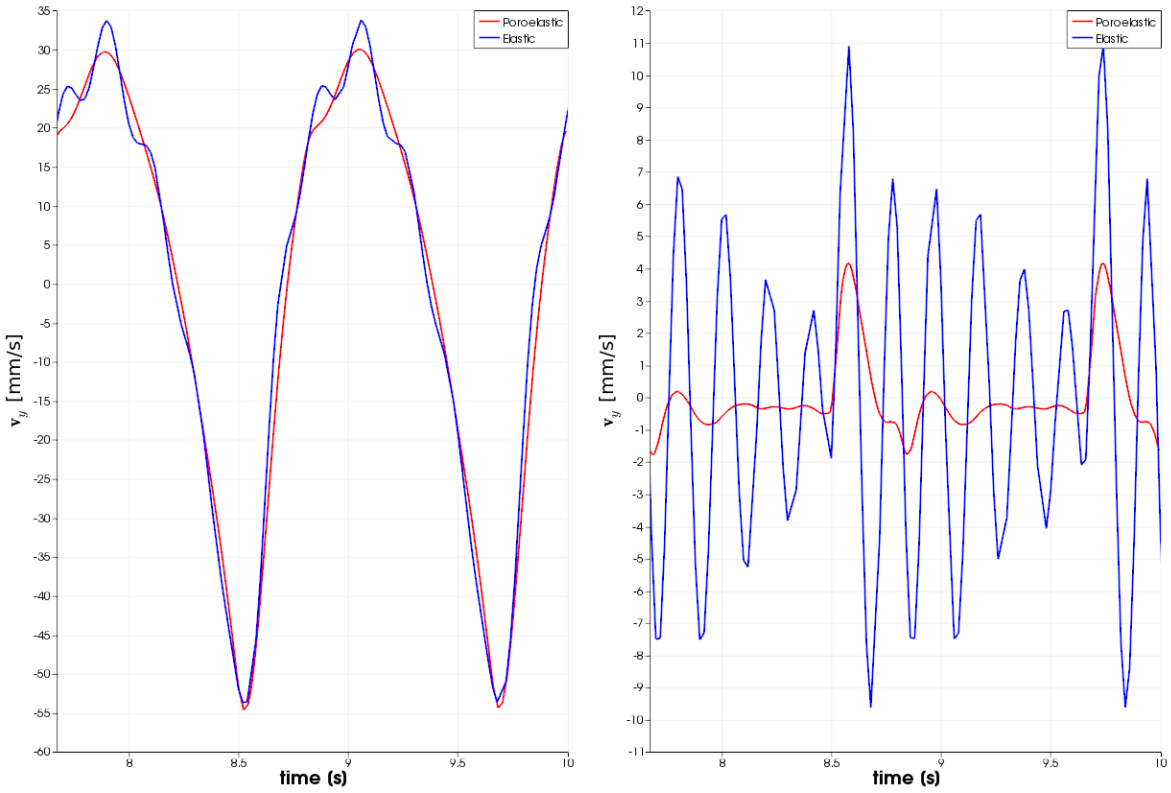

Figure 8.15: Comparison of SAS velocities (left) and syrinx velocities (right) for a thick syrinx (r=3mm). E=62.5 kPa

An interesting observation is that the waveform of the inlet pressure seems to be directly related to the temporal variation of syrinx velocities. In figure 8.17 pressures at the inlet is plotted together with velocities in the middle of the syrinx for the poroelastic model. If such a direct coupling between the two should exist, no major reflections of fluid should be present in the syrinx, and the fluid velocity within it should be relatively low at the arrival of the pressure pulse. Considering the low velocities often reported near the end of the cardiac cycle, it is not unlikely that the gradient and amplitude of the pressure wave could have a direct impact on syrinx velocity, and thus be directly related to the impact of the slosh mechanism. With E = 62.5 kPa, this close relation was also present in the elastic model at the arrival of the pressure pulse, but after the initial wave, reflections dominated syrinx velocity characteristics until a new pulse arrived.

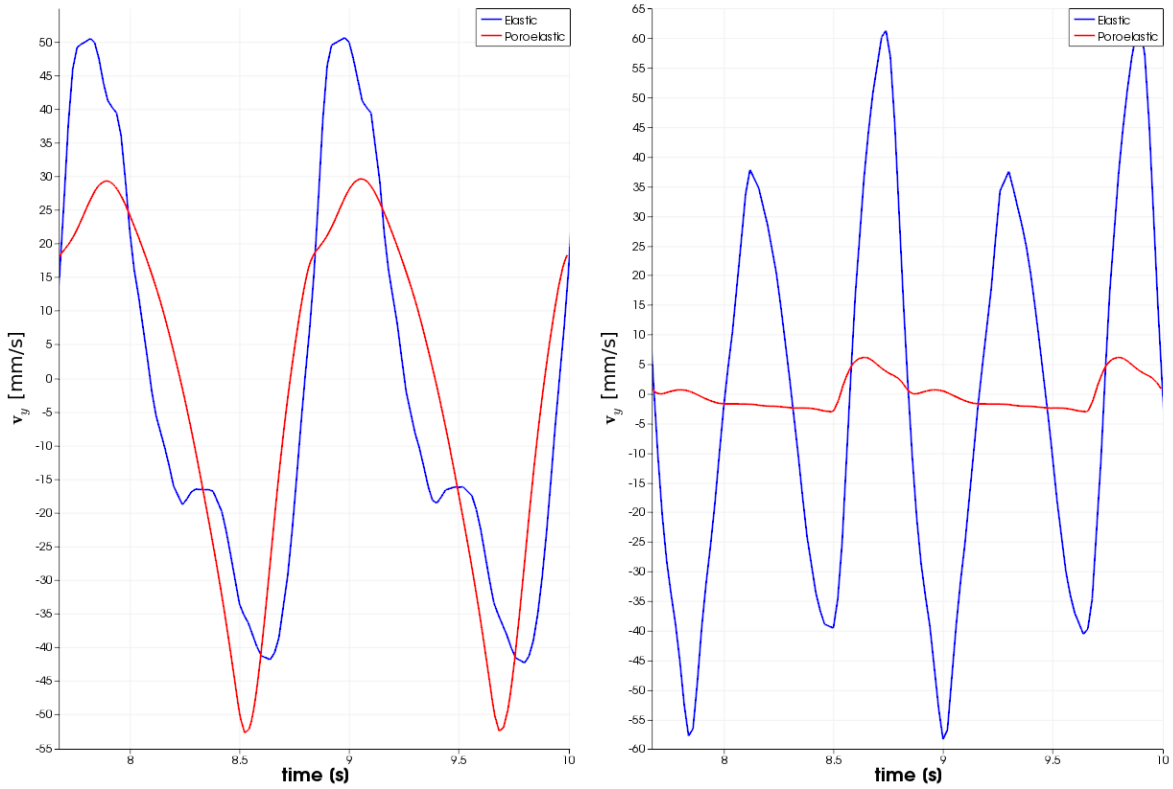

Figure 8.16: Comparison of SAS velocities (left) and syrinx velocities (right) for a thick syrinx. E=5 kPa

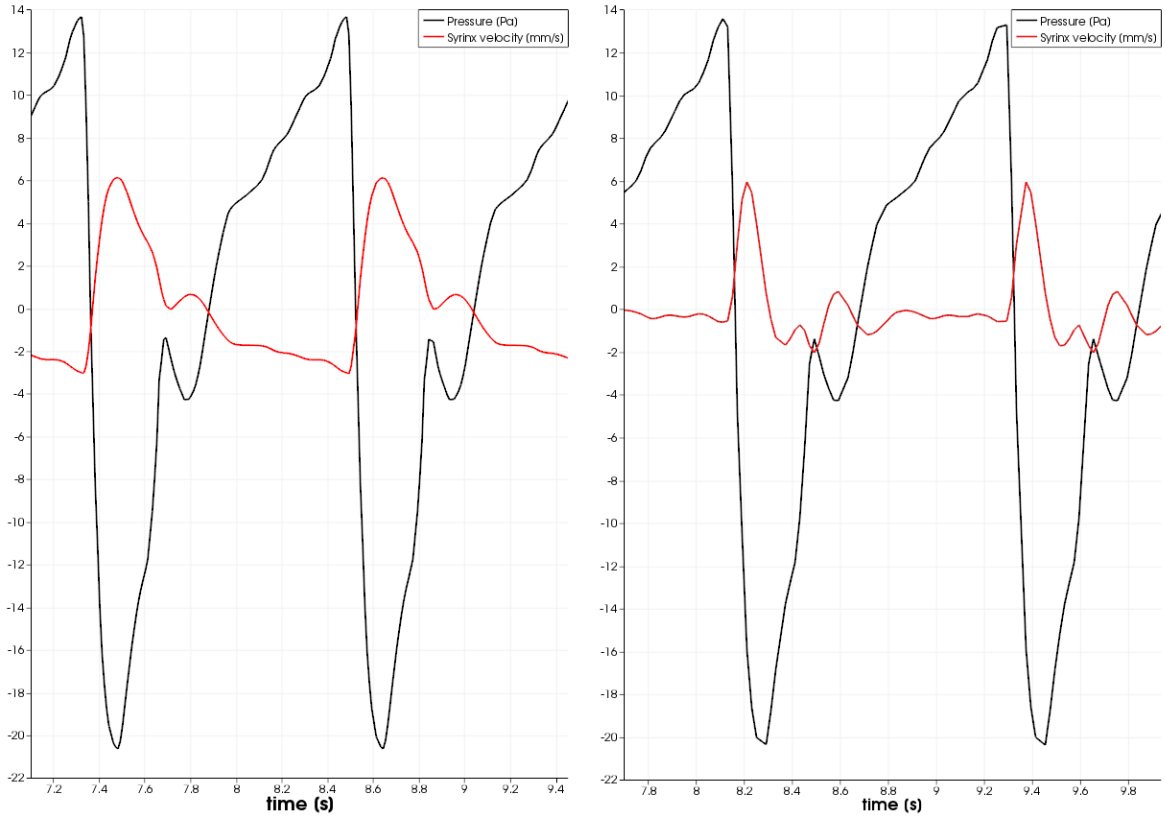

Figure 8.17: Comparison of pressure wave and corresponding syrinx velocities with $E = 5$ kPa (left) and $E = 62.5$ kPa (right)

Chapter 9

Discussion, Conclusions and Future Work

9.1 Discussion

We have developed models for elastic and poroelastic representation of the spinal cord in interaction with CSF in the SAS. Elastic models have been validated against benchmark results in a different geometry. Poroelastic models were shown to be grid independent for the quantities of interest for three different values of Young's modulus. The main concern with the poroelastic models in this case lie in the approximation of pressure continuity on the interface on the macro scale, especially in the case of only a thin tissue separating the SAS and the syrinx.

We have shown that the slosh effect can be explained with FSI or poroelasticity due to an asymmetric pressure boundary condition. Exact characteristics of syrinx velocities under the cardiac cycle can not be determined from this study due to uncertainty in the pressure wave applied to the system as well as other limitations explained in the next section. With a sinusoidal varying SAS velocity, syrinx velocities were shown to occur in opposite direction for all elastic models. In these models SAS velocities of 5.5 - 7.0 cm/s resulted in syrinx velocities of 0.2 - 2.6 cm/s with a large (r=3mm) syrinx and 0.14 - 2.2 cm/s with a small (r=1mm) syrinx. Another interesting finding is that under physiologically realistic conditions (i.e. slow fluid velocities before a sharp pressure pulse arrives) syrinx velocities seem to be directly related to the shape of the pressure pulse. Syrinx velocities were shown to be asymmetric pressure gradients, syrinx size and elastic properties of the cord also altered these patterns, and in agreement with Pinna (2000) [93], we might conclude that these patterns may vary from patient to patient.

As compared to Clark (2013) [9], and Cheng et al. (2014) [10], our experiments have given further evidence that FSI-effects on CSF-dynamics are negligible in models of healthy subjects. In these models more than a 10-fold increase in Youngs modulus gives at most a decrease in 0.02 cm/s, ($< 0.5\%$) and no visible effect on CSF-velocities. Cord displacements vary approximately linearly with Youngs modulus, an expected result with a linear elasticity model. The greatest displacements are

7μm and 20μm in the radial and axial directions, respectively. These displacements are below the resolution limit of MRI. [80]

In the diseased state, (i.e. in the presence of a syrinx) Bertram (2010) [16], Martin et al. [80, 12] have all concluded that effects of FSI on pressure in the SAS as well as syrinx velocities are important. In these models, the presence of a syrinx leaves only a small segment of spinal cord tissue between it and the surrounding SAS. This allows for greater displacements of the cord and thus fluid movement inside the syrinx. Our elastic models predict the same importance of FSI in the case of syringomyelia. Syrinx velocities are comparable to in vivo results by Brucker (A), and in vitro results by Martin et al. (2010), but does not quantitatively match in all our experiments. For instance, the long resting phase during diastole with slow, almost constant SAS velocities were not seen. In addition, high-frequent oscillations within the syrinx, (in our model, due to a more rigid spinal cord) have not been reported during the cardiac cycle. Peak syrinx velocities in the elastic models range from 0.14 cm/s to 6.1 cm/s.

Poroelastic models dampen FSI effects by allowing some fluid to flow into the spinal cord. The extent of damping is affected by spinal cord permeability [95], which was not investigated further in our model. The poroelastic models did not predict rapid oscillations within the spinal cord during the cardiac cycle. Peak syrinx velocities in these models ranged from 0.13 cm/s to 1.47 cm/s. Our models were not accurate enough to capture accumulation of fluid flow towards the cord, where an accuracy for fluid velocity of order 10^{-8} m/s is needed within the spinal cord tissue.

The main difference between the two models is in presence of a short and steep pressure pulse, where the relative timing of the pulse compared to the oscillatory movement within the syrinx is crucial for peak syrinx velocities. This relative timing of the pressure pulse has been reported to be of importance for syrinx progression [96].

The pressure field within the syrinx is opposite of that in the SAS in both models, meaning rapid change in pressure from the CSF along the cord wall to fluid within the syrinx. The pressure wave in the possibly thin tissue separating the two is complex and still needs more investigation. In contrast with Martin et al. (2005), [80] a general statement whether pressure is higher in the SAS or in the syrinx can not be given. To analyze pressure differences between the SAS and inside the syrinx, points of equal height should be used as the pressure varies along the cord both in the SAS and in the syrinx. At a given height, pressures have similar shape, but differs in amplitude. The SAS pressure has greater amplitudes, and thus syrinx pressure will be greater than SAS pressure when pressures are below baseline pressures.

New pressure measurements by Frič and Eide (2015) [88] suggests substantial damping of the signal as the pressure pulse travels along the spinal cord. According to these result, the damping is to the extent that reflecting waves from the bottom

of the spinal cord could be neglected. Exceptions include coughing as discussed by Bertram (2009) [15] and also shown in vivo by Williams (1976) [90]. These pressure data did not give the expected flow patterns, (i.e. slow steady upwards, and a short, powerful peak downwards) but Quigley (2004) [4] reported velocities opposite of that, more similar to figure 8.10d shifted upwards. However, Quigley's study contradicts other studies of CSF flow and can not be fully trusted. On the other hand, if peak velocities appear in the cranial direction, anatomical differences *below* the site of the syrinx could also be of importance. Thompson et al. (2015) [26] studied differences in tapering, showing that Chiari I patients with syringomyelia had a wider spinal canal at C7 than Chiari patients without syringomyelia. No significant difference were found at C4. This causes CSF velocities to increase when moving towards C4 in the cranial direction which again alters the pressure environment.

9.2 Limitations

This study has limitations, and in the following we mention some.

9.2.1 Geometry

Our simulations were done in 2D channels and are not directly comparable to 3D results. We expect many of the same characteristics to be present in 3D models as well, but quantitative comparison between simulation and in vivo measurements is limited. As mentioned earlier, our model ignore branching nerves from the spinal cord, as well as perivascular spaces. Bilston et al. (2010) [96] have suggested the latter to play an important role in fluid accumulation within the cord resulting in syrinx formation. Obstruction at the foramen magnum could affect the relative timing of CSF wave resulting in pressure differences between the CSF in the SAS and fluid within perivascular spaces. This study did neither include perivascular spaces, nor fluid obstruction at the foramen magnum. If inclusion of obstructions had been done in our model, a drawback is that the two channels do not directly communicate (i.e. fluid can not flow from one channel to the other).
The inclusion of a thin and stiff pia mater was shown by Støverud et al. (2015) [18] to be important by increasing radial pressure gradients. The pia permeability has also been shown to affect fluid accumulation within the cord [95]. Inclusion of a pia mater justifies the choice of a low Young's modulus of the spinal cord (E = 5kPa). If this value is representative for the cord itself, rapid oscillations within the syrinx will not be seen. The dura mater (outer fluid walls) have been assumed rigid, which is not true but does probably not affect the solution as the dura mater is of several orders higher magnitude stiffer than the pia mater and cord.

9.2.2 Boundary conditions

The pressure boundary conditions determines both CSF and syrinx velocity dynamics, and the pressure used in this study is approximated by a sinusoidal waveform or based on assumption that might not be completely correct. Pressure measurements

are done intracranial and in the lumbar region, while Chiari related patient-specific computational models typically focuses on the upper part of the cord. In addition to this the no slip boundary condition for structural displacement at the top and bottom will not be completely realistic. At the top and bottom of the cord, the fluid velocity also had to be set to 0 in the poroelastic model. Before conclusions with reliable results can be done, validation of this assumption could be done by e.g. extending the model caudally. The same concern is present for the fluid flux at the top and bottom in the poroelastic models. Also, because continuous elements were used for pressure, the conclusion that the Beavers-Joseph Saffmann condition is negligible might be erroneous.

9.2.3 Model equations

Biot's theory has been simplified by omitting the inertia term of the Darcy flux. Linear elasticity has been assumed for the structural part which, at best, only holds for small deformations. In addition assumption of continuity of pressure over the interface due to linear elements in FEniCS could introduce some errors.

9.2.4 Physiological understanding

The physiological concept of CSF production and circulation is not fully understood. It is not clear whether the net flux over a cycle has to be zero. To the most extreme, we have heard of studies reporting a net flux of 50L CSF in the cranial direction over a 24h period. These results have not been published, but opens the possibility that CSF might leave the SAS in intracranial regions, and later reappear at the bottom of the spinal cord. Furthermore, the possibility of tearing of biological tissue due to slosh is something we did not investigate.

9.3 Conclusions

9.3.1 Syrinx velocities explained in silico

Our model has provided a mechanical explanation for syrinx velocities within the spinal cord. The magnitude of syrinx flow is related to elastic properties of the cord, and the temporal variation is possibly directly related to the shape of the pressure wave in the SAS.

9.3.2 Applicability of in vivo pressure measurements

In vivo pressure measurements give new insight to the understanding of pressure-velocity coupling in the SAS. Although this is fairly well understood in healthy subjects, computer models applying Dirichlet conditions at both caudal and cranial ends should be able to predict measured pressure in the same way as our model should be able to predict SAS velocities. To our knowledge we are the first to apply these in vivo pressure measurements to computational models.

9.3.3 Poroelasticity alters syrinx dynamics

Poroelastic results differ from elastic results mainly by the syrinx velocity in response to a sharp pressure pulse. Most importantly, poroelastic models preticts substantial damping of the initial pressure pulse as well as damping of oscillatory syrinx velocities during diastole.

9.4 Future Research

Expanding the model to 3D would be beneficial, but so far we have not managed our meshing tools (Gmsh, mshr) to generate matching surfaces with an ellipsoid (syrinx) enclosed by two cylinders (spinal cord and SAS) as a starting point for idealized models. With the present model, it would be interesting to investigate whether the exact in vitro experimental setups by Martin et al. (2005,2010) [80, 12] could be replicated and produce the same results. This would also include some kind of obstruction of the SAS in our model. The computational model presented in this thesis could be a starting point to compare these in vitro studies. Furthermore, the recent discovered difference in spinal canal anatomy between Chiari I patients with and without syringomyelia [26] could be subject to computational investigation with our model. Propagation characteristics of the pressure wave needs more investigation, because the shape of the pressure wave could be directly related to syrinx velocities. As a beginning, damping of pressure waves along the cord in the poroelastic models can be compared to damping reported in pressure measurements by Frič and Eide (2015) [88]. As the pressure wave can both enhance and oppose fluid movement within the syrinx depending on the frequency, we suggest that heart rate could be investigated as a variable affecting peak syrinx velocities.

Appendices

Appendix A

Assessment of CSF Velocities using MRI

The following graphics show CSF velocities obtained with MRI. Curtesy of Justin Brucker, MD, Victor Haughton, MD, Allison Grayev, MD and Andrew Wentland, PhD. We would like to thank Justin Brucker for allowing this unpublished data to be used in this thesis. The 14-year old female subject underwent decompression surgery, and CSF velocities were measured with PCMR before, 2 months after and finally 10 months after surgery, when symptoms had vanished. The CSF velocities are measured in 12 different regions over a cross section named after the numbering around the clock. Thus, plots labeled as a reference to the clock, shows CSF velocities at a given position of a cross section over one cycle (14 measurements were done each cycle). 6 different cross sections were analyzed: C1, C1-C2, C2-C3, C3, C3-C4 and C4-C5. What should be noted is the extreme variety, and if the flux of each cross section is analyzed, too much fluid seem to accumulate in the center of the SAS. Figure A.1 shows an example of tables in the spreadsheet of raw data. The flux column has been calculated by the author. The study only involved one subject, and can not be used as a certain measurement of exact CSF velocities. It is an interesting direction in measuring syrinx velocity dynamics and long term improvement of CSF characteristics. In these images, and in most medical literature, positive values means in the caudal direction (i.e. downwards)

C1-C2	Position	6:00	7:00	8:00	9:00	10:00	11:00	12:00	1:00	2:00	3:00	4:00	5:00	Syrinx	Average	Flux
	Area (mm^2)	11.43	14.06	12.3	14.06	14.94	18.46	15.82	14.94	14.94	19.34	14.06	14.94	7.91		
Phase	Time (ms)	1.97	Vel (cm/s)	Vel (cm/s)	Vel (cm/s)	Vel (cm/s)	Vel (cm/s)	Vel (cm/s)	Vel (cm/s)	Vel (cm/s)	Vel (cm/s)	Vel (cm/s)	Vel (cm/s)	Vel (cm/s)	Vel (cm/s)	
10	577	0.62	0.38	0.57	1.2	0.71	-0.76	-0.66	-0.43	0.1	0.74	0.29	0.8	1.18	0.30	0.478598
11	640	0.72	0.85	0.77	0.93	0.49	-0.83	-0.63	-0.78	-0.03	0.67	0.47	0.73	0.89	0.28	0.431304
12	703	0.86	0.59	0.65	0.86	0.41	-0.78	-0.7	-0.57	0.12	0.87	0.54	0.62	1.09	0.29	0.458224
13	766	1.47	1.38	1.4	1.72	0.13	0.19	-0.23	-0.54	0.61	1.49	1.25	1.52	1.99	0.87	1.495653
14	829	3.11	2.34	2.88	2.93	4.18	3.08	2.51	3.6	3.89	2.29	2.83	2.73	1.74	3.03	5.408469
1	10	2.11	0.64	1.84	1.85	7.32	3.95	2.26	3.62	4.72	1.92	3.06	1.45	0.93	2.90	5.262087
2	73	1.5	-0.08	1.5	1.06	9.4	3.44	1.53	2.4	5.4	1.39	2.48	0.73	0.6	2.56	4.667064
3	136	0.98	0.21	0.51	0.62	7.97	2.1	0.18	0.63	4.97	0.8	1.45	0.76	0.94	1.77	3.20707
4	199	1.37	0.13	0.52	0.54	5.45	0.62	0.19	-0.66	3.3	0.35	0.8	0.86	1.11	1.12	1.976563
5	262	1.13	0.4	1.29	1.39	4.61	0.53	0.2	0.46	3.17	1.07	1.41	1.1	1.53	1.40	2.469561
6	325	1.13	0.29	1.06	1.01	3.63	0.56	0.05	0.27	2.56	0.95	1.1	0.86	0.76	1.12	1.985603
7	388	0.61	0.18	0.78	0.83	2.45	-0.03	-0.39	-0.28	1.68	0.71	0.8	0.62	0.77	0.66	1.158045
8	451	0.61	0.25	0.57	0.59	1.28	-0.68	-0.69	-0.78	0.7	0.49	0.33	0.64	0.98	0.28	0.439311
9	514	0.14	0.15	0.57	0.88	0.9	-0.92	-0.93	-0.53	0.44	0.39	0.32	0.59	1.19	0.17	0.24355

Figure A.1: Example of CSF velocities. Measurements at the C1-C2 level

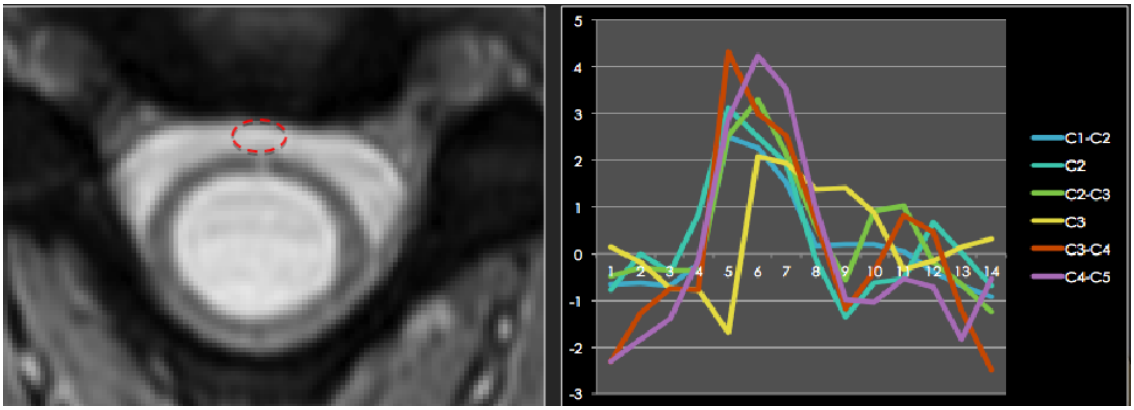

(a) Velocities at 12:00

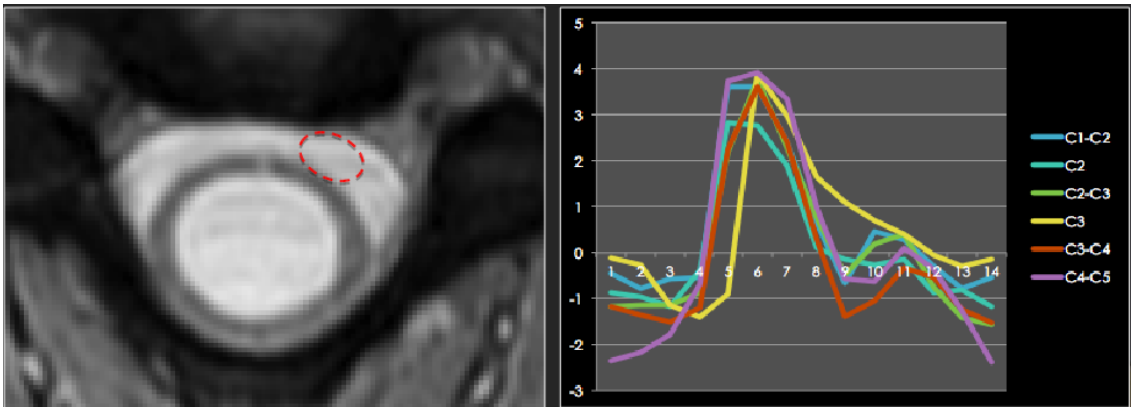

(b) Velocities at 1:00

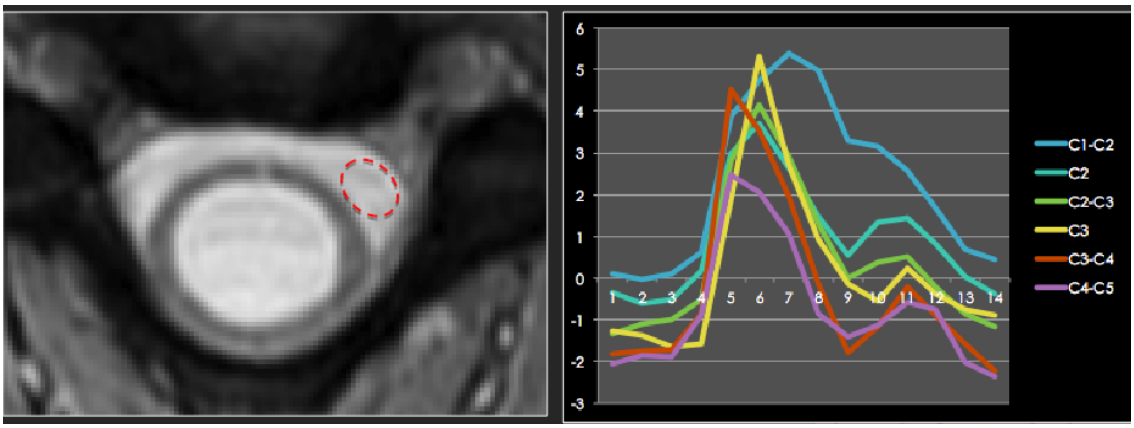

(c) Velocities at 2:00

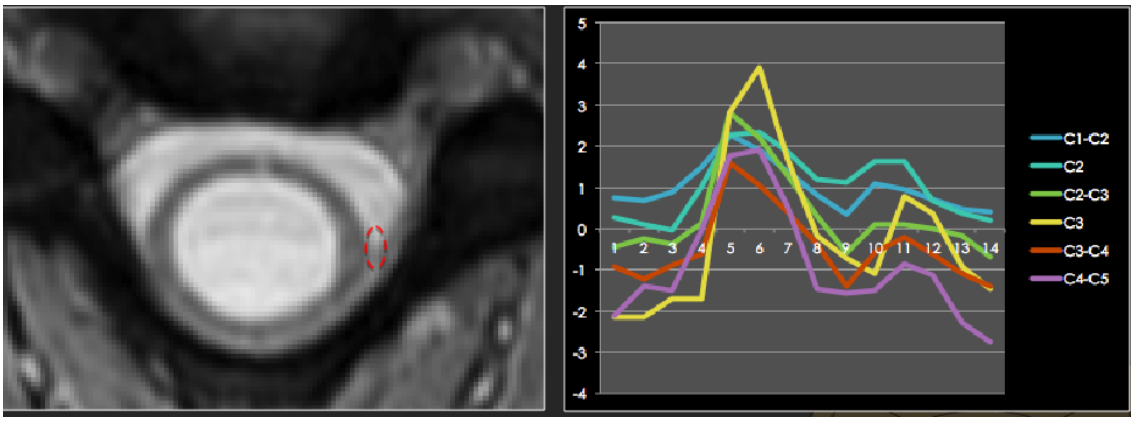

(d) Velocities at 3:00

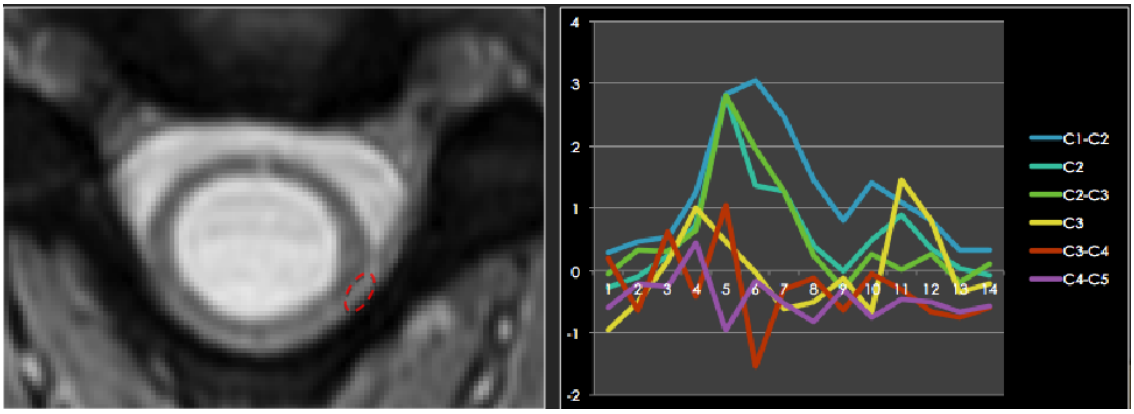

(a) Velocities at 4:00

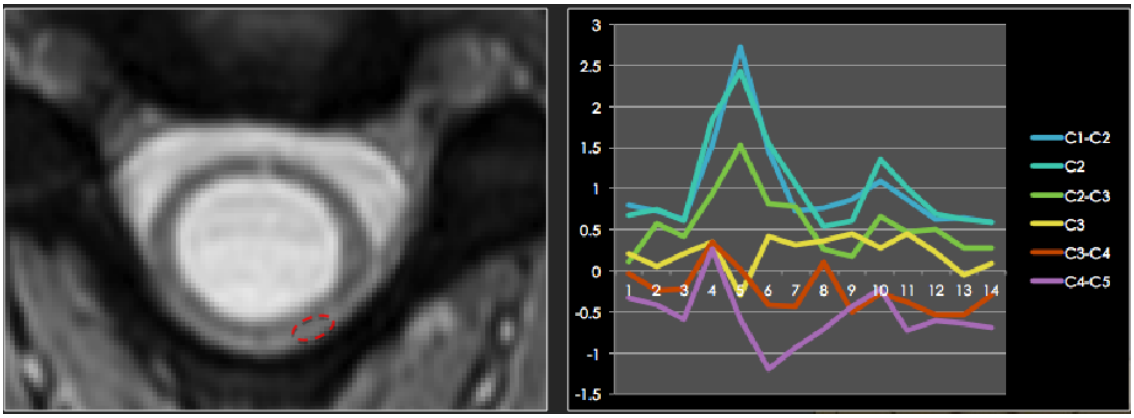

(b) Velocities at 5:00

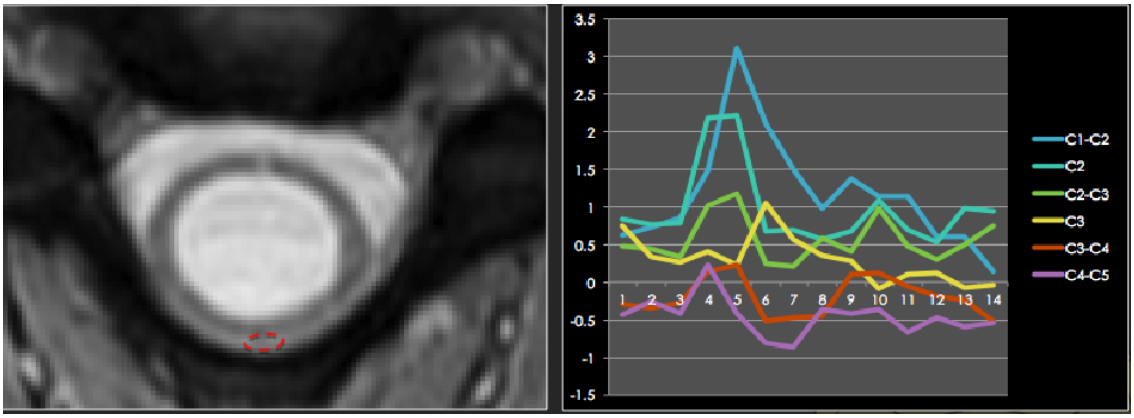

(c) Velocities at 6:00

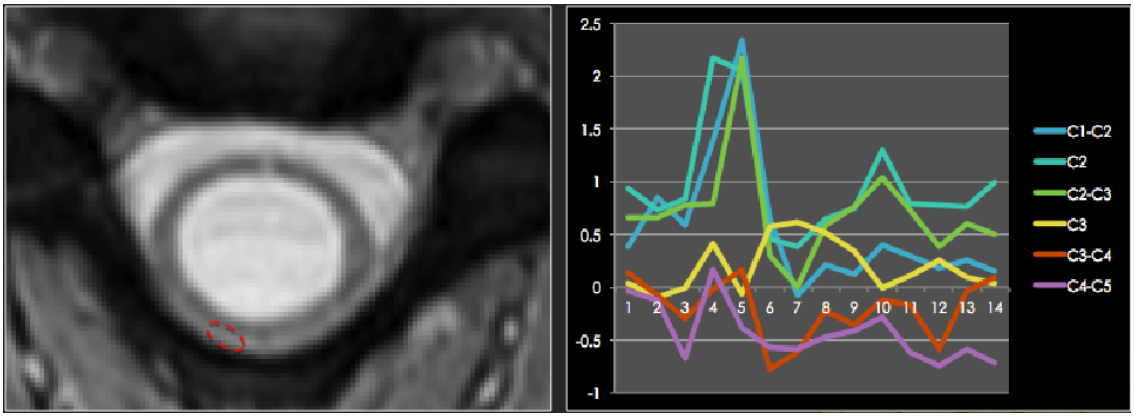

(d) Velocities at 7:00

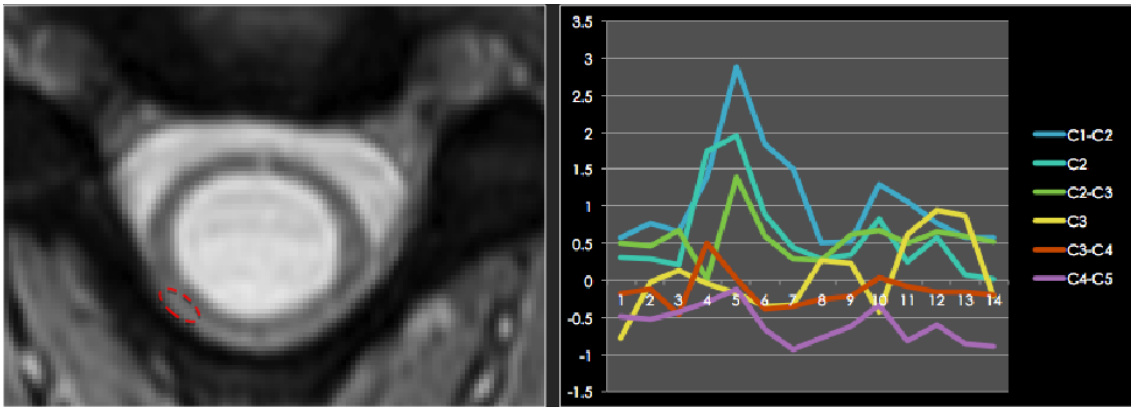

(a) Velocities at 8:00

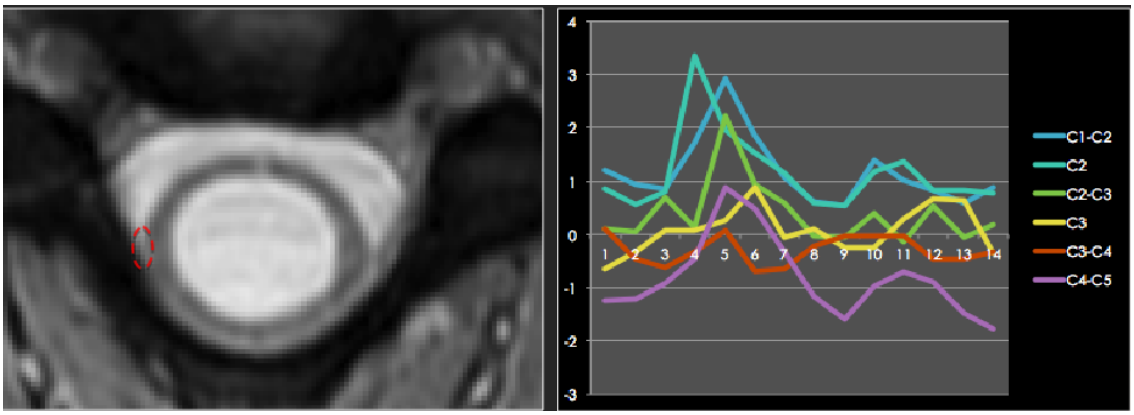

(b) Velocities at 9:00

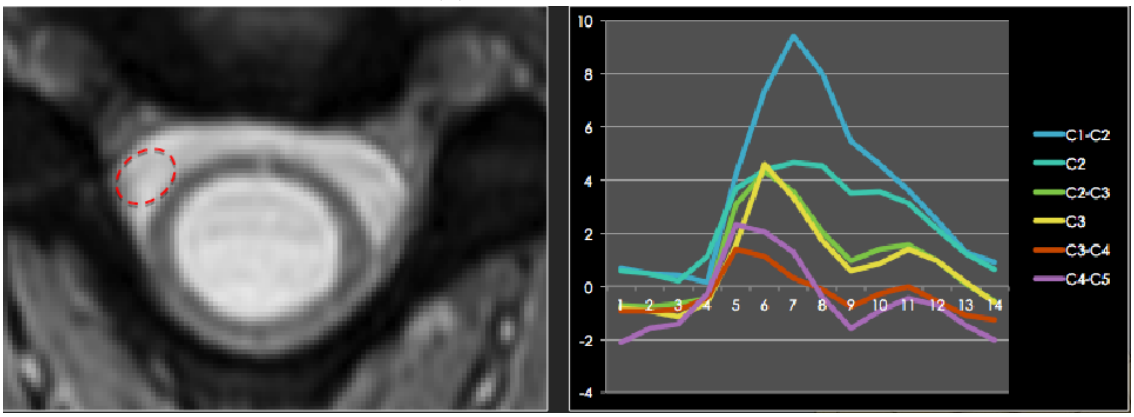

(c) Velocities at 10:00

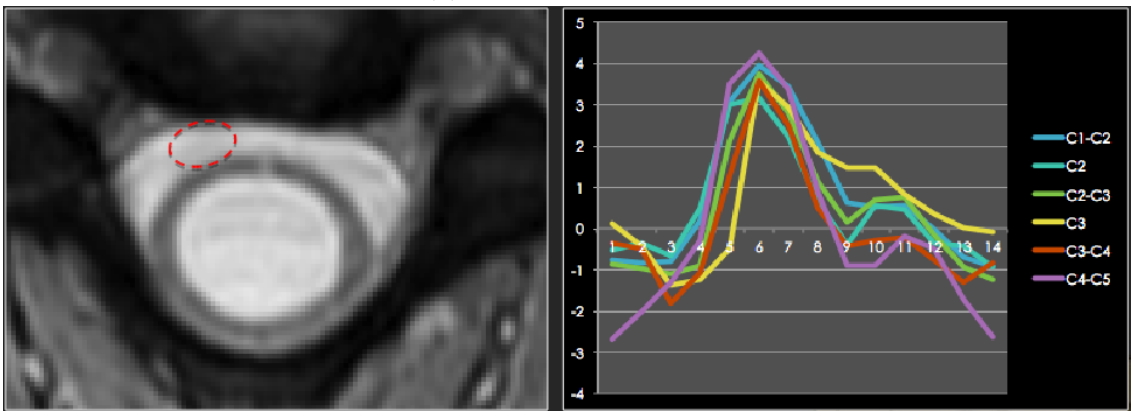

(d) Velocities at 11:00

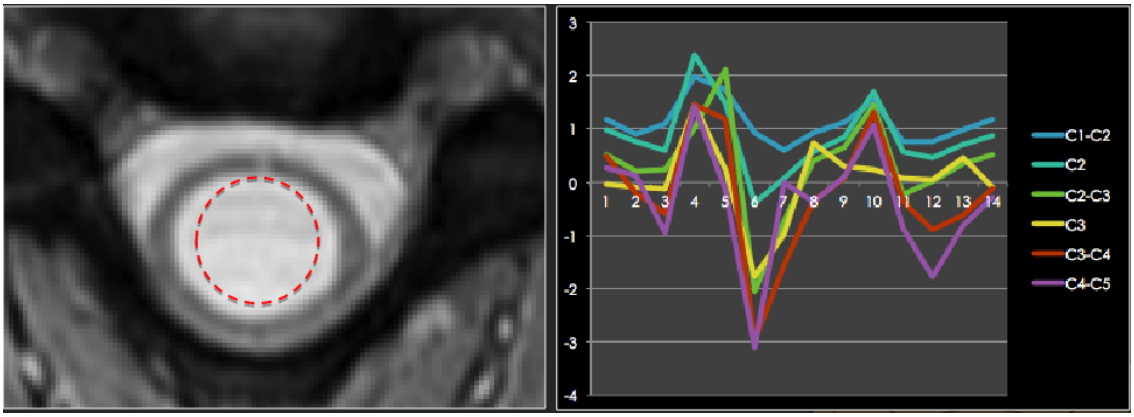

Figure A.5: Syrinx Velocity

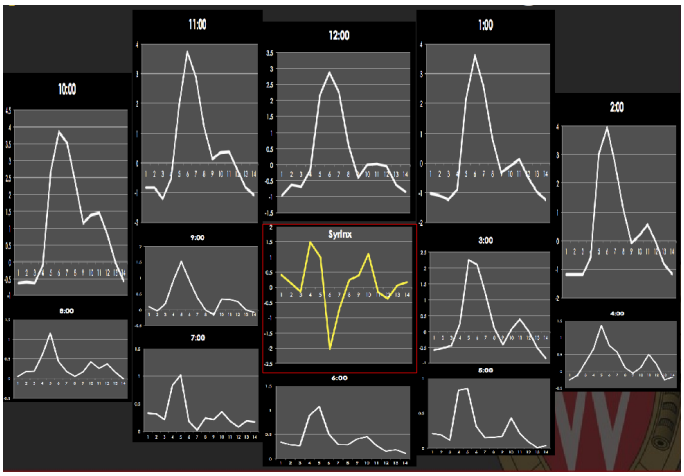

Figure A.6: Preoperative CSF velocities over a cross section (weighted average)

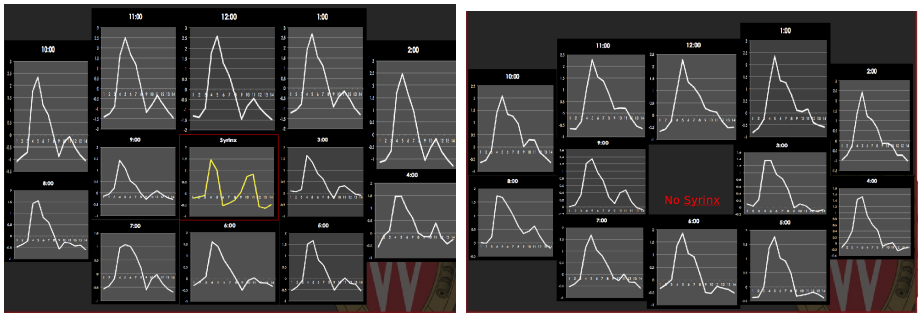

Figure A.7: Postoperative (left) and asymptomatic (right, 10 months after surgery) CSF velocities

Appendix B

In vivo Pressure Measurements

B.1 Estimating pressures at the cervical region

In figure 8.2 it was established that baseline pressures were always higher in Lumbar regions than in the intracranial region. If this difference in baseline pressure is omitted, we noted that there seem to be some wave propagating downwards being damped and smoothened out, with diffusion-like behavior. We asked for raw data from Rikshospitalet to more accurately investigate these observations. Data files consists of one number on each line giving intracranial pressure (ICP) or lumar pressure (LP). The sampling rate is 200 Hz, so real time data can be made. Two files exists for each subject, one measuring ICP and the other LP. An example of unedited data is shown in figure B.1. We used a butterworth filter design of order 7 with a critical frequency of 15 Hz. We used the filtfilt() function in scipy to apply the filter twice, once forward and once backwards. After the jump in pressure, the lumbar pressure is always higher in agreement with what was reported by Frič and Eide (2015) [88]. We are told to disregard the first and last part of these data and focus on the middle part. This seems legit, as data differs at these edges as well as being unstable with large-amplitude oscillations. For single beats, is is claimed that the baseline for the two parts should be ignored. We created a corresponding time series to investigate the propagation along the cord in time. We apply a butterworth

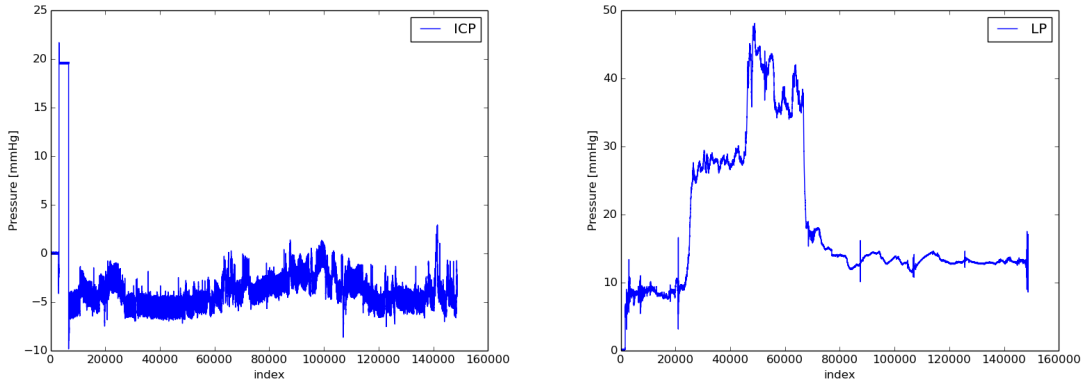

Figure B.1: Intracranial (left) and lumbar (right) pressure measurements

filter with 10 Hz as the critical frequency. Raw data and filtered data are compared in figure B.2 A very simple equation describing damping of signals and smoothing

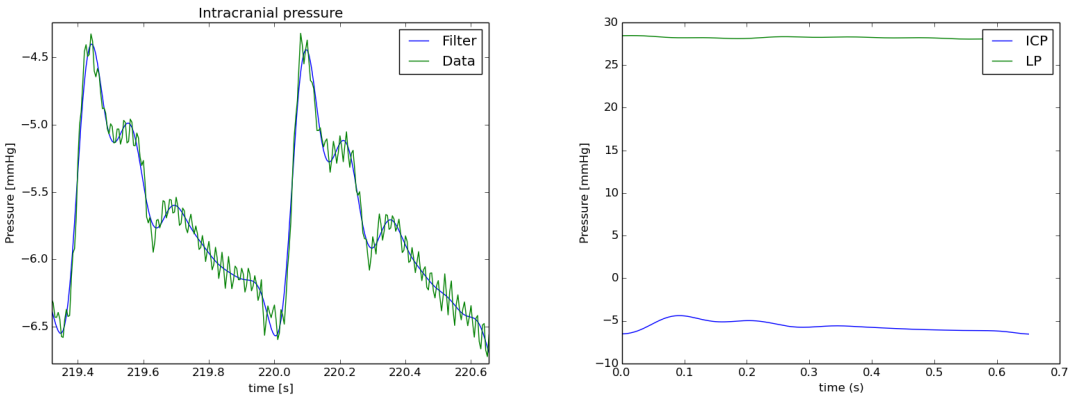

Figure B.2: ICP measurements with filtered data (left) and filtered ICP and LP in the same plot (right)

is the heat equation. We try to estimate the pressure at cervical regions by letting the pressure be a function in space, $p(x)$ that is smoothened out over time. This is not necessarily the case, but is built on the observation that this kind of damping seems to occur. The method can be regarded as a simplification of the damped wave equation as described in [95]. In other words we solve

$$\frac{\partial p}{\partial t} = k\frac{\partial^2 p}{\partial x^2}$$

where k is a constant. Obviously, as we have been told, the baseline pressures can not be trusted as the lumbar pressure is of several magnitudes higher at all times. We therefore shift the two curves to have the same baseline pressure. The first step is to adjust k so that solving up to some end time, T gives the lumbar pressure curve. In this first data set, very little response was observed at lumbar regions making this a bit more difficult. We use the filtered ICP as initial conditions and baseline pressure Dirichlet boundary conditions on both sides. Solving until $T_{end} = 0.2s$ and $k = 0.1\ m^2/s$ gives results given in figure B.3. In this case, the signal was estimated to reach the bottom at the global minimum of the LP yielding a wave speed of $\approx 2.4m/s$. The dampened signal from the ICP was therefore shifted along the x-axis according to this, so that the estimated damped signal would not reach the bottom of the cord earlier than the data suggests.

The idea is now to solve the same equation, but now solving for a shorter end time. For instance, the pressure halfway down the cord would be estimated by solving with the same value of k until $T = T_{end}/2$. The total length of the spinal cord is $L \approx 45cm$, and our model only has a length of $l = 6cm$. We therefore solve only up to $T = T_{end}\frac{l}{L}$. Bertram (2009) [15] showed that the presence of a syrinx critically changes wave speeds, and we have omited this fact in this method by assuming the same wave characteristics all along the cord. The results are summarized in figure B.4. This method acts as a preliminary test for solving the dampened wave equation with ICP measurements at the cranial end and homogeneous Neumann

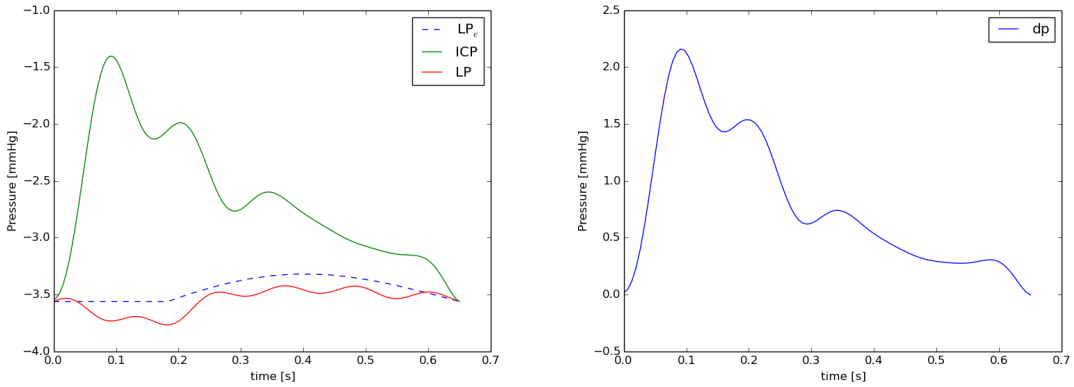

Figure B.3: Left: ICP, LP and estimated LP pressure. Right: Pressure difference dp = ICP - estimated LP

conditions at the caudal end. The actual pressure value at the caudal end could be recorded and compared to measurements of LP. The results presented in this section needs more investigation but successfully capture the shape of the pressure wave as estimated by Ringstad et al. (2016, not yet published) [97]. The results here also suggest a strong negative pressure gradient following the first wave, a necessity to obtain physiological flow patterns (ref. section 8.6). Using the same approach on

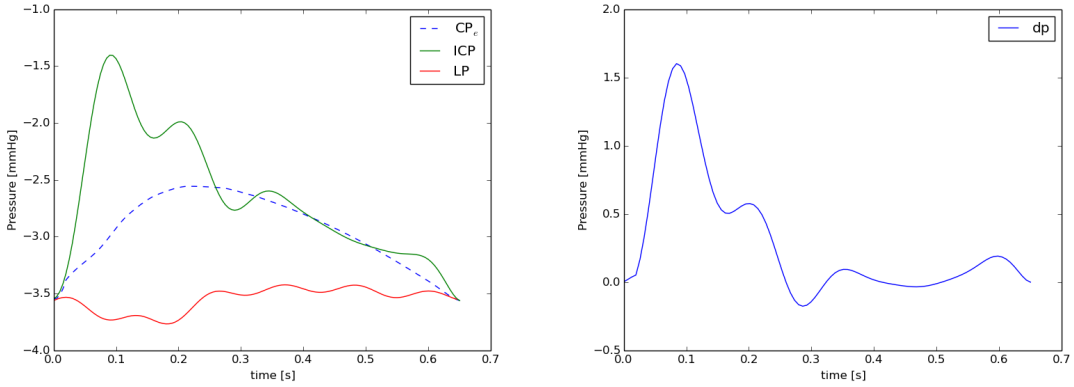

Figure B.4: Left: ICP, LP and estimated cervical pressure (CP) at C6. Right: Pressure difference dp = ICP - estimated CP

the published data by Frič and Eide (2015) [88] as shown in figure 8.2, gives results depicted in figure B.5

B.1.1 Example of a different wave

In section 8.5, we chose a 5th degree spline to investigate effects of a steeper pressure gradient. It did not capture the pressure rise at $t \approx 0.4$ into the cycle. Figure B.6 shows that this pressure rise is not present at every heart beat, which, according to our results in sections 8.5 and 8.5.2, could affect displacement patterns and syrinx velocity dynamics.

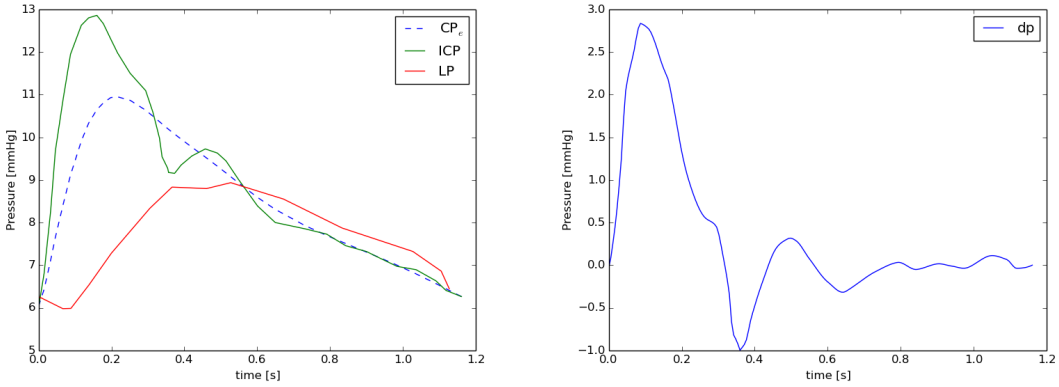

Figure B.5: Left: ICP, LP and estimated cervical pressure (CP) at C6. Right: Pressure difference dp = ICP - estimated CP

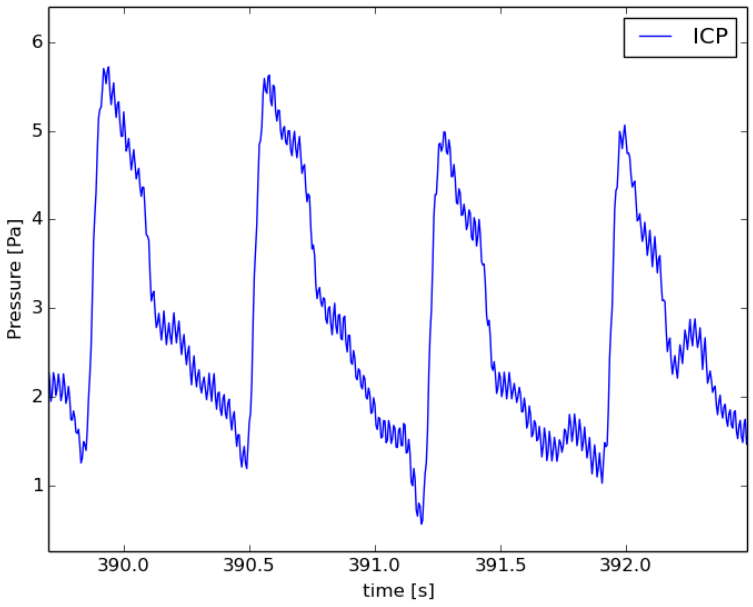

Figure B.6: ICP measurements. The common pressure rise shortly after peak presure is not seen in beats 1,2 and 3.

Bibliography

[1] K. S. Paul, R. H. Lye, F. A. Strang, and J. Dutton, "Arnold-chiari malformation: review of 71 cases," *Journal of neurosurgery*, vol. 58, no. 2, pp. 183–187, 1983.

[2] N. Di Lorenzo, L. Palma, E. Paletinsky, and A. Fortuna, "" conservative" cranio-cervical decompression in the treatment of syringomyelia-chiari i complex: A prospective study of 20 adult cases.," *Spine*, vol. 20, no. 23, pp. 2479–2482, 1995.

[3] F. Guo, M. Wang, J. Long, H. Wang, H. Sun, B. Yang, and L. Song, "Surgical management of chiari malformation: analysis of 128 cases," *Pediatric neurosurgery*, vol. 43, no. 5, pp. 375–381, 2007.

[4] M. F. Quigley, B. Iskandar, M. A. Quigley, M. Nicosia, and V. Haughton, "Cerebrospinal fluid flow in foramen magnum: temporal and spatial patterns at MR imaging in volunteers and in patients with Chiari I malformation 1," *Radiology*, vol. 232, no. 1, pp. 229–236, 2004.

[5] V. M. Haughton, F. R. Korosec, J. E. Medow, M. T. Dolar, and B. J. Iskandar, "Peak systolic and diastolic CSF velocity in the foramen magnum in adult patients with chiari i malformations and in normal control participants," *American journal of neuroradiology*, vol. 24, no. 2, pp. 169–176, 2003.

[6] S. Linge, V. Haughton, A. E. Løvgren, K.-A. Mardal, A. Helgeland, and H. P. Langtangen, "Effect of tonsillar herniation on cyclic CSF flow studied with computational flow analysis," *American Journal of Neuroradiology*, vol. 32, no. 8, pp. 1474–1481, 2011.

[7] S. O. Linge, K.-A. Mardal, A. Helgeland, J. D. Heiss, and V. Haughton, "Effect of craniovertebral decompression on CSF dynamics in chiari malformation type i studied with computational fluid dynamics: Laboratory investigation," *Journal of neurosurgery. Spine*, vol. 21, no. 4, p. 559, 2014.

[8] G. Rutkowska, V. Haughton, S. Linge, and K.-A. Mardal, "Patient-specific 3d simulation of cyclic CSF flow at the craniocervical region," *American Journal of Neuroradiology*, vol. 33, no. 9, pp. 1756–1762, 2012.

[9] E. C. Clarke, D. F. Fletcher, M. A. Stoodley, and L. E. Bilston, "Computational fluid dynamics modelling of cerebrospinal fluid pressure in chiari malformation

and syringomyelia," *Journal of biomechanics*, vol. 46, no. 11, pp. 1801–1809, 2013.

[10] S. Cheng, D. Fletcher, S. Hemley, M. Stoodley, and L. Bilston, "Effects of fluid structure interaction in a three dimensional model of the spinal subarachnoid space," *Journal of biomechanics*, vol. 47, no. 11, pp. 2826–2830, 2014.

[11] B. A. Martin and F. Loth, "The influence of coughing on cerebrospinal fluid pressure in an in vitro syringomyelia model with spinal subarachnoid space stenosis," *Cerebrospinal Fluid Res*, vol. 6, no. 1, p. 17, 2009.

[12] B. A. Martin, R. Labuda, T. J. Royston, J. N. Oshinski, B. Iskandar, and F. Loth, "Spinal subarachnoid space pressure measurements in an in vitro spinal stenosis model: implications on syringomyelia theories," *Journal of biomechanical engineering*, vol. 132, no. 11, p. 111007, 2010.

[13] C. Bertram, A. Brodbelt, and M. Stoodley, "The origins of syringomyelia: numerical models of fluid/structure interactions in the spinal cord," *Journal of biomechanical engineering*, vol. 127, no. 7, pp. 1099–1109, 2005.

[14] C. Bertram, L. Bilston, and M. Stoodley, "Tensile radial stress in the spinal cord related to arachnoiditis or tethering: a numerical model," *Medical & biological engineering & computing*, vol. 46, no. 7, pp. 701–707, 2008.

[15] C. Bertram, "A numerical investigation of waves propagating in the spinal cord and subarachnoid space in the presence of a syrinx," *Journal of Fluids and Structures*, vol. 25, no. 7, pp. 1189–1205, 2009.

[16] C. Bertram, "Evaluation by fluid/structure-interaction spinal-cord simulation of the effects of subarachnoid-space stenosis on an adjacent syrinx," *Journal of biomechanical engineering*, vol. 132, no. 6, p. 061009, 2010.

[17] N. K. Kylstad, "Simulating the viscoelastic response of the spinal cord," 2014.

[18] K. H. Støverud, M. Alnæs, H. P. Langtangen, V. Haughton, and K.-A. Mardal, "Poro-elastic modeling of syringomyelia–a systematic study of the effects of pia mater, central canal, median fissure, white and gray matter on pressure wave propagation and fluid movement within the cervical spinal cord," *Computer methods in biomechanics and biomedical engineering*, pp. 1–13, 2015.

[19] A. Logg, K.-A. Mardal, and G. Wells, *Automated solution of differential equations by the finite element method: The FEniCS book*, vol. 84. Springer Science & Business Media, 2012.

[20] J. Hron and S. Turek, *A monolithic FEM/multigrid solver for an ALE formulation of fluid-structure interaction with applications in biomechanics*. Springer, 2006.

[21] D. Van Wynsberghe, C. R. Noback, and R. Carola, *Human anatomy and physiology*. McGraw-Hill College, 1995.

[22] D. N. Levine, "The pathogenesis of syringomyelia associated with lesions at the foramen magnum: a critical review of existing theories and proposal of a new hypothesis," *Journal of the neurological sciences*, vol. 220, no. 1, pp. 3–21, 2004.

[23] N. Elliott, C. Bertram, B. A. Martin, and A. Brodbelt, "Syringomyelia: A review of the biomechanics," *Journal of Fluids and Structures*, vol. 40, pp. 1–24, 2013.

[24] B. Williams, "On the pathogenesis of syringomyelia: a review.," *Journal of the Royal Society of Medicine*, vol. 73, no. 11, p. 798, 1980.

[25] D. Greitz, "Unraveling the riddle of syringomyelia," *Neurosurgical review*, vol. 29, no. 4, pp. 251–264, 2006.

[26] A. Thompson, N. Madan, J. Hesselink, G. Weinstein, A. M. del Rio, and V. Haughton, "The cervical spinal canal tapers differently in patients with chiari i with and without syringomyelia," *American Journal of Neuroradiology*, 2015.

[27] V. J. Katz, "The history of stokes' theorem," *Mathematics Magazine*, vol. 52, no. 3, pp. 146–156, 1979.

[28] O. Reynolds, *Papers on Mechanical and Physical Subjects, The Sub-Mechanics of the Universe*, vol. 3. Cambridge University Press, Cambridge, 1903.

[29] F. White, *Viscous Fluid Flow*. McGraw-Hill series in mechanical engineering, McGraw-Hill, 3 ed., 2006.

[30] B. Gjevik, "Viskøse vesker og elastiske stoffer," *Forelesninger i MEK2200*, 2002.

[31] J. N. Newman, *Marine Hydrodynamics*. The MIT Press, 1977.

[32] P. K. Kundu, I. M. Cohen, and D. R. Dowling, *Fluid Mechanics*. Elsevier, Academic Press, 5 ed., 2012.

[33] H. F. Wang, *Theory of linear poroelasticity*. 2000.

[34] D. A. Nield and A. Bejan, *Convection in Porous Media*. Springer, 4 ed., 2013.

[35] M. A. Biot, "General theory of three-dimensional consolidation," *Journal of applied physics*, vol. 12, no. 2, pp. 155–164, 1941.

[36] M. A. Biot, "Theory of elasticity and consolidation for a porous anisotropic solid," *Journal of Applied Physics*, vol. 26, no. 2, pp. 182–185, 1955.

[37] M. Biot, "Theory of finite deformations of porous solids," *Indiana University Mathematics Journal*, vol. 21, no. 7, pp. 597–620, 1972.

[38] I. N. Drøsdal, "Porous and viscous modeling of cerebrospinal fluid flow in the spinal canal associated with syringomyelia," 2011.

[39] J. Donea, A. Huerta, J.-P. Ponthot, and A. Rodriguez-Ferran, *Encyclopedia of Computational Mechanics Vol. 1: Fundamentals., Chapter 14: Arbitrary Lagrangian-Eulerian Methods*. Wiley & Sons, 2004.

[40] T. Belytschko, J. M. Kennedy, and D. Schoeberle, "Quasi-eulerian finite element formulation for fluid-structure interaction," *Journal of Pressure Vessel Technology*, vol. 102, no. 1, pp. 62–69, 1980.

[41] A. M. Winslow, ""equipotential"zoning of two-dimensional meshes," tech. rep., California Univ., Livermore (USA). Lawrence Livermore Lab., 1963.

[42] G. S. Beavers and D. D. Joseph, "Boundary conditions at a naturally permeable wall," *Journal of fluid mechanics*, vol. 30, no. 01, pp. 197–207, 1967.

[43] P. G. Saffman, "On the boundary condition at the surface of a porous medium," *Studies in Applied Mathematics*, vol. 50, no. 2, pp. 93–101, 1971.

[44] I. Jones, "Low reynolds number flow past a porous spherical shell," in *Mathematical Proceedings of the Cambridge Philosophical Society*, vol. 73, pp. 231–238, Cambridge Univ Press, 1973.

[45] H. P. Langtangen, *Finite Element Method*. 2015.

[46] S. Brenner and R. Scott, *The mathematical theory of finite element methods*, vol. 15. Springer Science & Business Media, 2007.

[47] J. R. Womersley, "Method for the calculation of velocity, rate of flow and viscous drag in arteries when the pressure gradient is known," *The Journal of physiology*, vol. 127, no. 3, p. 553, 1955.

[48] W. E. Langlois and M. O. Deville, *Slow viscous flow*. Springer, 1964.

[49] H. C. Elman, D. J. Silvester, and A. J. Wathen, *Finite elements and fast iterative solvers: with applications in incompressible fluid dynamics*. Oxford University Press (UK), 2014.

[50] W. L. Barth and G. F. Carey, "On a boundary condition for pressure-driven laminar flow of incompressible fluids," *International journal for numerical methods in fluids*, vol. 54, no. 11, pp. 1313–1325, 2007.

[51] M. Schäfer, S. Turek, F. Durst, E. Krause, and R. Rannacher, *Benchmark computations of laminar flow around a cylinder*. Springer, 1996.

[52] S. Turek and J. Hron, *Proposal for numerical benchmarking of fluid-structure interaction between an elastic object and laminar incompressible flow*. Springer, 2006.

[53] A. Y. Tang and N. Amin, "Some numerical approaches to solve fluid structure interaction problems in blood flow," in *Abstract and Applied Analysis*, vol. 2014, Hindawi Publishing Corporation, 2014.

[54] K. Selim, "Adaptive finite element methods for Fluid-Structure interaction and incompressible flow," 2011.

[55] C. Taylor and P. Hood, "A numerical solution of the navier-stokes equations using the finite element technique," *Computers & Fluids*, vol. 1, no. 1, pp. 73–100, 1973.

[56] F. Brezzi and M. Fortin, *Mixed and hybrid finite element methods*, vol. 15. Springer Science & Business Media, 2012.

[57] M. Fortin, "Old and new finite elements for incompressible flows," *International Journal for numerical methods in fluids*, vol. 1, no. 4, pp. 347–364, 1981.

[58] A. Quaini, "Algorithms for fluid-structure interaction problems arising in hemodynamics," 2009.

[59] G. Balaban, "A newtons method finite element algorithm for fluid-structure interaction," 2012.

[60] B. Tully and Y. Ventikos, "Coupling poroelasticity and CFD for cerebrospinal fluid hydrodynamics," *Biomedical Engineering, IEEE Transactions on*, vol. 56, no. 6, pp. 1644–1651, 2009.

[61] J. C. Vardakis, D. Chou, B. J. Tully, C. C. Hung, T. H. Lee, P.-H. Tsui, and Y. Ventikos, "Investigating cerebral oedema using poroelasticity," *Medical engineering & physics*, 2016.

[62] S. Badia, A. Quaini, and A. Quarteroni, "Coupling biot and navier–stokes equations for modelling fluid–poroelastic media interaction," *Journal of Computational Physics*, vol. 228, no. 21, pp. 7986–8014, 2009.

[63] S. Linge, V. Haughton, A. Løvgren, K. Mardal, and H. Langtangen, "CSF flow dynamics at the craniovertebral junction studied with an idealized model of the subarachnoid space and computational flow analysis," *American Journal of Neuroradiology*, vol. 31, no. 1, pp. 185–192, 2010.

[64] R. A. Fishman, *Cerebrospinal fluid in diseases of the nervous system*. WB Saunders company, 1992.

[65] J. H. Smith and J. A. Humphrey, "Interstitial transport and transvascular fluid exchange during infusion into brain and tumor tissue," *Microvascular research*, vol. 73, no. 1, pp. 58–73, 2007.

[66] T.-K. Hung, G.-L. Chang, H.-S. Lin, F. R. Walter, and L. Bunegin, "Stress-strain relationship of the spinal cord of anesthetized cats," *Journal of biomechanics*, vol. 14, no. 4, pp. 269–276, 1981.

[67] F. Ben-Hatira, K. Saidane, and A. Mrabet, "A finite element modeling of the human lumbar unit including the spinal cord," *Journal of Biomedical Science and Engineering*, vol. 5, no. 3, p. 150, 2012.

[68] H. Ozawa, T. Matsumoto, T. Ohashi, M. Sato, and S. Kokubun, "Mechanical properties and function of the spinal pia mater," *Journal of Neurosurgery*, vol. 1, no. 1, pp. 122–127, 2004.

[69] S. Cheng, E. C. Clarke, and L. E. Bilston, "Rheological properties of the tissues of the central nervous system: a review," *Medical engineering & physics*, vol. 30, no. 10, pp. 1318–1337, 2008.

[70] E. C. Clarke, "Spinal cord mechanical properties," in *Neural Tissue Biomechanics*, pp. 25–40, Springer, 2010.

[71] C. Persson, J. L. Summers, and R. M. Hall, "Modelling of spinal cord biomechanics: In vitro and computational approaches," in *Neural Tissue Biomechanics*, pp. 181–201, Springer, 2010.

[72] B. K. Kwon, T. R. Oxland, and W. Tetzlaff, "Animal models used in spinal cord regeneration research," *Spine*, vol. 27, no. 14, pp. 1504–1510, 2002.

[73] E. Zarzur, "Mechanical properties of the human lumbar dura mater," *Arquivos de neuro-psiquiatria*, vol. 54, no. 3, pp. 455–460, 1996.

[74] D. J. Patin, E. C. Eckstein, K. Harum, and V. S. Pallares, "Anatomic and biomechanical properties of human lumbar dura mater.," *Anesthesia & Analgesia*, vol. 76, no. 3, pp. 535–540, 1993.

[75] "Densities of different body matter - sources with values cited below." http://www.scrollseek.com/training/densitiesofdifferentbodymatter.html. accessed:2016-05-10.

[76] C. Nicholson, "Diffusion and related transport mechanisms in brain tissue," *Reports on progress in Physics*, vol. 64, no. 7, p. 815, 2001.

[77] C. Watson, G. Paxinos, and G. Kayalioglu, *The spinal cord: a Christopher and Dana Reeve Foundation text and atlas*. Academic press, 2009.

[78] H. Ko, J. Park, Y. Shin, and S. Baek, "Gross quantitative measurements of spinal cord segments in human," *Spinal Cord*, vol. 42, no. 1, pp. 35–40, 2004.

[79] K.-H. Støverud, "Relation between the chiari i malformation and syringomyelia from a mechanical perspective," 2014.

[80] B. A. Martin, W. Kalata, F. Loth, T. J. Royston, and J. N. Oshinski, "Syringomyelia hydrodynamics: an in vitro study based on in vivo measurements," *Journal of biomechanical engineering*, vol. 127, no. 7, pp. 1110–1120, 2005.

[81] B. A. Martin, R. Labuda, T. J. Royston, J. N. Oshinski, B. Iskandar, and F. Loth, "Pathological biomechanics of cerebrospinal fluid pressure in syringomyelia: Fluid structure interaction of an in vitro coaxial elastic tube system," pp. 941–942, 2009.

[82] B. Williams, "Simultaneous cerebral and spinal fluid pressure recordings," *Acta neurochirurgica*, vol. 59, no. 1-2, pp. 123–142, 1981.

[83] M. Häckel, V. Beneš, and M. Mohapl, "Simultaneous cerebral and spinal fluid pressure recordings in surgical indications of the chiari malformation without myelodysplasia," *Acta neurochirurgica*, vol. 143, no. 9, pp. 909–918, 2001.

[84] P. K. Eide, G. Bentsen, A. G. Sorteberg, P. B. Marthinsen, A. Stubhaug, and W. Sorteberg, "A randomized and blinded single-center trial comparing the effect of intracranial pressure and intracranial pressure wave amplitude-guided intensive care management on early clinical state and 12-month outcome in patients with aneurysmal subarachnoid hemorrhage," *Neurosurgery*, vol. 69, no. 5, pp. 1105–1115, 2011.

[85] P. K. Eide and A. Brean, "Cerebrospinal fluid pulse pressure amplitude during lumbar infusion in idiopathic normal pressure hydrocephalus can predict response to shunting," *Cerebrospinal Fluid Res*, vol. 7, no. 5, 2010.

[86] P. K. Eide and E. Kerty, "Static and pulsatile intracranial pressure in idiopathic intracranial hypertension," *Clinical neurology and neurosurgery*, vol. 113, no. 2, pp. 123–128, 2011.

[87] P. K. Eide and W. Sorteberg, "Diagnostic intracranial pressure monitoring and surgical management in idiopathic normal pressure hydrocephalus: A 6-year review of 214 patients," *Neurosurgery*, vol. 66, no. 1, pp. 80–91, 2010.

[88] R. Frič and P. K. Eide, "Comparison of pulsatile and static pressures within the intracranial and lumbar compartments in patients with chiari malformation type 1: a prospective observational study," *Acta neurochirurgica*, vol. 157, no. 8, pp. 1411–1423, 2015.

[89] M. Czosnyka and J. D. Pickard, "Monitoring and interpretation of intracranial pressure," *Journal of Neurology, Neurosurgery & Psychiatry*, vol. 75, no. 6, pp. 813–821, 2004.

[90] B. Williams, "Cerebrospinal fluid pressure changes in response to coughing.," *Brain: a journal of neurology*, vol. 99, no. 2, pp. 331–346, 1976.

[91] C. A. Sansur, J. D. Heiss, H. L. DeVroom, E. Eskioglu, R. Ennis, and E. H. Oldfield, "Pathophysiology of headache associated with cough in patients with chiari i malformation," *Journal of neurosurgery*, vol. 98, no. 3, pp. 453–458, 2003.

[92] P. Brugières, I. Idy-Peretti, C. Iffenecker, F. Parker, O. Jolivet, M. Hurth, A. Gaston, and J. Bittoun, "CSF flow measurement in syringomyelia," *American journal of neuroradiology*, vol. 21, no. 10, pp. 1785–1792, 2000.

[93] G. Pinna, F. Alessandrini, A. Alfieri, M. Rossi, and A. Bricolo, "Cerebrospinal fluid flow dynamics study in chiari i malformation: implications for syrinx formation," *Neurosurgical focus*, vol. 8, no. 3, pp. 1–8, 2000.

[94] V. Haughton and K.-A. Mardal, "Spinal fluid biomechanics and imaging: an update for neuroradiologists," *American Journal of Neuroradiology*, vol. 35, no. 10, pp. 1864–1869, 2014.

[95] N. Elliott, "Syrinx fluid transport: modeling pressure-wave-induced flux across the spinal pial membrane," *Journal of biomechanical engineering*, vol. 134, no. 3, p. 031006, 2012.

[96] L. E. Bilston, M. A. Stoodley, and D. F. Fletcher, "The influence of the relative timing of arterial and subarachnoid space pulse waves on spinal perivascular cerebrospinal fluid flow as a possible factor in syrinx development: Laboratory investigation," *Journal of neurosurgery*, vol. 112, no. 4, pp. 808–813, 2010.

[97] G. Ringstad, E. K. Lindstrøm, S. Vatnehol, K.-A. Mardal, K. Emblem, and P. K. Eide, "Non-invasive assessment of pulsatile intracranial pressure with phase-contrast magnetic resonance imaging," *Submitted to journal*, 2016.